Exploration of several Radiation-based Analytical Techniques to investigate Chlorides and Chlorides Effects within Concrete

by

Mabuti Jacob Radebe

Thesis submitted in partial fulfillment of the
requirements for the M.Sc. degree in Physics at the
University of the Western Cape

June 2007

Supervisor: Mr. F. C de Beer

Co-supervisor: Prof. R. Lindsay

Declaration

I, the undersigned, declare that the work contained in this thesis is my own original work and has not previously in its entirety or in part been submitted at any university for a degree.

Signature: .....

Date: .....

Acknowledgements

I wish to express my appreciation to the following organizations and people who made this thesis possible:

University of the Western Cape Physics department, for financial assistance and for enabling me realize my dream of becoming a Physicist. The warmth I experienced inspired and encouraged me to achieve the great.

Radiation Utilisation group of the **Applied Nuclear Science and Technology** (ANST) **Division** at **Necsa** (South African Nuclear Energy Corporation) for making their SANRAD (South African Neutron Radiography) facility available for the study, for their welcoming spirit and for financial support.

Frikkie C. de Beer, my supervisor, for his guidance, support and leadership during the study. Thanks for all the enrichment and enlightenment, and for all your patience.

Professor Robbie Lindsay, co-supervisor, for guidance, contribution and for ensuring that my stay at Necsa is fruitful and enjoyable.

Carel Schoeman, for his assistance during experimental work.

My parents, **Elias and Nomahlubi Radebe**, sisters **(Khethiwe and Zanele)** and brothers **(Timothy and Mahlubandile)** for believing in me and supporting me all the way. I'm proud of you.

All my friends, your companionship was and is so fruitful for this study.

Finally I would like to thank the **Almighty God** for all He has enabled, helped me to do ; and all He has done for me. Thank you Lord, you are so righteous.

Exploration of several Radiation-based Analytical Techniques to investigate Chlorides and Chlorides Effects within Concrete

Mabuti Jacob Radebe

Abstract

In this study, the capabilities of Neutron Radiography (NRad) and -Tomography (NTomo), as well as X-ray Radiography (XRad) to investigate chlorides and chlorides corrosion effects within steel reinforced laboratory concrete samples are practically explored. Capabilities of Scanning Electron Microscopy (SEM), Prompt Gamma Neutron Activation Analysis (PGNAA), Particle Induced X-ray Emission (PIXE), Small-Angle Neutron Scattering (SANS), Neutron Diffraction (NDIFF) and X-ray Diffraction (XDIFF) analytical techniques are also explored through review of literature.

NRad, NTomo and Xrad were practically applied in three sub-studies: (1) the visualization and quantification of corrosion effects on steel reinforcing matter within concrete samples; (2) preliminary investigation of the change in detected flux of neutrons and x-rays due to attenuation by NaCl solutions of concentrations 3, 5, 8, 10 and 20 %wt respectively and (3) comparative study of Nrad and Gravimetrical methods to determine the porosity of plain concrete samples.

In the first sub-study, two steel reinforced concrete samples each containing six thin plain steel plates were respectively submerged in distilled water and in 20wt%[NaCl] solution for eight weeks. Two sets of independently existing thin plain steel plates were also submerged in the two liquids for eight weeks. Visualization of steel within concrete samples was achieved through NRad and associated NTomo software packages, by taking advantage of the penetrating capability of neutrons. The corrosion effect of chlorides on the steel reinforced concrete samples was studied through quantification and comparison of steel

matter volume after each exposure period. It was found that reinforcement steel in concrete corroded faster in the 20%wt[NaCl] solution, while independently existing steel matter corroded faster in distilled water.

In the second sub-study, variation in attenuation by solutions with water containing 3, 5, 8, 10 and 20%wt[NaCl] was imaged using XRad and NRad. The difference in attenuation coefficients between 0 and 20%wt[NaCl] solutions was found to be 0.1442 cm^{-1} for thermal neutrons and 0.1234 cm^{-1} for x-rays generated at 20 kV.

In the third sub-study, the porosity of two sets of three concrete samples of equal densities was tested. One set of samples was submerged in distilled water (leached samples) and another in lime water (3g CaOH/Liter of distilled water). During this study porosity was determined before exposure to any of the two liquids and after 25 days of exposure. The procedure with submersion of the samples was continuous for 12 days submersion followed by 8 hour/day submersion for 13 days. Porosity values obtained from the two methods, NRad and gravimetric, corresponded well, but NRad values were always higher than gravimetric values.

From literature reviewing, PGNAA has proven capabilities for elemental and concentration determination to even deeper depths into concrete. SANS, SEM, PIXE, XDIFF and NDIFF have shortcomings such as sample preparation, some with shallow penetration depths and investigation of small sized samples.

Table of Figures

List of Tables

Table of contents

Contents **Page No.**

Chapter 1: Introduction

In this chapter the aim of study, the problem statement (section 1.1), background knowledge on concrete structures (section 1.2), penetrating radiation (section 1.3) with respect to neutrons (section 1.3.1), X-rays and Gammas (section 1.3.2), as well as a description of radiation-based analytical techniques (section 1.4) with respect to this study, are discussed.

The primary aim for this study is to explore the capabilities of radiation-based analytical techniques to identify chlorides and the effects of chlorides within laboratory concrete samples. Radiation-based analytical techniques explored in this study are:

- Neutron Radiography and Tomography (NRad and NTomo)
- X-ray Radiography and Tomography (XRad and XTomo)
- Particle Induced X-ray Emission (PIXE)
- Scanning Electron Microscopy (SEM)
- Prompt Gamma Neutron Activation Analysis (PGNAA)
- Small Angle Neutron Scattering (SANS)
- X-ray Diffraction (XDIFF)
- Neutron Diffraction (NDIFF)

Facilities to conduct NRad and XRad are available at Necsa and were considered for experimental evaluations for the purpose of the study. Other techniques were only reviewed from literature, discussed and not used.

1.1 Scope of the study

This study comprises the following:

(a) Literature study of published research on the interaction of chloride sources with steel reinforced concrete using radiation-based analytical techniques.

(b) Quantitative neutron and x-ray investigations to determine their capability to detect differences in attenuation due to the presence of chlorides originating from different concentrations of NaCl in distilled water.

(c) Porosity measurements on concrete samples using neutron radiography and the gravimetric porosity measurement technique; as well as to contribute to literature on attempts to establish the radiography-based porosity measurement procedure.

(d) Quantitative tomography measurements of the volume of steel corroded within the laboratory concrete samples, due to submersion in distilled water and 20%wtNaCl solution respectively. These experiments were conducted to determine the capability of neutron tomography to identify and quantify the effects of chlorides on steel corrosion.

1.2 Problem Statement

Concrete structures see application in a variety of fields, such as civil engineering construction and road works. Concrete is also being used for radioactive waste containment, to build high rise buildings, highways, bridges, dams, etc. Premature or unexpected failure of concrete structures leads to great financial loss, even loss of lives. The existence of precise concrete structure lifespan and performance estimation methods are thus essential even in the research and development phase of concrete matter.

Methods have been developed to estimate the lifespan of concrete in structural members, but results from these methods have large uncertainties. More accurate lifespan estimation methods, and for estimation of the safety

performance of existing and planned concrete structures are needed [htt01]. Most conventional methods for safety performance estimation are destructive and determine only concrete properties and characteristics associated with concrete deterioration. Examples of such destructive methods are the Alkaline Leaching (AL) method and the In Situ Leaching (ISL) method which are both used for the determination of chloride content in concrete.

The AL method is used for chloride determination in the aqueous phase of hardened cementitious materials [Cas01], while the ISL method is for chloride determination from pore water ionic content determination in small cavities drilled in mortar or concrete specimens [Cas06].

Furthermore, methods for reduction of corrosive attack through the removal of chlorides have been developed. These methods are Cathodic Protection (CP) and Electrochemical Chloride Extraction (ECE) [htt01], [Naq06], each with its advantages and disadvantages. Not withstanding their ability to alleviate the corrosive attack, they cannot confirm that chlorides have been removed.
This study seeks to provide non-destructive visualization of steel within reinforced concrete and quantitative determination of volume of steel reduction due to corrosion. ECE, CP and the influence of chlorides on the corrosion rate [htt01], [Naq06] need techniques to validate results obtained so far using these techniques and hypothesis respectively.

1.3 Background information on concrete

Concrete is a masonry material made by mixing coarse aggregates, fine aggregates, cement, and water and allowing the mixture to cure into a solid mass. Coarse aggregates could be any coarse natural stone pieces, gravel for example, and fine aggregates any fine natural stone pieces, like sand. The cement is the chemically active component while the sand and stone are the inert

elements. This definition of concrete is relevant for plain concrete. Two kinds of concrete are defined; plain and steel reinforced. Steel reinforced concrete is plain concrete with steel bars embedded within. Concrete may also be viewed as a porous medium from a physics point of view.

The history of concrete goes a long way back to even before the birth of Christ. The Egyptians were already using this type of technology for the construction of their pyramids 3000 BC. It did not become a standard technique for construction until the Romans adopted it after 200 B.C. for roads, construction, and engineering works [htt03]. Combining pozzuolana[a] with lime, broken stones, bricks, and tuff[b], formed the concrete of the Romans. This was easily produced and had great durability. Famous structures such as the Pantheon of Rome and the Baths of Caracalla were built with this composition.

The component materials of concrete are mixed in varying proportions, according to the strength required and the function to be fulfilled. The ideal mixture is that which solidifies with minimum voids, i.e. porosity. A typical proportioning is 1:2:5, i.e. one part of cement, two parts of sand, and five parts of broken stone or gravel, with the sufficient amount of water for a pouring consistency. A simple test called a slump test is used to confirm the proportions and consistency of the mixture and it is then poured into wood, steel or polymer moulds, called forms. Concrete usually takes about 25 -28 days to cure or reach acceptable hardness [Jus98], but a technique called steam saturation can shorten the curing time to less than 18 hours.

Concrete used without strengthening is termed mass or plain concrete and has the structural properties of stone. This concrete has great strength under compressive forces but almost none under tensile forces. F. Joseph Monier, a French inventor, found that this tensile weakness could be overcome if steel rods were embedded in a concrete member. The new composite material was called reinforced concrete or Ferro concrete. It was put into use in 1857 through a construction of a private house in Port Chester, N.Y. United States [htt03].

---

c. A volcanic earth.

d. A rock composed of compacted volcanic ash varying in size from fine sand to coarse gravel.

There exists also concrete reinforced with polypropylene fibers instead of steel giving equivalent strength with a fraction of the thickness.

Reinforced concrete was improved by the development of pre-stressed concrete. This is concrete containing cables that are placed under tension opposite to the expected compression load before and after the concrete hardens. Another improvement useful for thin-shell construction, takes advantage of the inherent structural strength of certain geometric shapes, such as hemispherical and elliptical domes. As for the thin-shell construction, great distances are spanned with very little material. The perfecting of reinforced concrete has profoundly influenced structural building techniques and architectural forms.

1.4 Penetrating Radiation

Several types of penetrating radiation are known, such as gamma rays, x-rays and neutrons. Figure 1-1 classifies radiation types according to their energy range [htt04], [htt39].

The penetrating effect of x-ray radiation was discovered on the 8th November 1895 by Wilhelm Conrad Röntgen (1845-1923) who was a Professor at Wuerzburg University in Germany. Two weeks after the discovery of this effect of this type of radiation, Professor Röntgen took the first ever x-ray Radiograph of his wife's hand (see Figure 1-2) [htt23].

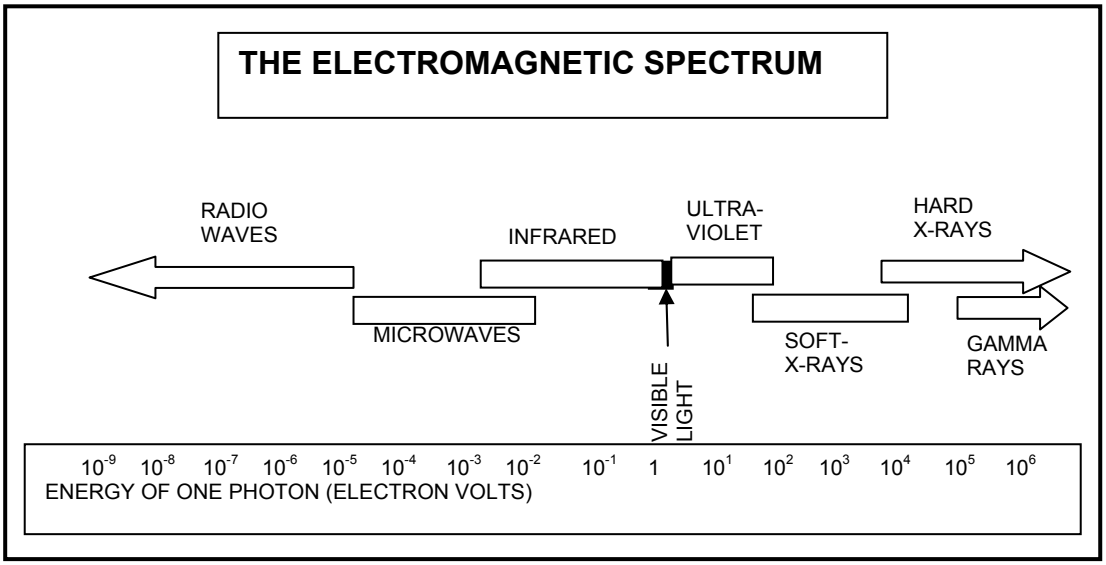

Figure 1-1: The electromagnetic spectrum.

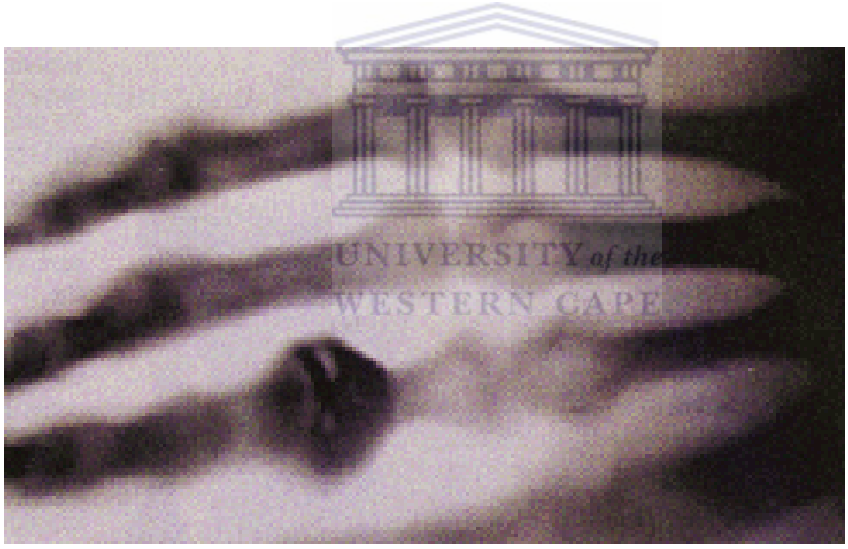

Figure 1-2: Mrs. Röntgen's hand, the first X-ray Radiograph [htt24].

Two German physicists, W. Bethe and H. Becker, discovered highly penetrating radiation in 1930 but suggested it was highly penetrative gamma rays. It is James Chadwick that discovered neutrons in 1932 [htt26], [htt27]. First neutron radiographs were produced in 1938 in a laboratory of the I.G. Farben Aktiengesellschaft in Berlin, Germany, in the years 1935 - 1938 by H. Kallmann and Kuhn; then in 1944 by O. Peter from the Forschungsanstalt der Deutschen Reichspost. The first neutron radiographs, developed in the 1935 - 1938, were

lost during the Battle of Berlin in 1944/45. The bottom half of Figure 1-3 presents the oldest existing neutron radiograph taken during 1944 by O. Peter [htt29], [Car92]. The figure shows how x-ray imaging (top images) compliments neutron imaging.

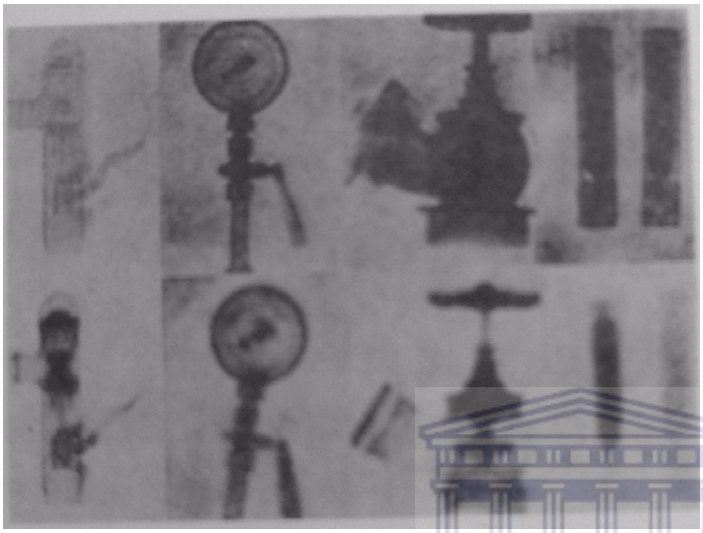

Figure 1-3: The oldest existing Neutron Radiograms by O. Peter, December 1944. [htt24].

1.4.1 Neutron radiation

Neutrons are one of the components of the atomic nucleus. Neutrons are emitted from the nucleus, creating free neutrons, during nuclear fission (either spontaneous or triggered), nuclear fusion, very high energy reactions such as in a Spallation Neutron Source, or from the (α,n) reaction, for example when a beryllium nucleus absorbs an alpha or deuterium particle and emits a neutron. Cold and thermal neutron radiation are most commonly used for transmission and scattering experiments in order to access the properties and the structure of materials in condensed matter physics, biology, solid state chemistry, materials science, geology, mineralogy and related sciences. Neutrons are generally categorized as cold, thermal and fast depending on their energies. A more comprehensive neutron classification according to their energies, as well as their scattering characteristics by materials which is important for radiography purposes is shown in Table 1.1[Bay92].

Table 1.1: Neutron classification according to energy and scattering characteristics.

TYPE	COMMENTS	ENERGY
Slow		**0eV to 10^4eV**
Cold	Materials possess high cross sections thus decrease transparency of most materials, increase efficiency of detection.	Less than 0.01 eV
Thermal	Slowing down of fast neutrons until average energy of neutron is equal to that of medium. Good discrimination capability between different materials.	0.01eV to 0.3eV
Epithermal		0.3 eV to 10^4eV
Resonance	Certain nuclei exhibit strong absorption character at well defined energies. Provides excellent discrimination for particular materials. Greater transmission and less scatter in samples containing Hydrogen.	1 eV to 10^2 eV
Fast	Good penetration Poor material discrimination because cross sections tend to be small and similar.	**10^4eV to 20 MeV**

Thermal neutrons are favored for radiographic work since they are easily captured by atomic nuclei. Neutrons used for neutron radiography are produced by nuclear research reactors, Van de Graaff accelerators, cyclotrons and radioisotopes. Neutrons from all available sources are born at high energies between 2 MeV and 14 MeV [htt05], [Bay92]. Thermal and epithermal neutrons are produced from high energy neutrons (fast neutrons) that lose energy when traveling through an appropriate moderating material with a low neutron absorption cross-section but high scattering cross-section such as water, heavy water, graphite, beryllium, polyethylene, etc. [Bay92]. In this study fast neutrons are moderated by water in the SAFARI-1 nuclear research reactor core. Gamma rays and fast neutrons are further removed using a bismuth crystal in the flight path of the experimental facility [Bee05]. A common and wide spread radioisotopic neutron source is ^{252}Cf that produces neutrons through spontaneous fission. Comparison of neutron sources as well as their advantages and disadvantages for neutron imaging are shown in Table 1.2 [Bay92]. It can be seen from Table 1.2 that despite the high running cost, the reactor source is the best radiography option.

Table 1.2: Comparison of neutron sources as to their advantages and disadvantages for neutron imaging.

SOURCE	NEUTRON FLUX ($n.cm^{-2}.s^{-1}$)	ADVANTAGES	DISADVANTAGES	RADIOGRAPHIC RESOLUTION
Nuclear Reactor	10^6- 10^9	High Flux Low cost per Neutron	High running cost Not portable Licenced	Excellent
Particle Accelerator	10^4- 10^6	Good flux	Poor target life Complex to operate	Medium
Radioisotopic sources	10^3- 10^4	Ease of operation Small size	Low flux level Decay of intensity Continuous output	Poor to medium

Outside the nucleus, neutrons are unstable and have a mean lifetime of about 12 minutes, [Col95]. Neutrons in this unstable form are known as free neutrons. A neutron decays by emitting an electron and antineutrino to become a proton.

Effects of neutron radiation

Neutron radiation is often called indirectly ionizing radiation. It does not ionize atoms in the same way protons, photons and electrons would do by exciting an electron because neutrons have no charge. However, when a neutron is absorbed the emitted gamma can remove electrons from an atom. This case presents indirect ionization effect of neutrons. Because neutrons are uncharged, they are generally more penetrating than alpha or beta radiation. In high atomic number materials neutrons are more penetrating than gamma radiation, whereas in hydrogen, a low energy neutron has far lower penetration compared to a high energy gamma. Health Physics considers neutrons as the fourth radiation hazard.

Another sometimes more severe hazard of neutron radiation is neutron activation. Neutron activation is the ability of neutron radiation to induce radioactivity in most substances it encounters, including the body tissues of humans. This occurs through the capture of neutrons by atomic nuclei, which are

transformed to another nuclide frequently, a radionuclide [htt40]. It is also a problem in nuclear fission and nuclear fusion installations, as it gradually renders the equipment radioactive; eventually the hardware must be replaced and disposed of as low-level radioactive waste.

Neutrons also degrade materials through intense bombardment creating dislocations in the materials. This leads to embrittlement of metals and materials through swelling. This poses a problem for nuclear reactor vessels in that it significantly limits their lifetime. The lifetime can be somewhat prolonged by controlled annealing. This is because controlled annealing reduces the number of the built-up dislocations. Graphite moderator blocks are especially susceptible to this effect, known as the Wigner effect and have to be annealed periodically [htt38].

Neutron radiation shielding

Neutron radiation protection relies on radiation shielding. In comparison with conventional ionizing radiation based on photons or charged particles, neutrons are absorbed in light (low atomic number) nuclei, so a large mass of hydrogen rich material is needed for shielding. The most effective materials for neutron shielding are water, polyethylene, boron, paraffin wax, or concrete where a considerable number of water molecules are chemically bound to the cement.

Secondary gamma rays (gamma rays other than that resulting from the fission process) radiation are often produced in such reactions, so additional shielding (in the form of lead) has to be provided to absorb it.

1.4.2 X-ray and Gamma Radiation

X-rays are high-energy electromagnetic radiation produced by: 1) electrons transitions from high energy levels to lower energy levels filling vacancies induced by electron excitations of inner energy shells electrons (characteristic

x-rays); and 2) by sudden stop of high energy electrons (Bremsstrahlung x-rays).

For the production of characteristic x-rays, incident particles must excite electrons from inner shells of the atoms of the target material. When electrons from higher energy level fall back into lower energy level electron holes, x-rays of energy equal to the energy difference between the two shells is emitted. The phenomenon of electron excitation and x-ray emission is shown in Figure 1-4 [htt29].

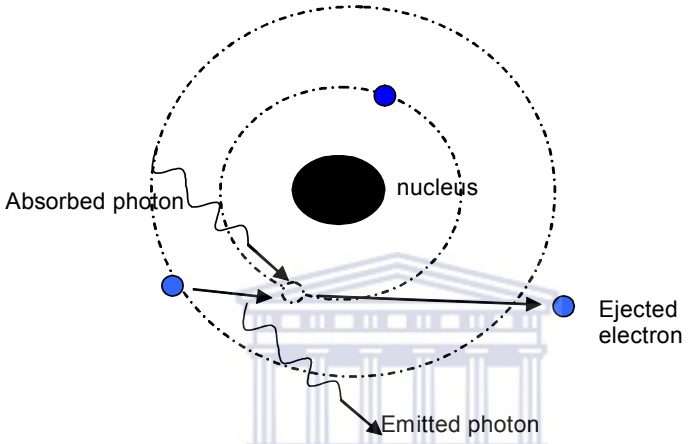

Figure 1-4: Demonstration of the phenomenon of the production of characteristic x-rays.

Bremsstrahlung x-rays are produced when free electrons from a heated filament (cathode) are accelerated and suddenly stopped by an anode material. Figure 1-5 presents an apparatus applied to produce Bremsstrahlung x-rays, where free electrons are accelerated, under vacuum, using the potential difference applied between the cathode and the anode.

Wilhelm Conrad Röntgen, a German scientist, observed x-rays while experimenting with vacuum tubes [htt04]. X-ray radiation is primarily used for diagnostic radiography and crystallography. X-rays are also a form of ionizing radiation and as such can be dangerous. In many languages it is called Röntgen radiation.

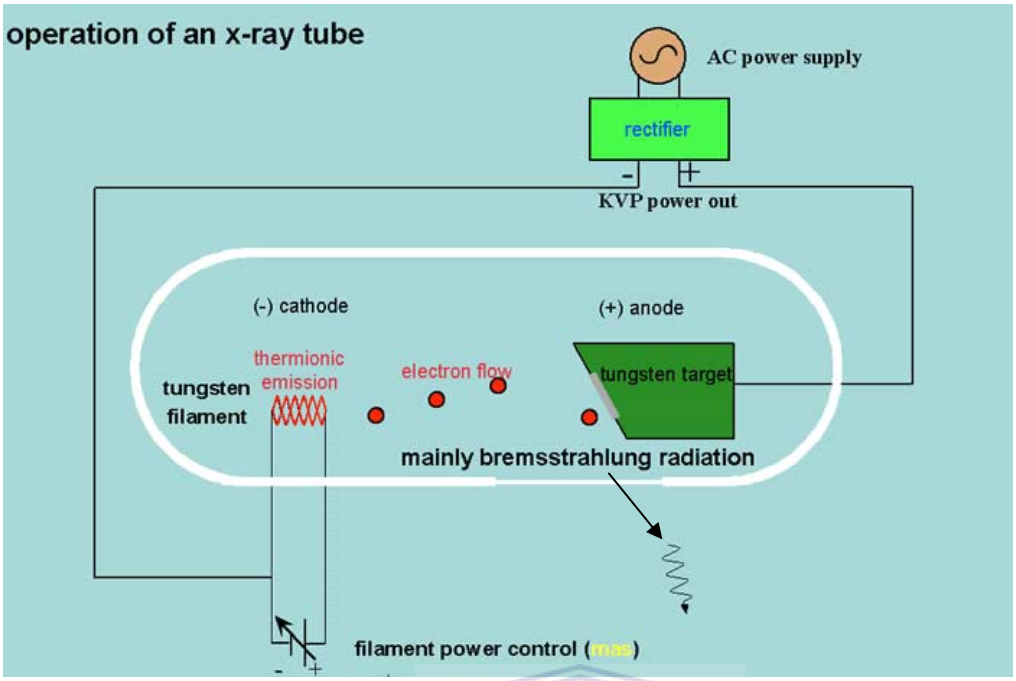

Figure 1-5: Demonstration of the phenomenon of the production of Bremmsstrahlung x-rays [htt43].

Gamma rays denoted by the greek symbol γ, occupy the highest-energy end of the electromagnetic spectrum and have generally higher photon energies than x-rays. Gamma rays are produced by radioactive decay or nuclear or subatomic processes such as electron-positron annihilation. An example of production of gammas from radioactive decay of ^{60}Co is shown below [htt08].

^{60}Co is a radioactive isotope that decays to excited ^{60}Ni by beta decay:

$$^{60}\mathrm{Co} \rightarrow {}^{60}\mathrm{Ni}^{*} + e^{-} + \bar{\nu}_{e}.$$

Where e^{-} is an electron and $\bar{\nu}_{e}$ is an electron-type antineutrino.

Then the ^{60}Ni decays by emitting two gamma rays in succession:

$$^{60}\mathrm{Ni}^{*} \rightarrow {}^{60}\mathrm{Ni} + 2\gamma.$$

Gamma rays of energy 1.17 MeV and 1.33 MeV are produced.

Figure 1-6 demonstrates how two 0.5 MeV gammas are produced from the process called positron-electron annihilation. The positron-electron annihilation is the process of the production of two 0.5 MeV gammas that results when a positron combines with an electron.

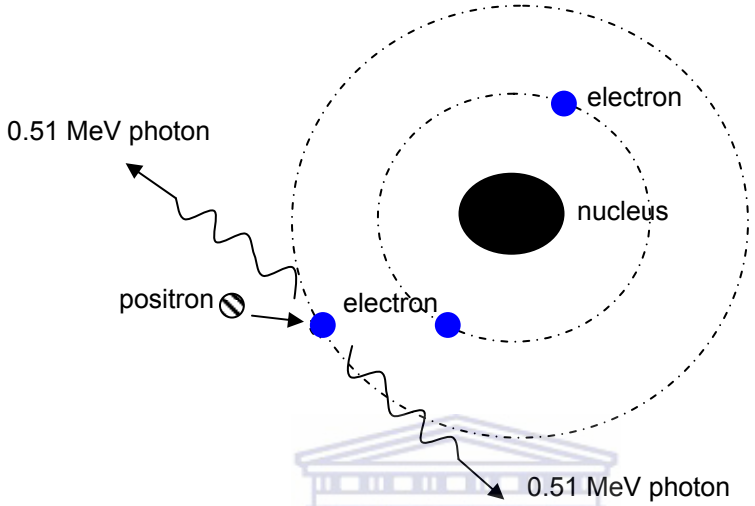

Figure 1-6: Demonstration of the phenomenon of the production of gamma rays through positron-electron annihilation.

Gamma rays were discovered by the French chemist and physicist, Paul Ulrich Villard in 1900 while he was studying uranium. He found that the rays were not bent by a magnetic field. For some time, it was assumed that gamma rays were particles. The fact that they were also waves was demonstrated by the British Physicist, William Henry Bragg in 1910 when he showed that the rays ionized gas in a similar way to x-rays. In 1914, Ernest Rutherford and Edward Andrade showed that gamma rays were a form of electromagnetic radiation by measuring their wavelengths using crystal diffraction. Rutherford named them gamma rays, after naming alpha and beta rays [htt04].

As seen on Figure 1-1, x-rays are defined as electromagnetic radiation with energies larger than 50 eV with soft x-rays overlaping the extreme ultraviolate radiation while hard x-rays overlaps low energy Gamma rays. Soft x-rays have energies between 50 eV and 10 keV and hard x-rays from 10 keV to several hundred keV.

Gammas are often defined to begin at energy of 100 keV, although electromagnetic radiation defined around 10 keV to several hundred keV is also referred to as hard x-rays. This is because it is possible for some electron transitions to be of higher energy than some nuclear phenomena. There is then an overlap between low energy gamma rays and high energy x-rays. It must also be noted that there is no physical difference between gamma rays and x-rays of the same energy. Rather, gamma rays are distinguished from x-rays by their origin.

X-rays and γ-Rays interaction with matter

Gamma rays are a form of ionizing radiation. They are more penetrating than both alpha and beta radiation (neither of which is electromagnetic radiation), but generally less ionizing. Most gamma rays of 1 MeV energy will pass through 1 cm of aluminium, while an alpha particle with an energy1 MeV will be stopped by even a single sheet of paper [htt04]. In passing through matter, x-rays and gamma radiation ionizes via three main processes: the photoelectric effect, Compton scattering, and pair production.

The photoelectric effect, demonstrated in Figure 1-7, describes the phenomennon in which a gamma or an x-ray photon interacts with and transfers its full energy (hf_{photon}) to an atomic electron, ejecting that electron from the atom.

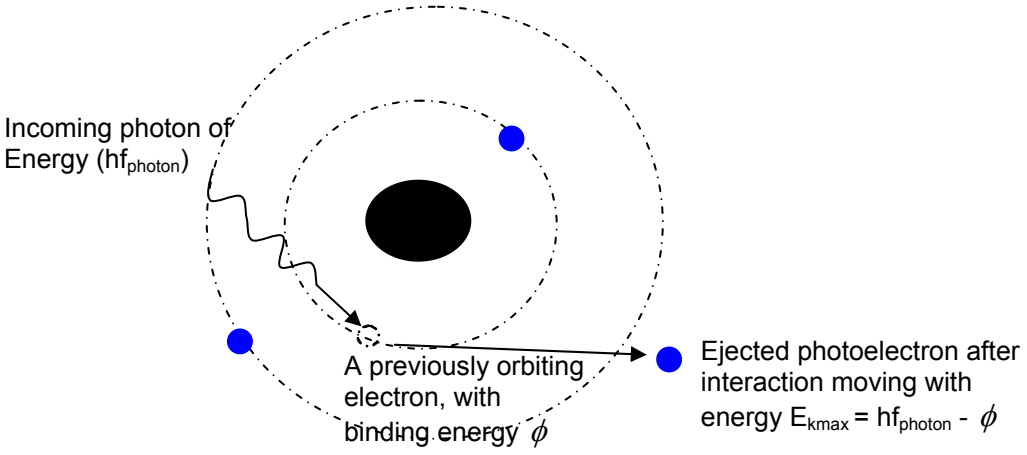

Figure 1-7: Photoelectric effect: Ejected photoelectron after gaining the entire energy of the photon.

The kinetic energy, $E_{kmax,}$ of the resulting photoelectron is equal to the energy (hf_{photon}) of the incident photon minus the binding energy, ϕ of the electron. The photoelectric effect is the dominant energy transfer mechanism for x-ray and gamma ray photons with energies below 50 keV but it is much less important at higher energies [htt08].

The Compton scattering effect, shown in Figure 1-8, is an interaction in which an incident gamma or hard x-ray photon of energy $hf_{photon1}$ loses enough energy to an atomic electron to cause its ejection, with the remainder of the original photon's energy being emitted as a new, lower energy ($hf_{photon2}$) photon and an emission direction different from that of the incident gamma photon.

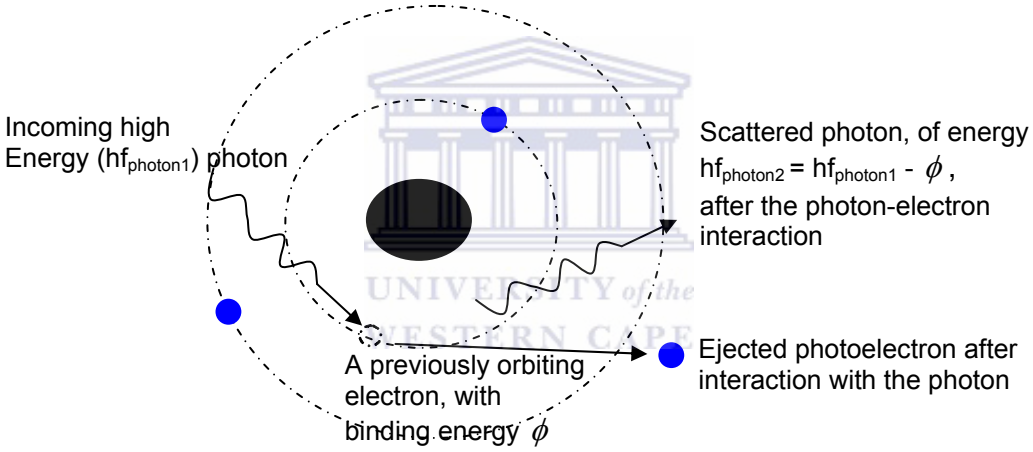

Figure 1-8: Compton scattering effect: Ejected photoelectron and the scattered photon after photon-electron interaction.

The probability of Compton scattering decreases with increasing photon energy. Compton scattering is the principal absorption mechanism for gammas and x-rays in the energy range 100 keV to 10 MeV, an energy range which includes most gamma radiation present in the fission process. Compton Scattering is relatively independent of the atomic number of the absorbing material [htt08], [Lil01].

Pair Production, demonstrated in Figure 1-9, is the spontaneous conversion of the energy of the incident photon into the mass of an electron-positron pair by

interaction via the Coulomb force, in the vicinity of the nucleus. A positron is the anti-matter equivalent of an electron; it has the same mass as an electron, but has a positive charge equal in size to the negative charge of an electron. Energy in excess of the equivalent rest mass of the two particles, i.e. 1.02 MeV, appears as the kinetic energy of the pair and the recoil nucleus. The positron has a very short lifetime, about 10^{-8} seconds. At the end of its range, it combines with a free electron. The entire mass of these two particles is then converted into two gamma photons of 0.51 MeV energy each as discussed above [htt08].

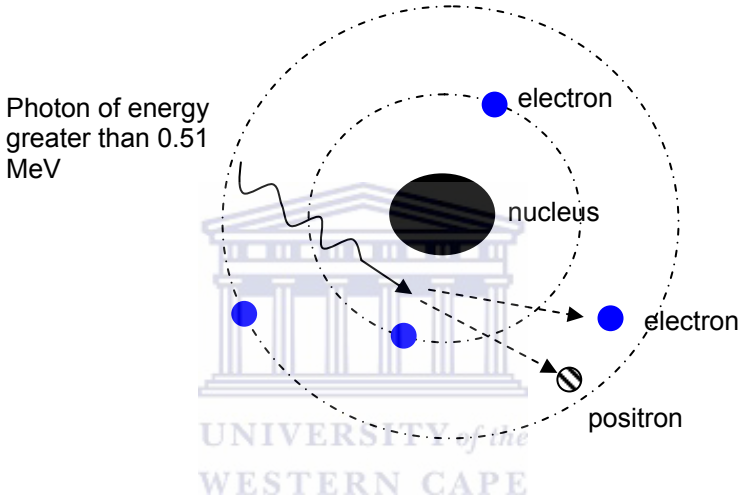

Figure 1-9: Pair Production: The production of the photon-electron pair from the conversion of the photon of energy greater than 1.02 MeV.

These interactions are important for the quality of the radiographs and tomographs. The photoelectric effect provides for a better representation of the sample's properties, owing to the absorption of the entire energy of the photon. With the Compton scattering effect, after partial absorption of the photon's energy, the photon with the residual energy can still be scattered within the material until it gets detected at an arbitrary spot on the detection system.

1.5 Description of Radiation-Based Analytical Techniques.

Radiation-based analytical techniques mentioned earlier in this chapter are theoretically described in this section, except for NRad and NTomo, and, XRad and XTomo. Neutron radiography and –tomography as well as x-ray radiography and -tomography being techniques practically applied in this study, are described and discussed in detail in section 2.4.2. Aspects such as sensitivity, limitation, advantages and disadvantages of the above mentioned techniques regarding the identification of chlorides and chloride effects within concrete, are discussed in section 2.5.

1.5.1 PIXE (Particle induced x-ray emission)

PIXE is a powerful non-destructive elemental analysis technique with basic components being the ion beam source, collimation system, sample stage and detection system. A general configuration of the components of the PIXE system is shown in Figure 1-10.

For a PIXE event to occur, incident particles (usually protons) in the energy range 2 - 5 MeV must excite electrons from core shells of the atoms of the target. When electrons from higher energy levels fall back into lower energy level electron holes, x-rays of energy equal to the energy difference between the two shells are emitted. This phenomenon of electron excitation and x-ray emission is shown in Figure 1-4. Every element emits a unique spectrum of x-rays that can be used to identify elements within the sample. Scanning the proton beam across the surface of the sample enables the mapping of the concentration of each element constituting the material surface. X-ray detection is made possible using Si(Li) detectors.

PIXE has elemental analysis capabilities at penetration depth ranging from 10 to 50 μm depending on the material that constitutes the sample, the energy of the

incident beam and the energy of the characteristic x-rays. It takes 5 to 10 min to generate results with instruments capable of determining concentrations down to 1ppm and some to 1ppb. This technique studie elements of atomic number greater than that of Si and some PIXE instruments are capable of studing elements between Al and U [htt09], [htt10], [htt11], [htt12].

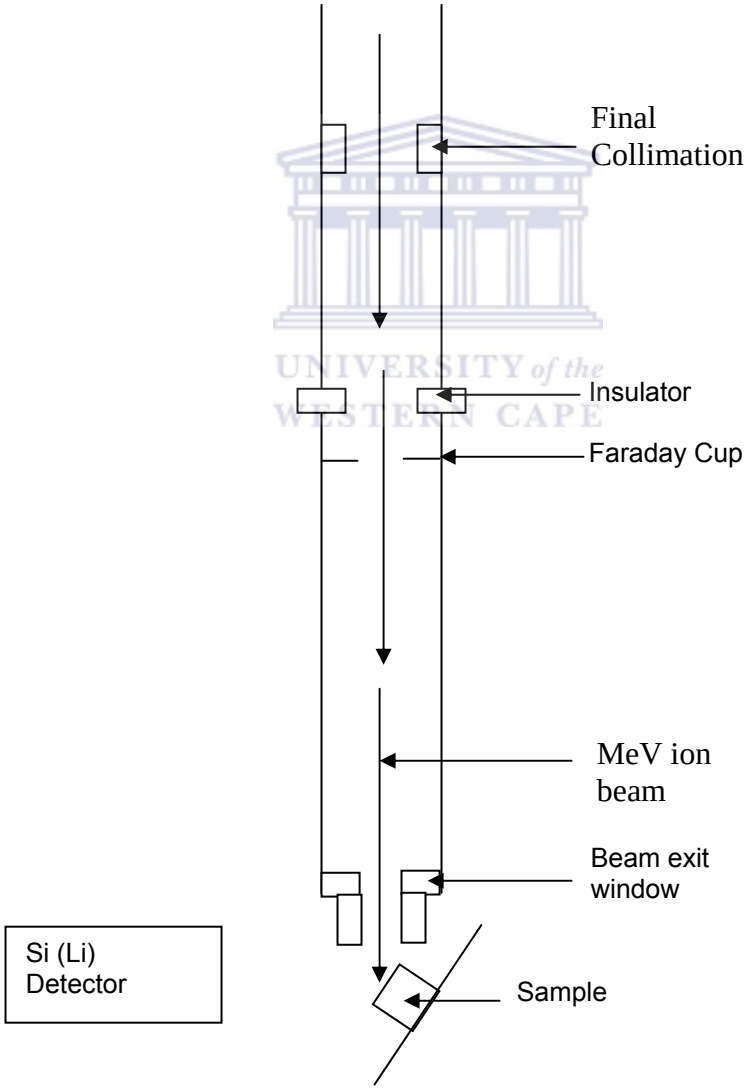

Figure 1-10: The configuration of the components of a PIXE system.

1.5.2 SEM (The scanning electron microscope)

SEM schematically shown in Figure 1-11 [htt35], generates a beam of electrons in a vacuum; the beam is collimated by electromagnetic condenser lenses, focused by electromagnetic lenses, and scanned across the surface of the sample through deflection coils. The imaging method is based on the collection of secondary electrons, inelastically scattered by the incident electron beam and liberated out of the sample surface within 10 nanometers (nm) depth. The secondary electrons are detected by a scintillation material that produces flashes of light, which are then detected and amplified by a photo-multiplier tube. SEM sees applications in materials' surface investigation [Chap86], [htt13], [htt14], [htt15].

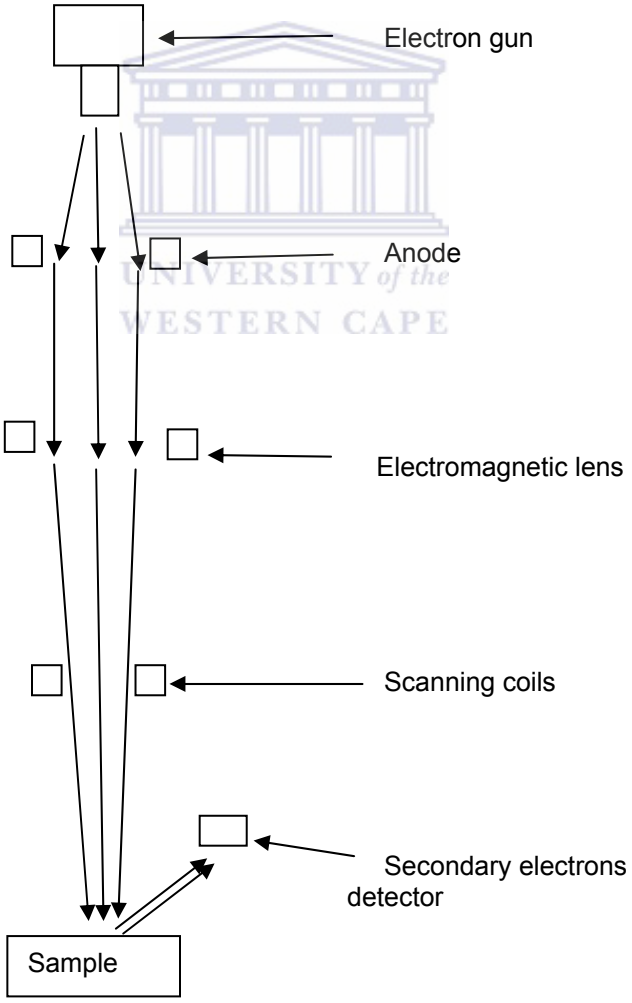

Figure 1-11: The general configuration of the components of the SEM system.

SEM instruments can resolve structures as small as down to 4 nanometers (nm). The incident electron beam can also be elastically backscattered by atoms from within the material and detected after escaping out of the sample surface. These backscattered electrons are used to determine the type of material of the sample, the relation is the higher the atomic number the higher the backscattering coefficient. Backscattered electrons can produce secondary electrons, and have a penetration depth of up to several microns (μm) into the sample, depending on the material and the energy of the incident electron beam.

Both the incident electron beam and backscattered electrons can produce bremsstrahlung and characteristic x-rays. Characteristic x-rays can be used to determine the material of the sample. X-rays can travel at least twice the depth secondary electrons can.

The penetration of incident electron beam, backscattered electrons and the progression of x-rays depends on the energy of the incident electron beam, the material of the sample and the energy of the characteristic x-rays [Chap86].

1.5.3 PGNAA (A Prompt Gamma Neutron Activation Analysis)

PGNAA set-up consists of a neutron source, sample, detection system and shielding as primary components of the system. Figure 1-12 demonstrates the primary components of the PGNAA facility [htt30].

When a sample is irradiated with thermal neutrons, characteristic energy gamma rays from elemental atoms composing the sample are emitted. These gamma rays are referred to as prompt gamma rays and are detected by either a NaI detector or high purity Germanium (HPGe) detector. The detection of prompt gammas is in the form of a pulse height spectrum with different energy gamma rays allocated different channels [Naq06].

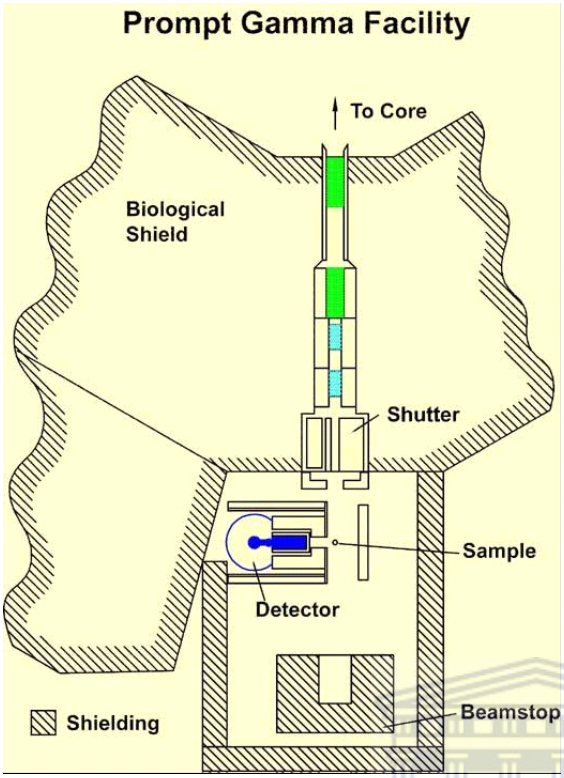

Figure 1-12: Representation of the PGNAA Facility with the nuclear reactor as a neutron source [htt32].

Neutrons can penetrate up to few hundreds of millimeters depending on the material of the sample [htt45] making PGNAA useful for investigation of bulk samples. PGNAA instruments provide information of concentration sensitivity down to 60ppm in the bulk material of the sample [Mic02].

1.5.4 SANS (Small Angle Neutron Scattering)

SANS involves scattering of a beam of neutrons away from the straight trajectory after it interacts with a sample, which can be an aqueous solution, a powder, or a crystal. The scattering angle is small, 0.1-10°, hence the name small-angle. Neutrons are elastically scattered by interacting with the nuclei of the atoms present in the sample, because the nuclei of all atoms are compact, and of comparable size, neutrons are capable of interacting strongly with all atoms. Neutrons interact strongly with hydrogen, the most abundant element.

After neutrons are elastically scattered by a sample, the resulting scattering pattern is analyzed to provide information of the physical composition of the sample [htt16]. Shown in Figure 1-13 is a SANS facility diagram [Ham95], [htt31].

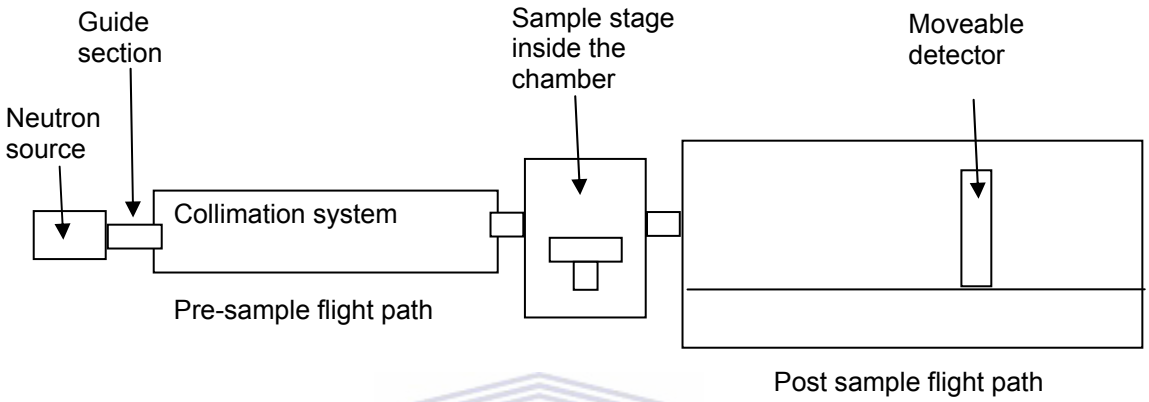

Figure 1-13: Representation of the SANS experimental set-up.

This technique can give information about the size, shape and orientation of a sample. SANS instruments usually uses a gas detector consisting of 128 x 128 cells. SANS instruments can investigate samples of thickness 1-2 mm. The pre-sample and post sample flight paths can have their lengths adjusted to suit desired resolution and beam intensity. Pre-sample flight path can be few tens of meters and post sample flight path several meters. The sample chamber contains a translation table that can accommodate many samples, allowing sequential measurement of samples. Sample chamber can provide sample environments with temperature variations from -150^0C to 200^0C; other sample environments like cryostats, electromagnets, shearing devices, etc, can be provided. SANS instruments based on continuous neutron sources can offer a monochromatic beam, filtered from gammas and epithermal neutrons, through the use of the velocity selector or the crystal monochromators and crystal filters. Time-of-flight SANS instruments use the whole spectral distribution with careful timing between the source chopper and the detector to separate the various

wavelength frames. In the latter, the length of the instrument is determined by the pulse frequency to avoid overlap of frames [Ham95].

1.5.5 X-ray and Neutron Diffraction

These are crystallographic techniques used to determine the atomic arrangement of the sample under investigation. Measurements using these techniques require an x-ray or neutron source, a sample and a detection system. XDIFF reveals the sample's atomic structure in the way x-rays are deflected by electrons of the atoms of the irradiated sample, while NDIFF does in the way neutrons are deflected by the atoms of the material of the sample. The other difference between NDIFF and XDIFF is the sensitivity of neutrons to magnetic forces within the material of the sample. NDIFF measurements are carried out in much the same way as with XDIFF, with a detector moving around the sample, locating the positions of high intensity diffracted beams [Cul78], [htt36].

For x-ray diffraction, a sample to be examined is placed in a monochromatic x-ray beam that gets diffracted in a manner that reveals the sample's arrangement of atoms [htt17]. This generally leads to an understanding of the material and molecular
structure of a substance. The spacing in the crystal lattice can be determined using Bragg's law. The electrons that surround the atoms, rather than the atomic nuclei themselves, are the entities which physically interact with the incoming X-ray photons. X-ray diffraction is commonly carried out using single crystals of a material, but if these are not available, microcrystalline powdered samples may also be used [htt37]. X-rays probe a very thin surface layer of the material (typically tens of microns) [htt44]. Figure 1-4 presents an XDIFF experimental instrument consisting of a source of x-rays, sample stage and a movable detection system [htt32].

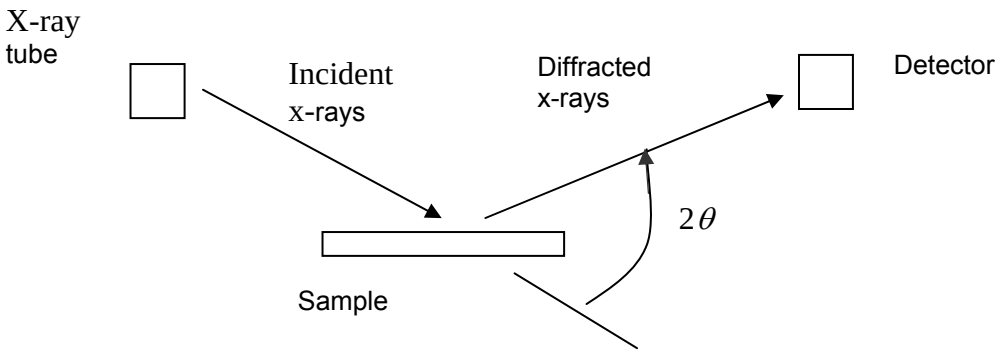

Figure 1-14: Representation of the XDIFF experimental set-up

For neutron diffraction, a sample to be examined is placed in a beam of thermal or cold neutrons, the beam gets diffracted by the sample's arrangement of atoms and the intensity pattern around the sample gives information of the structure of the material. If the wavelength of a quantum particle is short enough, atoms or their nuclei can serve as diffraction obstacle, and neutrons slowed down and selected properly have a wavelength that lies near 0.1 nanometre (one angstrom), the typical separation between atoms in a solid material [Cul78], [htt36]

The Necsa NDIFF facility of the Radiation Utilization group has three diffractometer workstations that do tasks outlined as [htt17]:

- A residual strain instrument
- A four-circle Huber diffractometer for single crystal studies
- A multi detector powder diffraction diffractometer

Shown in Figure 1-15 is the general NDIFF experimental instrument with instrument components configured linearly. The NDIFF is characterized by the neutron source, beam collimation, sample stage and the neutron detection system [htt33].

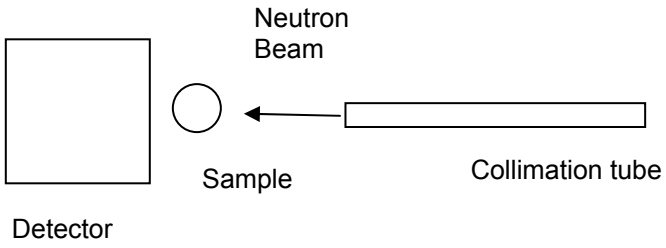

Figure 1-15: Representation of the NDIFF experimental instrument.

The greatest advantage that neutrons have over x-rays is the very large penetration depths, which make them capable of measuring at near surface depths of around 0.2 mm down to bulk measurements of up to few tens of millimeters depending on the material of the sample, e.g. 70 mm in aluminum or 37 mm in steel [htt45].

Chapter 2: Background to the study of concrete

In this chapter the following are discussed: Definition of concrete deterioration (section 2.1), causes of concrete deterioration (section 2.2), chloride ions (section 2.2.3), identification of concrete's deterioration (section 2.3), methods to determine concrete deterioration (section 2.4), attenuation of neutrons and x-rays (section 2.5), literature review of radiation-based techniques to investigate chlorides and the effects of chlorides within concrete (section 2.6), theoretical feasibility study of the x-rays and neutron based techniques (section 2.7).

2.1 Definition of concrete deterioration

The failure of concrete is caused by the degradation of components that give concrete its strength. This degradation is the leaching of the cement paste material, cracking of concrete and corrosion of steel reinforcement. The corrosion and the rate of corrosion of steel reinforcement are influenced by the concentration of contaminant chemical elements and the rate of absorption of liquids that contain contaminant chemical elements, oxygen and moisture [Nac05]. The degree of liquid absorption depends on the pore size and pore connectivity [Mar97], the rate at which the cement paste is leached, and cracks probably caused by corroded steel.

2.2 Causes of concrete deterioration

Although concrete is considered to be a durable material it is subject to deterioration caused by a number of factors which range from poor workmanship, poor material composition up to environmental effects [htt03]. Chlorides have been, based on practical conducted work, accepted as being of great influence

on the rate of corrosion; the presence of chlorides in concrete speeds up the rate of steel corrosion [htt01], [Ale99], [Naq06].

2.2.1 Materials and Workmanship

Concrete may experience deterioration caused by materials containing contaminants and used in the mix or by errors that occurred in mixing, forming or placing. Materials and workmanship problems include: (a) improper aggregate, (b) alkali-aggregate reactions, (c) improper aggregate sizing, (d) calcium chloride or similar salt additives, (e) incomplete consolidation in tamping (voids and honeycombs), (f) placement of reinforcing steel too close to the surface, (g) improper handling of cold or weak plane joints, and (h) inadequate curing.

2.2.2 Environmental Factors

Environmental effects associated with concrete deterioration depend on factors ranging from underground (soil), the earth's surface (seawater), and atmosphere. Of the three, seawater provides for an effective transportation of chlorides into concrete structures. Figure 2-1 demonstrates the effects of seawater on a concrete structure. It shows that concrete structure submerged under seawater is more prone to chemical decomposition of the cement.

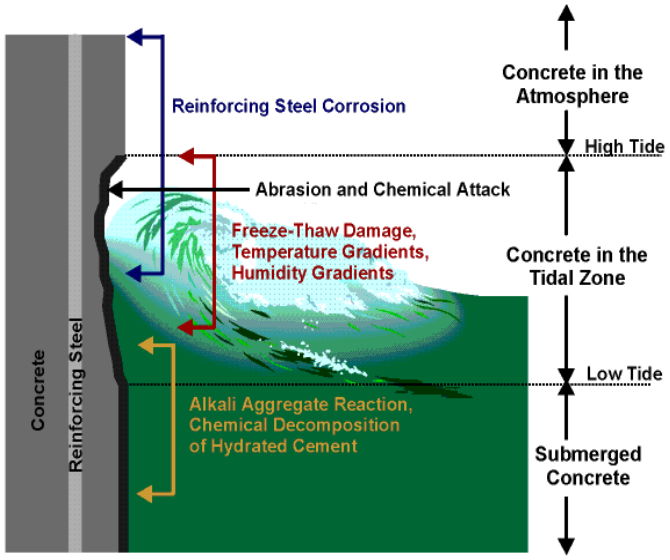

Figure 2-1: Diagram demonstrating general seawater environmental effects associated with concrete deterioration [htt45].

The figure demonstrates that the tidal level zone of the concrete structure is more prone to fractures and spalling due to temperature gradients and extreme temperature ranges that cause freeze-thaw cycles; where moisture absorbed by the concrete expands and contracts with temperature changes and the resulting mechanical action.

Airborne components, such as carbon dioxide, can cause adverse chemical reactions which can cause surface deterioration and steel corrosion.

2.2.3 Chloride ions

Chlorides present within steel reinforced concrete enhance the propagation of corrosion and rate of corrosion of steel. Chlorides are capable of destroying a protective layer that steel develops on its surface to prevent propagation corrosion deep into steel matter [Nac05]. Steel is an alloy of iron, and primarily consists of iron and corrodes to oxides and hydroxides of iron. Some of the chemical processes through which steel corrodes are [htt18]:

$$4Fe + 3O_2 \longrightarrow 2Fe_2O_3 \quad \text{(Eq 2-1)}$$

$$2Fe + 3H_2O \longrightarrow Fe_2O_3 + 3H_2 \quad \text{(Eq 2-2)}$$

$$2Fe + O_2 + 2H_2O \longrightarrow 2Fe(OH)_2 \quad \text{(Eq 2-3)}$$

Sources of chloride ions are [htt24], [htt25], [Cod96]:

- Sea Water 2.6% NaCl
- Soil
- Human Body fluids
- Deicing Salts for road deicing

The phenomenon of corrosion of steel is not well understood at this point in time. For example, soil corrosion cannot be fully represented in terms of chemical formulas.

2.3 Identification of concrete deterioration

Concrete deterioration may be observed firstly by eye and quantitatively determined through field and/or laboratory testing methods [htt03], [htt07].
Six prominent reinforced concrete deterioration mechanisms have been identified.

2.3.1 CRACKING

The types and severity of cracks in concrete are varied and include dormant and active cracking. Dormant cracking is caused by shrinkage during curing and is not a cause for concern except for potential moisture infiltration. Inactive or dormant cracking usually requires observation and limited corrective action to prevent moisture infiltration. Active cracking is more serious and can indicate severe problems. Active cracks show movement and are related to structural overloading, foundation settling, inherent design flaws, or other deleterious conditions. Active cracking can be temporary or continuous. It requires monitoring and may require corrective action. Random surface cracking, or crazing, may indicate an adverse reaction between cementitious alkalis and aggregates and requires surface corrections. Figures 2-2 and 2-3 demonstrate minor and major cracks respectively.

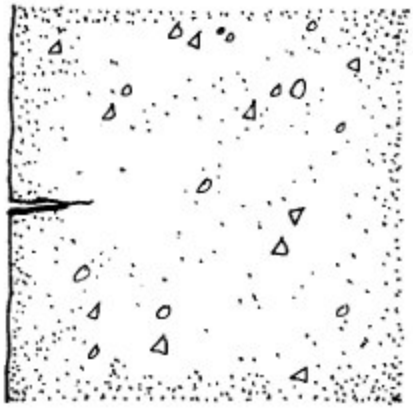

Figure 2-2: A small surface crack in concrete.

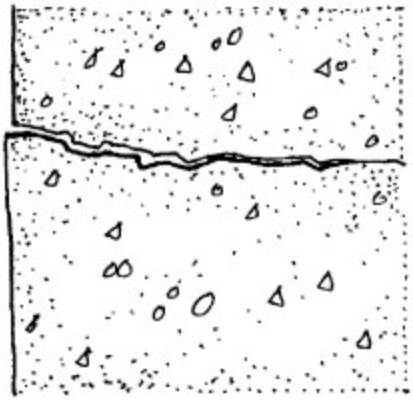

Figure 2-3: Structural crack through concrete showing displacement.

2.3.2 SPALLING

Surface concrete loss in pieces of various sizes is called spalling and is caused when expansive forces inside and near the surface of concrete act along a weak plane or create a weakened plane. The expansive force can be caused by the stress of corrosion of reinforcing steel or imbedded metal items (see Figure 2-4). Corrosive oxidation (rust) causes expansion which in turn creates additional stress. Internal expansion can also be caused by moisture absorbed by porous aggregates that expand and contract in thermal cycles. Moisture may be trapped inside the matrix of the concrete by paints or sealants that do not allow moisture to migrate and escape at the surface. Spalling can also occur due to a condition called laitance where concrete, during placement, was mixed too wet and cement rich paste rises to the surface of the concrete thereby depriving other portions of the mix of cement-related cohesion and consolidation.

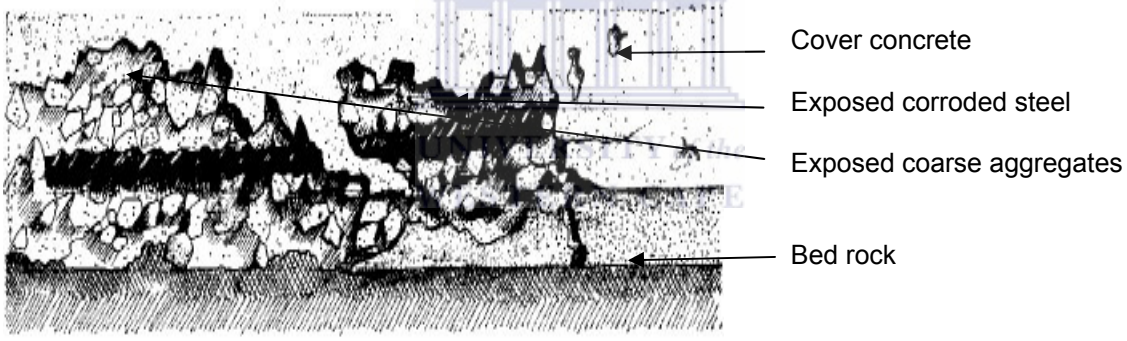

Figure 2-4: Spalling mainly caused by expansive corrosion acting on reinforcing steel.

2.3.3 DEFLECTION

Concrete footings, foundations, beams, columns, slabs, and walls are subject to deflection that can be seen in bending, bowing, or sagging. Deflection can be caused by overloading, the effects of corrosion, inadequacies in original construction, seismic stress, and by long-term shrinkage. Deflection, by creating internal stress within a concrete mass, may cause spalling at the concrete's extreme surfaces. Most design standards rate structural failure as deflection exceeding about a 2.5 cm drop over a length of 10 m.

2.3.4 STAINS

Stains on concrete surfaces that are not purposely applied, may indicate internal problems such as corrosion or adverse chemical reactions. Corrosion usually involves reinforcing steel and the resulting stains are rust-colored. Alkali-aggregate reactions are usually seen as a white efflorescence. Moisture-related stains may appear as a variety of colors.

2.3.5 EROSION

Weathering of concrete surfaces by wind, rain, snow, or other mechanical action can cause surface loss. Temperature related expansion and contraction of surface moisture exerts a mechanical action and results in the gradual wearing away of the concrete surface. Exposed aggregates are particularly susceptible to differences in the rates of expansion among the various constituent materials.

2.3.6 CORROSION

Reinforcing steel that has been placed too close to the surface of the concrete or that has been exposed by spalling, erosion, or cracking, can corrode or rust due to oxidation of the steel in the presence of moisture. The presence of salt-rich moisture adds to the rate of corrosion (deterioration). Corrosion is an active chemical process that exerts its own expansive stress. High alkalinity in the concrete promotes corrosion and causes, in addition to expansion, a loss of surface bonding between steel and concrete. This loss of bonding reduces the unified effect of reinforced concrete to resist tensile and compressive forces.

2.4 Methods used to determine concrete deterioration

2.4.1 Method 1: Engineering methods

Inspection and Testing [htt06], [htt07].

Determining the causes of concrete deterioration requires careful analysis by experienced architects and structural engineers. Structural deterioration can have

life-safety implications and threaten a structure's existence. In addition to inspection and observation by experienced professionals, materials testing and analysis is needed. Procedures for testing and inspection involve field analysis and documentation, review of documents, testing, monitoring, and laboratory analysis [htt06], [htt07].

Testing and Inspection Procedures

(1) FIELD ANALYSIS

This is the activity of conduction of onsite visual inspection to locate the nature and extent of concrete deterioration.

(2) DOCUMENT REVIEW

This is an activity of reference to original drawings and engineering reports in comparison to field data. Checking of historic records and photographs for further information to reveal progress of deterioration, is conducted.

(3) FIELD TESTING

If required, after visual inspection, a testing program that involves both on-site testing followed by laboratory testing and analysis is instituted to determine the nature and extent of deterioration. On-site testing includes the use of:

a) calibrated metal detectors, sonic meters, and other devices to locate imbedded metals.
b) sounding hammers and chains to locate voids.
c) direct application of controlled water spray to determine moisture penetration.
d) a moisture meter to determine presence and extent of moisture in concrete.
e) computer simulation and test models to calculate deflection.
f) a transit for deflection measurement.

(4) LABORATORY TESTING AND ANALYSIS

Samples taken from fieldwork are subject to certain laboratory tests such as:

a) Compressive strength testing.

b) Mix composition analysis by weight and volume.

c) Chemical reaction analysis testing for alkalinity, carbonation, porosity, chloride presence, and other components.

Analysis of field data, inspection reports, documents, and testing data requires careful and thorough analysis by structural and materials testing by engineers to determine the exact scope of corrective action. This is particularly important where historic concrete is involved. Since improper repairs can cause additional deterioration, no action may be preferable to improper measures.

2.4.2 Method 2: Non-invasive Neutron and X-ray, Radiography and Tomography

This study involves experimental application of NRad, XRad and NTomo as discussed in this section. Radiation attenuation constitutes a very important part of radiography and tomography, hence it is discussed in this section as an introduction to radiography and tomography.

2.4.2.1 Attenuation of Neutrons and X-rays

When incident on an object, radiation interacts with the particles of the material and has a probability to be absorbed, scattered or/and transmitted. The combine effect of absorption and scattering is called attenuation and the principle is schematically shown in Figure 2-5.

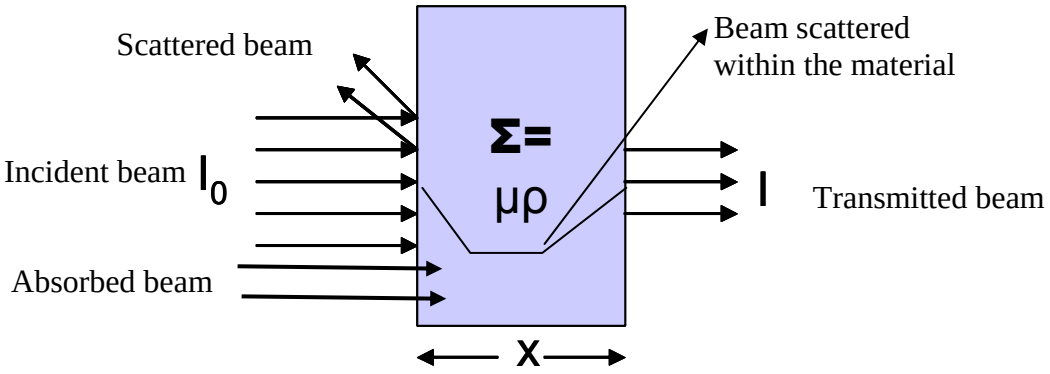

Figure 2-5: Schematic presentation of the radiation attenuation relation.

Neutrons have a random arrangement of attenuation coefficient as a function of the atomic number; whilst x-ray attenuation values systematically increase smoothly with atomic number (see Figure 2-6). The reason for this difference in behavior of attenuation of neutrons and x-rays is that, x-rays interact with atomic electrons whilst neutrons interact with the nucleus. Radiation attenuation (absorption and scattering) is common for all sources of radiation.

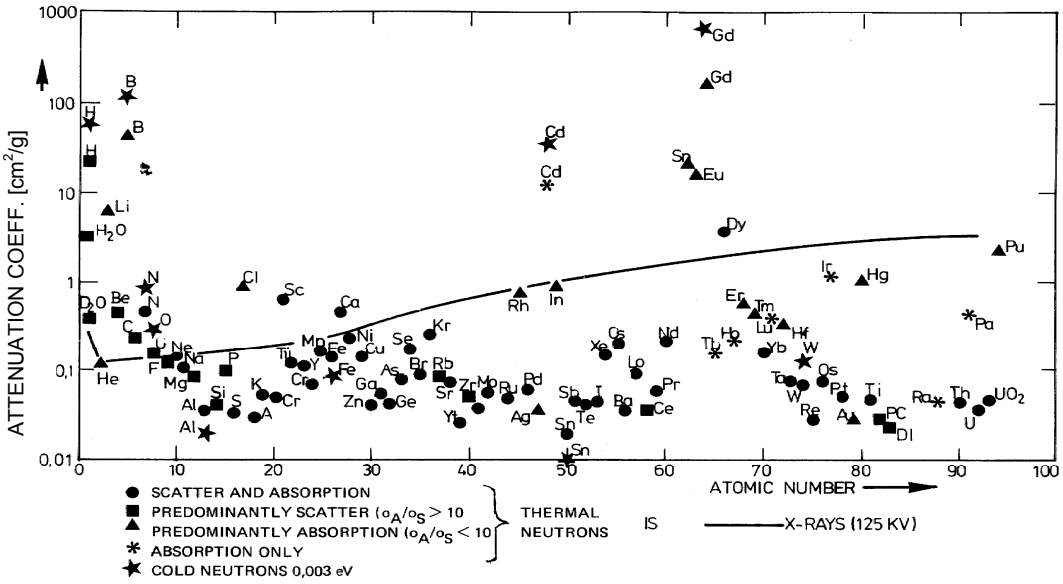

Figure 2-6: Mass attenuation coefficients ($cm^2.g^{-1}$) for thermal and cold neutrons, as well as for X-rays (125kV)-solid line- as a function of the atomic number of elements between 1 and 100 [Bay92].

Figure 2-6 shows that the attenuation coefficient values for elements or compounds generally decrease with increase in energy of the x-rays and neutrons. The amount of radiation transmitted through a material depends on the thickness traversed, density and attenuation coefficient, the type of radiation as well as its energy.

The factor that indicates how much attenuation will take place per cm of pathlength through the material (the probability of radiation to be absorbed and/or scattered) is known as the linear attenuation coefficient [Bay92], [htt07].

The relation of attenuation of any type of radiation is given by:

$$I_{transmitted} = I_0 e^{-(\Sigma_m x)} \qquad \text{(Eq 2-4)}$$

where, $\Sigma_m = \mu_m \rho_m$

Σ_m - macroscopic cross section of the atoms of the sample, in a cm^3 of the sample's solid matrix.(cm^{-1})

μ_m - mass absorption coefficient of the atoms of the sample. ($cm^2.g^{-1}$)

ρ_m - density of the material of sample. ($g.cm^{-3}$)

x - thickness of the sample. (cm)

I_0 - pixel intensity value of the incident radiation beam without attenuation by the sample.

$I_{transmitted}$ - pixel intensity value of the beam transmitted through the sample.

2.4.2.2 Radiography

Radiography is an imaging method that uses penetrating radiation to produce 2-D images called radiographs, from samples under investigation. The geometry layout requires a radiation source, collimator system and detection system as schematically shown on Figure 2-7.

This figure demonstrates that the sample volume with the defect inclusion allows either more or less radiation to pass through it than does the volume of the sample without a defect.

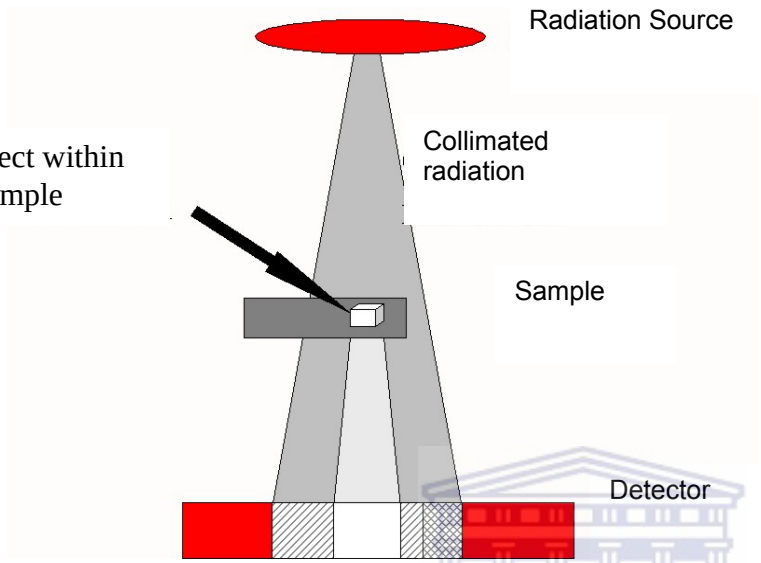

Figure 2-7: Basic components and principle of radiography

Radiation detection is conducted using radiation sensitive films or modern electronic detection devices. Figure 2-8 presents the penetrating radiation detection process made possible through the scintillator screen, charge coupled device (CCD) being the camera and computer with a frame grabber.

The electronic or digital image (radiograph) is compiled from the radiation transmitted through the object under investigation, that is converted by the scintillator screen to visible light that is captured by the camera as a photo image and displayed on the computer monitor. The image formed with a scintillator screen is a positive image where brighter areas on the image indicate that higher intensities of transmitted radiation reached the screen. The image is opposite to the negative image produced in film radiography.

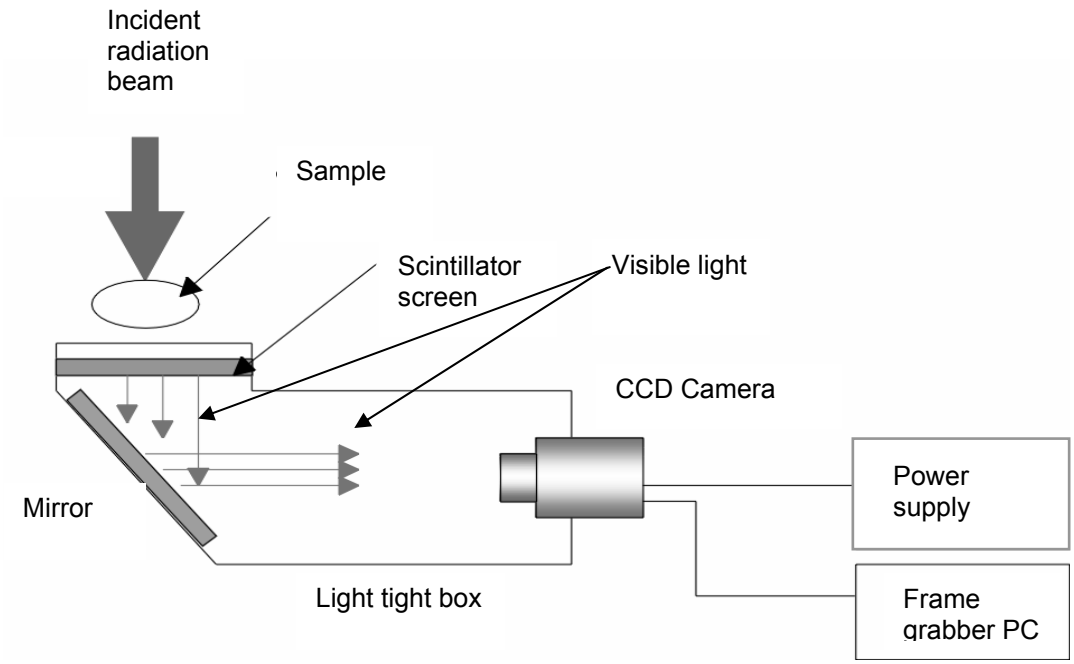

Figure 2-8: Schematic diagram of a camera based detection system.

2.4.2.3 Tomography

Tomography is a software based technique that produces 3-D images from the reconstruction of multiple radiograms (projections) of a sample acquired with up to 400 angular rotation steps between 0^0 to 180^0. A simplified layout of the radiography/tomography facility is shown in Figure 2-9.

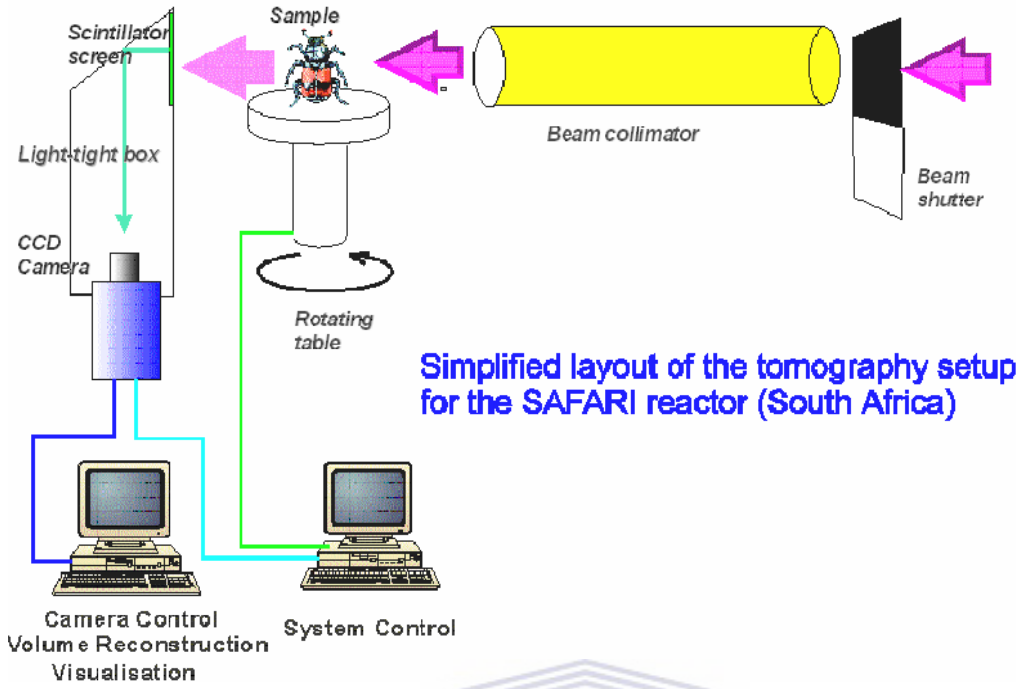

Figure 2-9: A schematic diagram of the layout of the Radiography and Tomography Facility at Necsa [Bee5A].

The sample (non-human) is placed on a rotary table in front of an imaging system. The turntable can be stepwise rotated to up to 360^0. For maximum resolution, the number of angular projections must be equal to the number of pixels that constitute the longest dimension of the sample's image. At each angle a 2-D radiogram or projection is captured as explained earlier in this section. The turntable and the imaging system are connected to a computer so that 2-D radiograms collected can be correlated to the angular position of the test component.

3-D images (Tomograms) are obtained from the reconstruction of radiograms into 3-D images using appropriate computer software packages [htt20] [htt19].

Characteristics of the internal structure of an object in 3 dimensions such as size, shape, internal defects and density are readily available from tomography images.

2.4.2.4 Neutron Radiography

Neutron radiography is a non-destructive test method whereby a 2-D radiograph of a sample is produced by means of neutrons. To produce a radiograph, incident neutrons are attenuated to different degrees by different materials within the sample being investigated. After attenuation, transmitted neutrons are then detected with the detection system which then forms and capture a photo image that is displayed on the computer monitor. Thermal neutrons are recommended for radiography work, because of their good discrimination capability between different materials. For electronic imaging of neutron beams a 6LiF/ZnS:Cu,Al,Au scintillator screen is required [Bee05].

2.4.2.5 X-ray Radiography

X-ray radiography is similar to neutron radiography with the same facility layout, in terms of components involved in beam conditioning and image detection, but an x-ray source is used instead of the neutron source as well as a different scintillator screen. X-ray radiography is used for medical scans as well as for industrial purposes. X-ray medical scans are widely known, but industrial radiographs are relatively less well known. Figure 2-10 presents an x-ray radiograph acquired for industrial purposes. It can be seen in the figure that the material used for welding attenuates x-rays to a different degree compared to the parent pipe material. For electronic imaging, x-ray radiography requires the use of a gadolinium oxysulfide, Gd_2O_2S scintillator screen to transform x-rays to visible light [htt22].

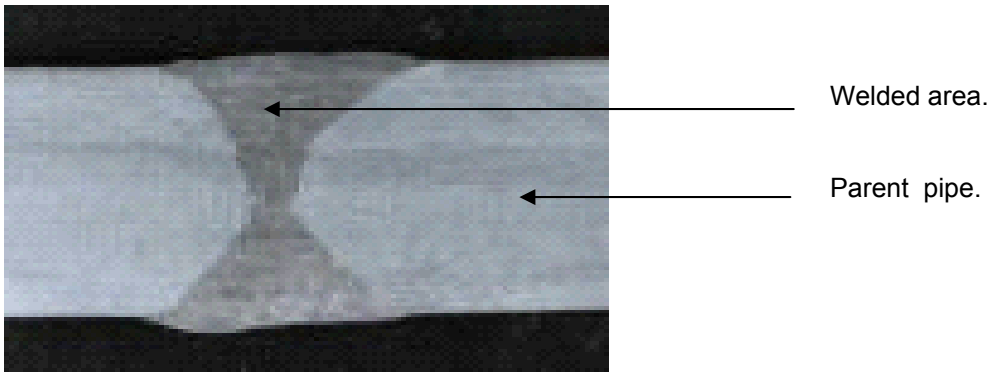

Figure 2-10: An x-ray radiograph of a welded area in a metal pipe.

2.4.2.6 Neutron Tomography

Neutron Tomography is a powerful non-destructive evaluation technique utilizing 2-D images to produce images that can be transformed using software into 3-D cross-sectional images of a test object. Application of neutron tomography in the study of concrete deterioration has been used to determine only some factors [Bee05], [Mil04], [Gerde]. These applications focus on visualization of liquid within the concrete.

Shown in Figure 2-9 is a schematic diagram of a neutron tomography system which is similar to an industrial x-ray tomography system, but with (a) a neutron source and (b) 6LiF/ZnS:Cu,Al,Au scintillator screen instead of an x-ray system elements.

2.4.2.7 X-ray Tomography

Computer assisted x-ray tomography for industrial purposes (commonly known is CAT scanning which is for medical purposes) works on similar principle as the neutron tomography with inclusion of a different scintillator screen suitable for x-rays absorption, and an x-rays source. This technique, shown on Figure 2-11, is extensively used for medical diagnostic purpose.

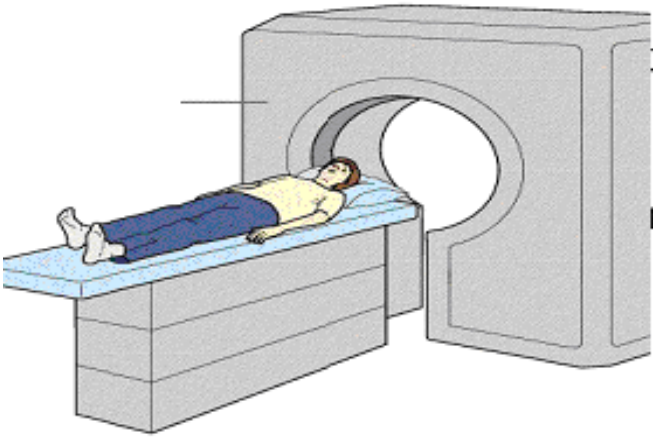

Figure 2-11: A diagram of the layout of CAT medical system.

Neutron radiography and tomography are used mainly as non-destructive analytical techniques in research and development as well as specific industrial applications while x-ray radiography and tomography are used in both industrial and medical diagnostic applications.

2.5 Literature review of radiation-based techniques to investigate chlorides and the effects of chlorides within concrete.

In this section a literature review account is given of studies in which radiation-based techniques are discussed regarding their capability to identify chlorides and study the effects of chlorides within concrete. A principal effect of chlorides on steel reinforced concrete is the acceleration of corrosion of the steel within the concrete structure, and its severe effect on concrete strength that leads to concrete deterioration. Knowledge of the corrosion rate of steel embedded in concrete is essential to civil engineers, constructors and architects. If steel embedded in concrete can be imaged, then the corrosion rate can be determined to a better confidence level.

2.5.1 Investigation for chlorides within concrete samples

Study 1- PGNAA

This section discusses the published work by Naqvi [Naq06] that presents the capabilities of PGNAA to investigate chlorides within concrete.

PGNAA is an established analytical technique for elemental composition of concrete [Col95], [Khe99], [Lim01]. In the study by Naqvi, PGNAA has been used to determine chloride concentration in laboratory concrete samples exposed to varied chloride concentrations with range 0.5, 1, 1.5, 2 and 3 %wt [Naq06]. Table 2-1 summarizes the elemental composition of their concrete samples. The results give an almost 100% correlations between known calcium and silicon concentration, and the prompt gamma ray experimental yield. Results from these elements were used as a measure to calibrate their instrument.

Table 2.1: Elemental composition of four concrete samples investigated by Naqvi.

Element (%wt)	Sample 1	Sample 2	Sample 3	Sample 4
H	0.9461	1.026	1.237	1.106
C	5.5086	5.976	3.728	6.325
O	50.9105	52.19	51.768	50.638
Na	0.0594	0.058	0.07	0.048
Mg	0.3378	0.276	0.359	0.368
Al	0.6456	0.494	0.811	0.629
Si	14.9212	15.306	18.881	10.228
S	0.2453	0.187	0.271	0.273
K	0.1606	0.162	0.187	0.127
Ca	25.7398	23.932	22.059	29.707
Ti	0.0277	0.027	0.027	0.027
Fe	0.4975	0.364	0.6	0.524

After the instrument had been calibrated, it was used to investigate known chloride concentrations of 0.5, 1, 1.5, 2 and 3 %wt in concrete. It is noted in Figures 2-12 and 2-13 that three chloride peaks, i.e. 1.164, 6.62 and 7.41 MeV, could be used to determine chloride concentrations in concrete. Interferences of chloride peaks with calcium peaks in energies above 3 MeV were reported, and zero interference of the 1.164 MeV chloride peak was also reported.

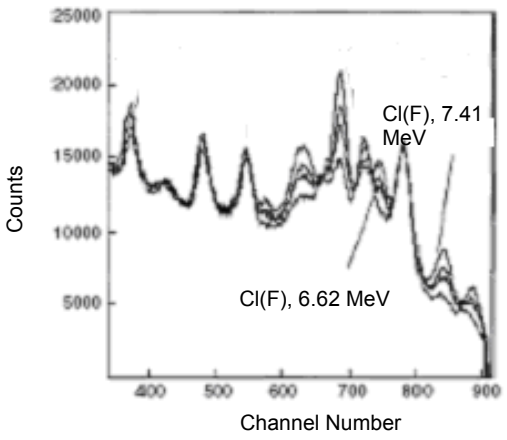

Figure 2-12: Prompt gamma ray spectra of four concrete samples, above 3 MeV, for 0.5, 1.5, 2.0, 3.0 %wt chloride concentration.

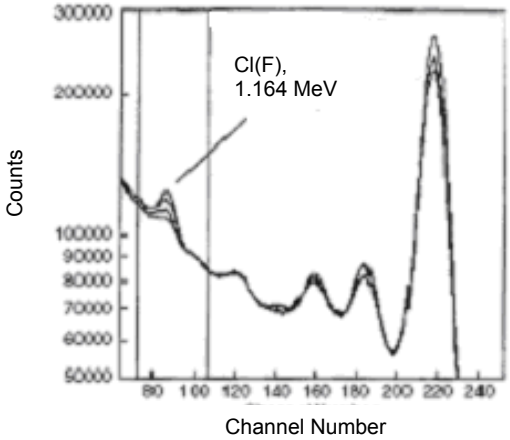

Figure 2-13: Prompt gamma ray spectra of four concrete samples, below 3 MeV, for 0.5, 1.5, 2.0, 3.0 %wt chloride concentration.

Study 2: PIXE AND SEM

In the study reported by Kathikeyan and Saroja in an IGC (International Guild of Coaches) newsletter in 2005 [Kat05], a study of chloride distribution within concrete samples as well as predicting the time dependence of chlorides redistribution was conducted. After time was allowed for the redistribution of chloride ions to occur, concrete specimens were sampled from different depths into the concrete structure. These specimens were examined using SEM and PIXE, as well as chemical methods for ion concentration determination. SEM used for this work employed an energy dispersive x-ray analyzer (EDXA). Figure 2-14 presents a summary of results on the distribution of chlorides within a concrete slab, obtained through chemical precipitation method. The zero point on the x-axis is the reference point from where the source of chlorides was in contact with the concrete structure. Negative numbers represents a part of the structure buried under geological formation and the positive numbers represents the part of the structure exposed to the atmosphere. The shortcoming of this study is that the chloride concentration is obtained from specimens drilled from different depths into the concrete slab (analytical techniques used in this study could penetrate only so much), which makes this method destructive.

Drilled core specimens investigated with PIXE were also used for SEM investigation.

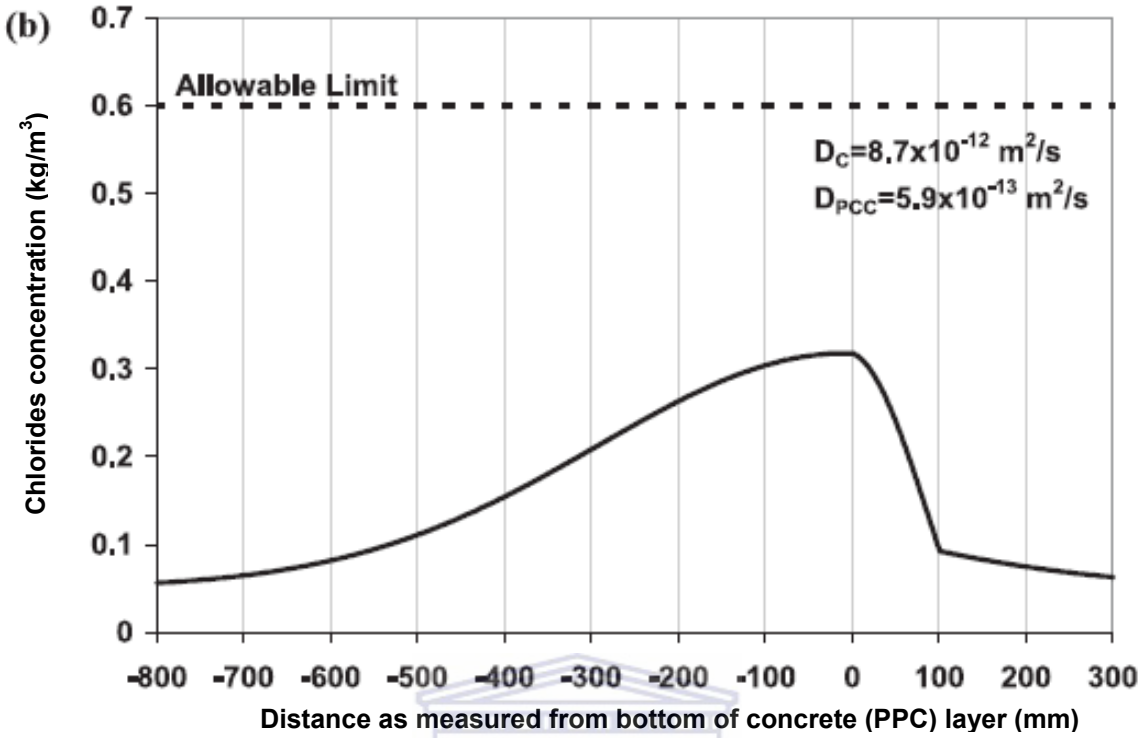

Figure 2-14: Chloride concentration profiling in concrete (PPC) sample, after redistribution of chlorides from one point (0 mm) inside the concrete.

PIXE

Figure 2-15 shows the spectra obtained from specimen obtained at different depths of the concrete sample, cured in seawater, after sectioning starting from the surface. The important feature of these spectra is the decrease in chlorine concentration with distance of the point of contact of the concrete structure with chloride source. This experimental work was conducted to study the penetration character of chlorides into concrete. A chloride peak was identified at 2.62 keV $K_{\alpha 1}$ x-ray energy on the spectrum and was used to determine presence of chlorides.

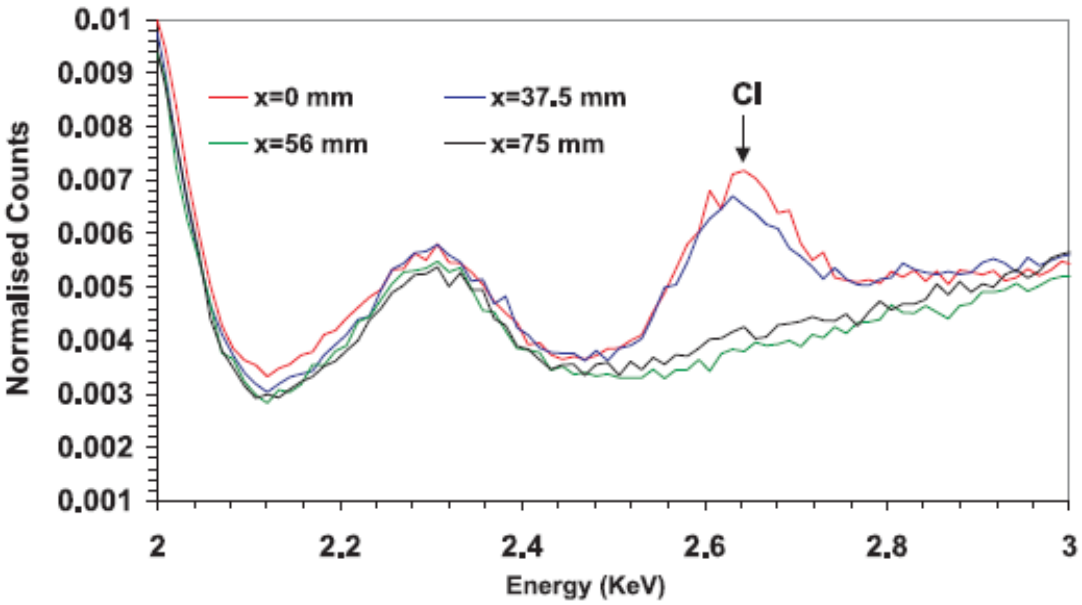

Figure 2-15: Chloride concentration profiling in concrete sample using PIXE at 0, 37.5, 56.0 and 75 mm depths.

SEM

Shown in Figure 2-16 is the EDXA spectra obtained from the cement paste of concrete cured in seawater as well as that of the concrete sample cured in normal water. The reference sample is the sample cured using normal water. A chloride peak at 2.62 keV photon energy was identified on the spectrum. The reference sample spectrum does not have a chloride peak. This study was conducted to verify that the chloride accumulation observed in Figure 2-15 were due to concrete submersion into seawater.

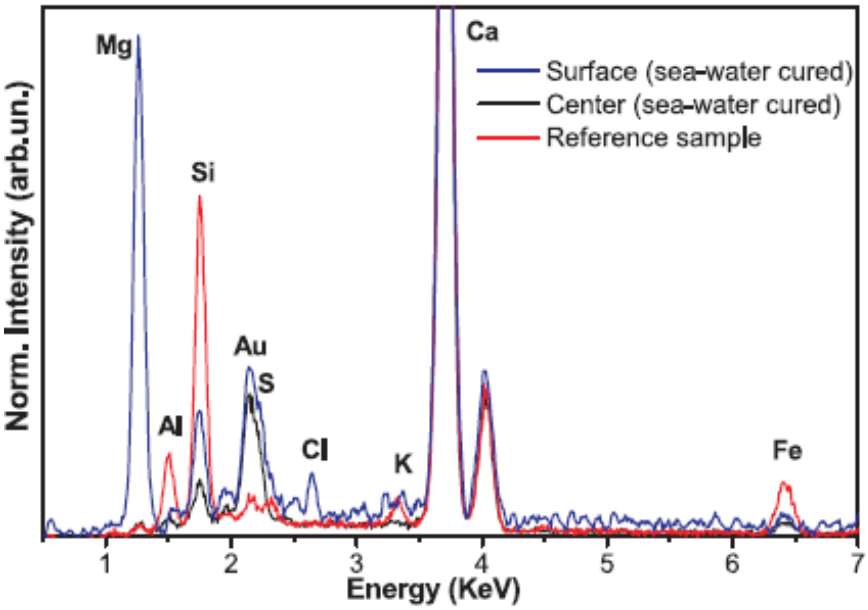

Figure 2-16: EDS spectra for sea water cured concrete's surface and center locations compared with a sample cured in fresh water.

2.5.2 Identification of chlorides effect within concrete samples

Study 1: X-ray diffraction

Nachiappan [Nac05] studied the rate of corrosion of two kinds of steel, chromium rich and conventional (low carbon), under exposure to NaCl solutions. This study was divided into two components, (1) study of corrosion rate of isolated steel rods in NaCl solutions and the (2) study of corrosion rate of steel embedded in concrete. X-ray diffraction was used for the analysis of corrosion products on the corroded steel reinforcement after the concrete sample had been broken. Using x-ray diffraction, it was found that these two kinds of steel formed different corrosion products. Chromium rich steel formed hematite (Fe_2O_3) and conventional steel formed magnetite (Fe_3O_4), while both formed some lepidocrocite (FeOOH). It was also found that conventional steel corroded faster than chromium rich steel in both 1.7 and 3.0%wt[NaCl] solutions.

2.6 Feasibility study of the X-rays and Neutron based techniques

A feasibility study on the attenuation coefficients was undertaken for radiation-based analytical techniques that were available for the experimental work of this study. Neutron-based tools demonstrated huge potential while x-ray-based tools only demonstrated good potential as far as chloride detection in water is concerned.

NRad has been established as far as the visualization and quantification of hydrogen containing liquids within porous media is concerned [Bee04], [Bee4A], [Bee05], [Gerde] [Lunat], [Mid05], [Mil04], [Nor00]. Successful application of XTomo to study density variation of materials has also been reported [Burch].

There is a need to theoretically examine x-ray radiography and tomography, and, neutron radiography and tomography capabilities to produce required results before applications of suggested tools. This exercise assists in determining if it is worth conducting experimental work with applications of the suggested tools. Based on capabilities shown by x-ray radiography and tomography, and, neutron radiography and tomography, it is worthwhile to conduct experimental work using these techniques as discussed below.

2.6.1 X-rays attenuation coefficients

This part of the study discusses x-ray attenuation coefficients for chlorides, water and concrete to determine the x-rays energy most suitable for chlorides investigation within concrete samples. The mass attenuation character as function of x-ray energy for chlorine, sodium, water, as well as silicon and calcium as these are primary constituents of concrete as shown in Table 2.1 [Naq04], [Naq06], is presented in Figures 2-17 to 2-21 respectively. Mass attenuation coefficients for chlorine, sodium, water, silicon and calcium at 3.0 keV are $1.47x10^3$, $5.07x10^2$, $1.93x10^2$, $9.78x10^2$ and $2.68x10^2$ cm^2/g respectively. At

3.0 keV x-ray energy (indicated by lines on Figures 2-17 to 2-21), only silicon attenuates almost as much chlorine does. This means that at this x-ray energy, chlorine has a better influence on the contrast of the radiogram than at lower or higher energies.

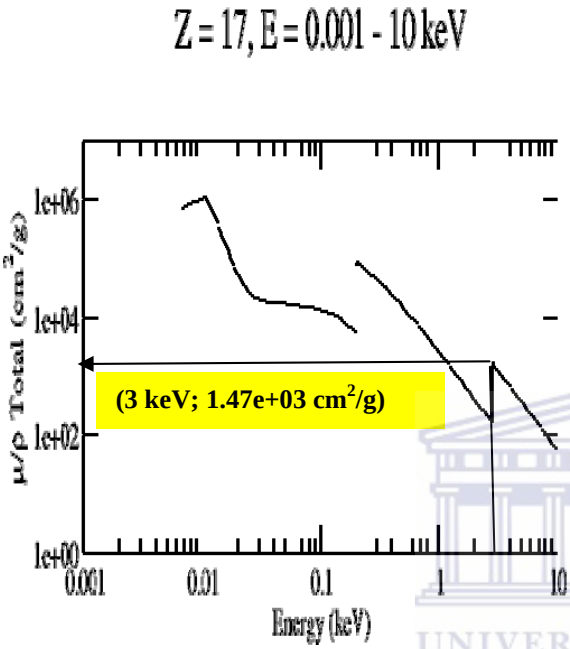

Figure 2-17: Mass attenuation coefficients of chlorine at different x-ray energies.

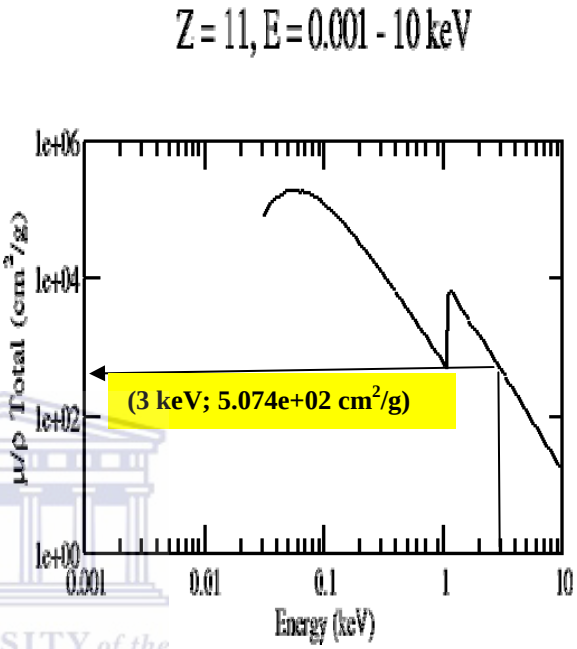

Figure 2-18: Mass attenuation coefficients of sodium at different x-ray energies.

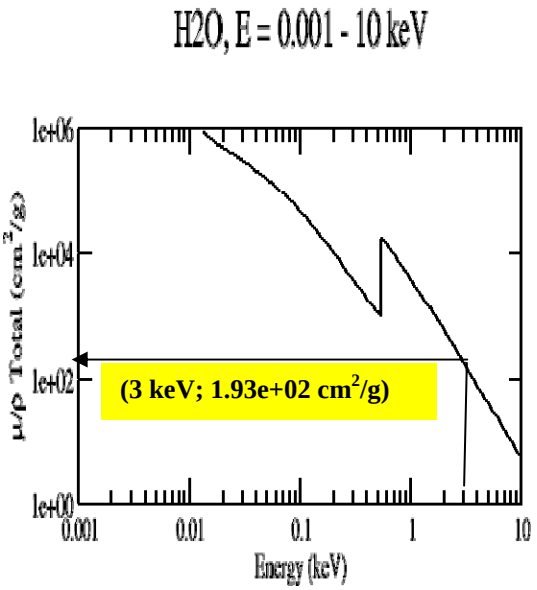

Figure 2-19: Mass attenuation coefficients of water at different x-ray energies.

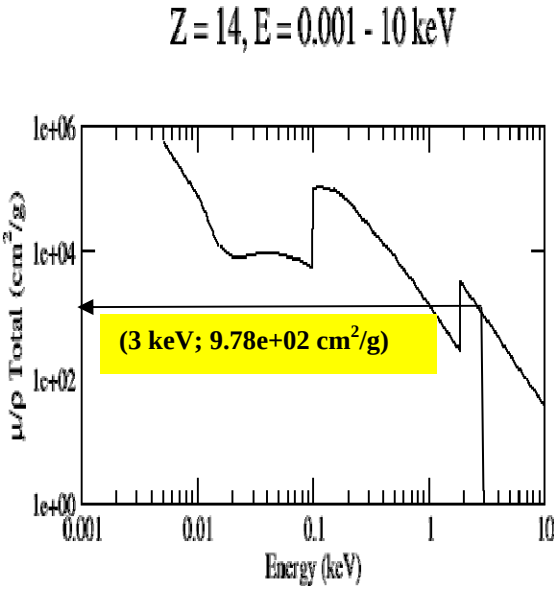

Figure 2-20: Mass attenuation coefficients of silicon at different x-ray energies.

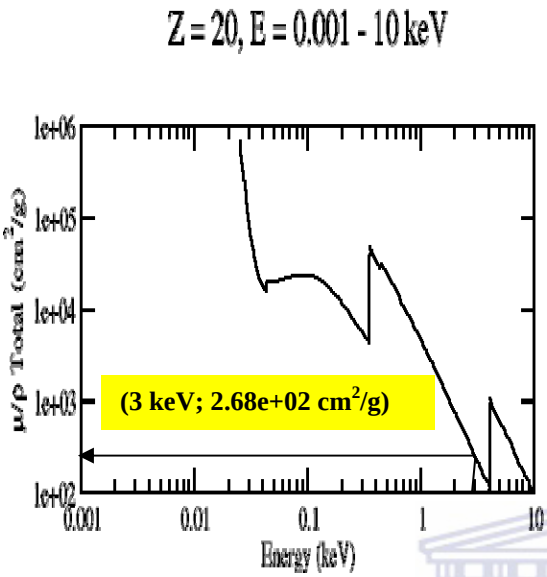

Figure 2-21: Mass attenuation coefficients of calcium at different x-ray energies.

There is good possibilities to detect chlorides at 3.0 keV x-ray energy but practically impossible to achieve penetration of x-rays through relatively thick concrete samples at this low energy. As a result, x-ray radiography and tomography will not be used for the investigations required by this study.

2.6.2 Thermal Neutron attenuation coefficients

Table 2.2 indicates that thermal neutrons are attenuated (mass absorption coefficient) the most by water, chlorine, iron, sodium, concrete, silicon and calcium, in decreasing order [Bay92]. This means that water has the dominant influence over the contrast of neutron radiograms, which makes the imaging of the presence of chlorides within the wet laboratory concrete samples impossible. The absence of water implies that chlorides presence within dry laboratory concrete samples can be imaged.

Iron can also be imaged within dry laboratory concrete samples with neutrons, by virtue of the higher attenuation coefficient of iron than of the matrix of the concrete.

The mass absorption coefficient ($cm^2.g^{-1}$) of thermal neutrons for the elements, compounds and materials of interest for the study are shown in Table 2.2.

Table 2.2: Mass absorption coefficients for thermal neutrons of materials found in steel reinforced concrete [Bay92].

Material	**Mass absorption coefficient ($cm^2.g^{-1}$)**
Water (H_2O)	3.48
Chlorine (Cl)	0.85
Iron (Fe)	0.15
Concrete	0.06
Silicon (Si)	0.04
Calcium (Ca)	0.04
Sodium (Na)	0.12

Based on the good penetration nature of neutrons and differences in neutrons attenuation by concrete, iron and chlorides, neutron-based techniques show good potential for the detection of (a) chlorides within dry laboratory concrete samples and (b) imaging of steel within dry laboratory concrete samples.

Chapter 3: Experimental set-up and Methodology

In this chapter, the experimental work performed for this study are described namely: The radiation sources and collimation system at Necsa (section 3.1); the SANRAD (South African Neutron Radiography) facility (section 3.2); the laboratory control area on the beam port floor of the SAFARI-1 research reactor (section 3.3); the analytical methods applied (section 3.4); the sample referencing and conditioning (section 3.5) and sample preparation and measurement (section 3.6), are described.

3.1 Radiation sources and collimation system.

3.1.1 Neutron source (SAFARI-1 nuclear research reactor)

Neutron radiographs and tomograms for this study were produced with the use of a neutron beam from the SAFARI-1 nuclear research reactor (Figure 3-1) operated by Necsa. Necsa is located at Pelindaba, Northwest Province of South Africa which is 30 km west of Pretoria. Neutrons are produced in the reactor core through controlled fission of enriched ^{235}U nuclear fuel into two smaller nuclei, energy and fragments amongst which are free neutrons.

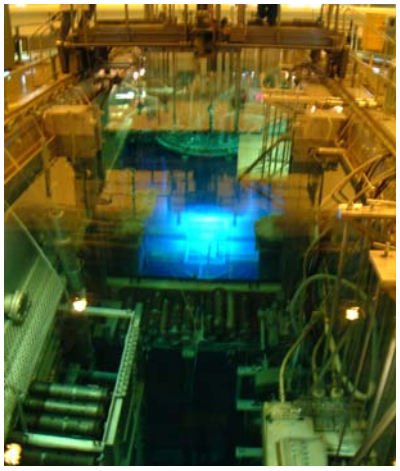

Figure 3-1: Photograph of SAFARI-1 nuclear research reactor interior view.

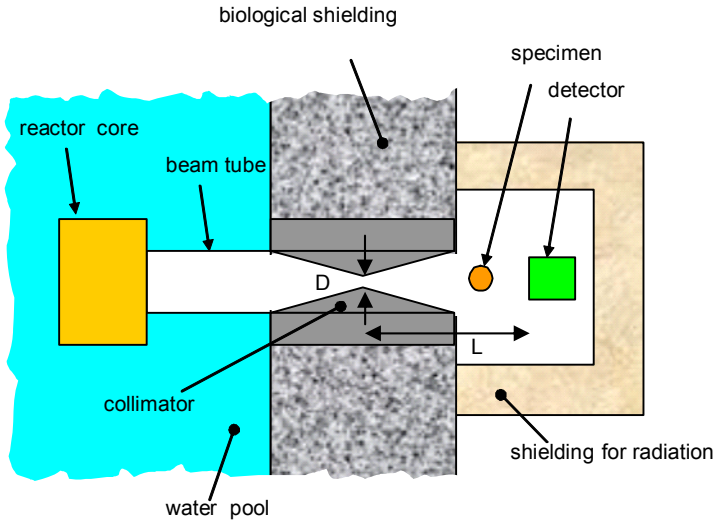

Figure 3-2: Schematic top view representation of a neutron radiography facility.

Figure 3-2 is a schematic representation of a neutron radiography facility. The fast neutron beam eminating from the fission is moderated into thermal neutrons by the water surrounding the reactor core. From the reactor core, a beam tube directs the neutron beam through a collimation (beam shaping) system to the radiography experimental facility on the beam port floor of the reactor.

3.1.2 The Neutron beam collimation system

The arrangement of key components of the neutron radiography set-up involved in the production, collimation and the application of the neutron beam is shown in Figure 3-2. Neutrons produced in the reactor core are expelled radially. Those neutrons that fall within the solid angle of the beam tube are channeled through the collimation system. The collimation system consists of a laminated structure built up from sections of Fe (Iron) and PE (Polyethylene). The function of the collimator is to attenuate the fast neutrons. A bismuth crystal located in the beam path is used to eliminate most of the gamma rays eminating from the fission reaction as well as the prompt gamma rays produced from the scattered neutrons. This renders the neutron beam to be 93% thermal. Specifications and the characteristics of the neutron beam and those of the collimation system are summarized in Table 3.1. At 20 MW reactor power and using a 21 mm interior pinhole diameter neutron passage in the collimator, a flux of 1.2 x 10^7 n.cm^{-2}.s^{-1} is delivered at the object position in the centre of beam. There are two beam shutters, the exterior and interior (pinholes).

Table 3.1: Specifications and the characteristics of the neutron beam and collimation system.

Distance (L) from aperture to the detection plane	3000 mm
Beam diameter at outlet of collimator	300 mm
Neutron flux at object in centre of beam (n.cm^{-2}.s^{-1}) at 20 MW reactor power & pinhole (D) = 21 mm	1.2×10^7
Separate pinhole apertures: D = 6 mm D = 10 mm D = 21 mm	Collimation ratio L/D 500 300 143
Beam divergence at: D = 6 mm D = 10 mm D = 21 mm	0.9^0 1.5^0 3.2^0

The exterior beam shutter, serves as the main beam shutter, has a 300 mm diameter and the interior has three diameters of 6, 10 and 21 mm to choose from, depending on the required beam flux and diameter.

3.1.3 X-ray source

A 100 kV x-ray tube, can be installed at the exit of the collimator to replace the neutron beam delivery with x-rays. The power supply and the control panel are located in the laboratory control area, outside the facility's containment. A change in voltage and electrical current affects the image produced on the frame grabber computer. The control panel and the detection system for x-rays are discussed in sections 3.2.3.1 and 3.3.2. Characteristics of the x-ray beam and the imaging properties are summarised in Table 3-2 [Bee05].

Table 3.2: Specifications and character of the x-ray beam.

Distance (L) for the aperture to the detection system	800 mm
Cone beam diameter at scintillator	728 mm
Focal spot D: D = 1 mm D = 3 mm	Collimation ratio L/D: 800 266
X-ray tube voltage range	0-100 kV
Beam divergence	40^{o} at D = 3 mm.

3.2 SANRAD (South African Neutron Radiography) facility

The SANRAD facility is situated at beam port No. 2 of the SAFARI-1 reactor in the beam port hall. The facility has neighboring facilities, i.e. a small angle neutron scattering facility (beam port No. 1) and a neutron diffraction facility (beam port No.5).

The SANRAD facility consists of a radiation containment component and an experimental control area. The containment is where a sample is exposed to neutron or x-ray radiation and shields the surrounding area from penetrating

neutron and x-ray radiation beams. The imaging system for radiography is located inside the containment. An experimental control area is where stage rotations and image acquisition are controlled. This is also where pinhole size is selected and shutter is opened and closed. There are two Pentium-4 computers in place to assist with operations including image manipulation, data acquisition and reconstruction of 3-D images.

The experimental set-up shown in Figure 2-9 gives a representation of the experimental apparatus. Arrows show the progression of the beam from the external shutter, to the sample where it is generally partly attenuated and partly transmitted, then to the detection system and finally to the computer based output system.

3.2.1 Experimental set-up containment

The containment shown in Figure 3-3 serves as an enclosed radiological shielding with (200 x 200 x 200) cm^3 internal dimensions. The reactor core concrete structure forms one of the vertical sides, while the other three (including the roof) consists of 45 cm thick high density concrete covered on the inside with layers of 2 cm thick wax tiles containing 5% boron by mass, covered by 2 cm thick polyethylene sheet. Part of the concrete roofing directly above the sample area is removable to accommodate samples longer than 200 cm. The outer area of the side walls of the containment is covered with 5 cm lead (Pb), for shielding against secondary gamma rays emerging from neutron interaction with the sample and concrete shielding. The side of the containment opposite to beam entry is used as the entrance and beam stop. It is a 150 cm thick sandwich like structure of 0.5 cm steel layer housing filled with concrete and PE layers. It is driven backwards and forwards by a motor. The front surface of the beam stop is covered with a 4 cm layer of wax containing 5% boron by mass. Boron incorporation is important for its neutron absorption effect as can be seen in Figure 2-6.

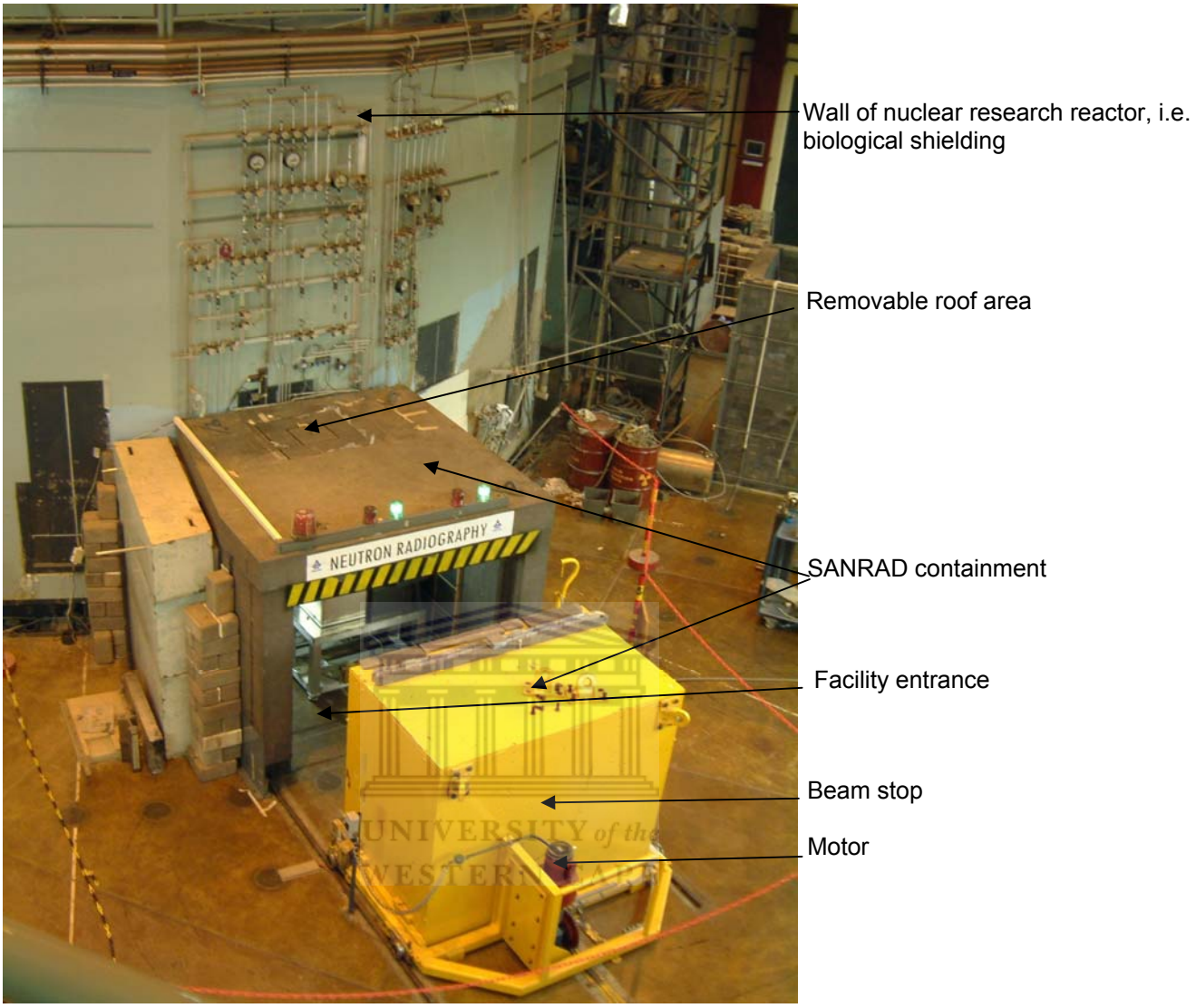

Figure 3-3: SANRAD facility containment.

3.2.2 The camera system for neutron and x-ray detection

The detection system used in this study is a camera system consisting of a light-tight hollow box made of aluminum , a neutron scintillator screen, an aluminum-coated mirror and a lens mounted onto a CCD (charge coupled device) camera as indicated on Figures 3.4 and 3.5. Shown in Figure 3-4 is the upper section (red) of the light-tight box that houses the camera system. It is critical for the box to be light-tight for preservation of the visible light image

formed by the scintillator screen after interaction with radiation suitable to be captured by the scintillator screen. The light-tight box is lined on the inside with aluminum, lead and boron carbide for shielding which aides the quality of the radiograph. Aluminum has a very short neutron half life which is critical for safety within the experimental facility. Image detection takes place when the radiation beam (neutrons/x-rays) incident on the scintillator screen is converted to visible radiation (light), that is reflected by the mirror to the CCD camera lens and magnified onto the CCD camera chip, and captured by the frame grabber card in the PC. Image detection is detailed in section 2.4.2.2.

Figure 3-4: Photograph showing the upper part of the light-tight box. This houses the camera system on the top of the red component of the box.

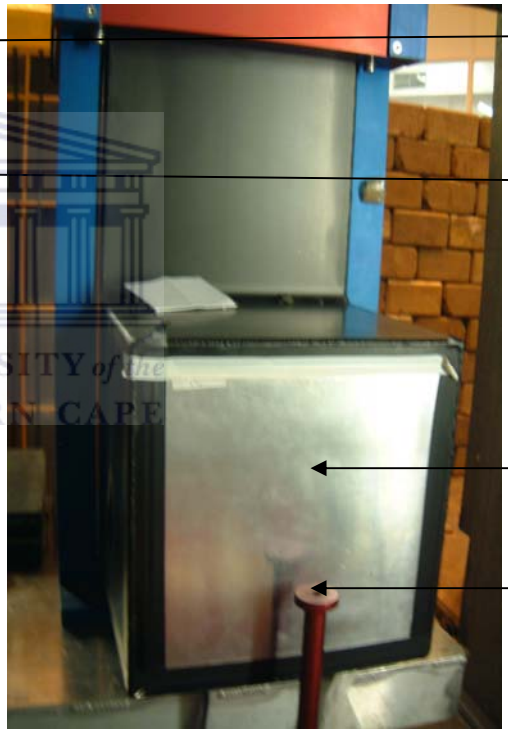

Figure 3-5: Photograph showing the view of the imaging equipment as viewed along the beam direction.

3.2.2.1 Scintillator screens

The scintillator screen is responsible for the conversion of the incident x-rays or neutron beam into visible light radiation for the production of photo

images (radiographs). The appropriate scintillator screen is matched to the type of radiation. For neutrons the scintillator used is (^{6}LiF/ZnS: Cu, Al, Au) and for x-rays it is gadolinium oxysulfide, Gd_2O_2S, [htt23]. The scintillator screen is mounted on the light-tight box with the incident radiation beam perpendicular to its surface, as shown in Figure 3-6. Neutron imaging is made possible through an appropriate scintillator screen, by having neutrons incident on the scintillator screen interacting with the lithium ions from ^{6}LiF to produce alpha particles, tritons and 4.8 MeV photons as interaction products. The alpha and triton particles interact with ZnS:Ag and radiate visible light that is pixed up by the CCD camera. In the case of the x-ray scintillator screen, the x-rays interact with the gadolinium oxysulfide that produces visible light from excitation and de-excitation of the semiconductor material.

3.2.2.2 Aluminum front-coated mirror

A front surface coated mirror mounted at 45^{o} vertical to the incident beam reflects the photon image from the scintillator screen to the lens on the CCD camera. The mirror reflects the photo image from the scintillator screen towards CCD camera in the set-up that seeks to protect the CCD camera from being directly exposed to incident radiation.

3.2.2.3 SMC-Pentax lenses

These lenses are employed for magnifying the photon image from the scintillator screen in order to improve the image spatial resolution, especially for small samples. Lenses vary resolution of the image and vary the field of view on the scintillator screen. Table 3.3 presents the spatial resolution obtained with various SMC-Pentax lenses.

Table 3.3 : Specifications of various SMC-Pentax lenses, [Bee05].

Pentax lens Type	Field of view (FOV[c]) (mm^2)	Spatial Resolution[d] (pixels/mm)
A 50mm/F1.2	250 x 250	3.8
FA 100 mm/F2.8	130x 130	7.7
FA 135 mm/F2.8	100x 100	10.3

c. An area that is focused by a camera lens on the scintillator screen.
d. Ability to distinguish between two closely spaced objects.

In this study the FA 135 mm/F2.8 pentax lens is used for the capturing of radiographs.

3.2.2.4 Peltier-cooled CCD camera

Images are captured by a Peltier-cooled CCD camera. Its specification is an Andor type with 1024×1024 pixel array and 16-bit image output device at $2\,\mu s / pixel$. The Peltier-cooled CCD camera has an image acquisition rate of 1.2 s but can be adjusted to produce a radiograph at full dynamic range[e]. It captures photo images reflected from the scintillator screen through the Pentax lens. Because these images are created by means of radioactivity, they are being called radiographs. The camera chip can be cooled to -75^{o}C to minimize dark current[f] to less than 0.05 electrons/pixels. Dark current incorporates gray value errors due to contribution of electrons from the electronics into electron wells for gray value determination. For the purpose of the study, it was sufficient to cool to -45^{o}C.

3.2.3 Rotary table

The translation table, shown in Figure 3-6, is used for the horizontal rotation of the sample to enable taking images, at different angles, with the imaging system for different projections that are used for 3-D tomographic reconstructions. The platform on which the sample is put is available in different sizes to accommodate different sized objects. The movement is available in 4 directions i.e. X-sideways, Y-backwards and forwards, Z-upwards and downwards, and R-horizontal rotations relative to the scintillator screen. A stepper motor controls the horizontal rotation of the sample to enable acquisition of radiographs at sample rotations between 0^{o} to 360^{o}, and the X-translation across the detector is for the positioning of the sample within the field of view. Y and Z-translations are being performed manually to position the sample at the appropriate distance and horizontal level in front of the detector.

---

e. It's a scale range that defines the lower as well as the upper limits of number of electrons that can be accommodated in the electron well in the CCD chip.

f. Electrons produced from electronics as a result of relatively warm temperatures.

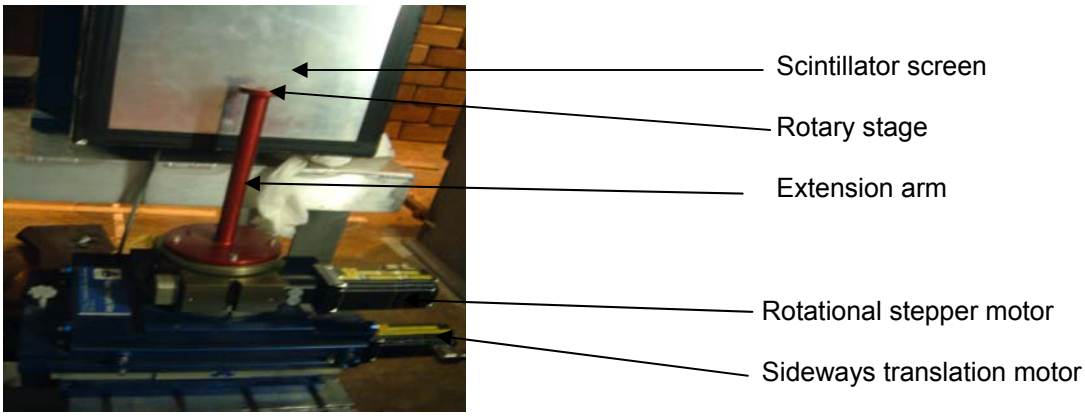

Figure 3-6: Photograph of the rotary table in front of the scintillator screen.

3.3 Experimental control area

3.3.1 Control Box

The experimental hutch control box (Figure 3-7) is situated in the experimental control area. From here the radiation type and status of the neutron beam main shutter and the pinhole size (D = 6, 10 or 21 mm diameters) are controlled.

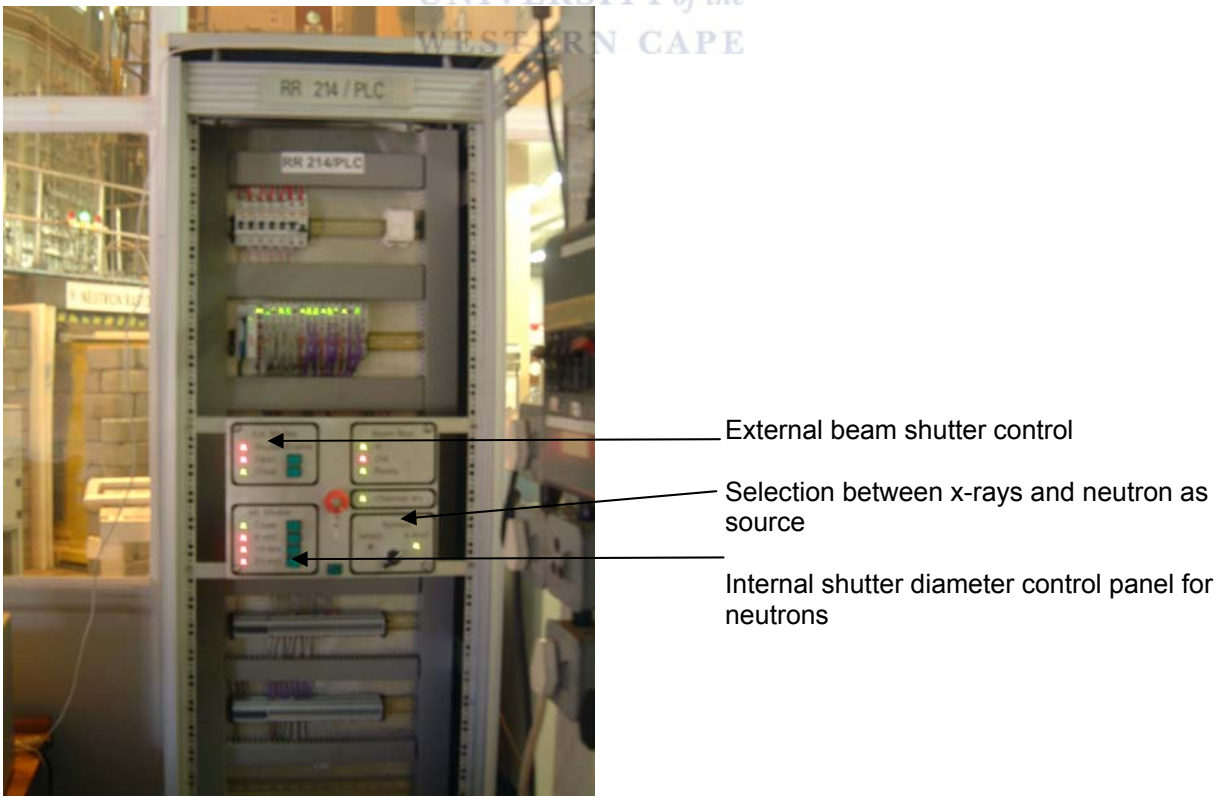

Figure 3-7: Control box for the SANRAD facility.

3.3.2 Computers and the x-ray control panel

The image from the CCD camera within the containment is transferred to the data acquisition computer with a frame grabber card in a PC located in the experimental control area. There are three Pentium-4 computers (Figure 3-8) in the experimental control area, one for image acquisition and manipulation, and the other to control the sample movement such as rotational speed and rotation steps. The third computer contains several software packages for tomography re-construction, enhancement, visualization and analysis.

The x-ray energy and current settings are operated through a separate control panel shown in Figure 3-8.

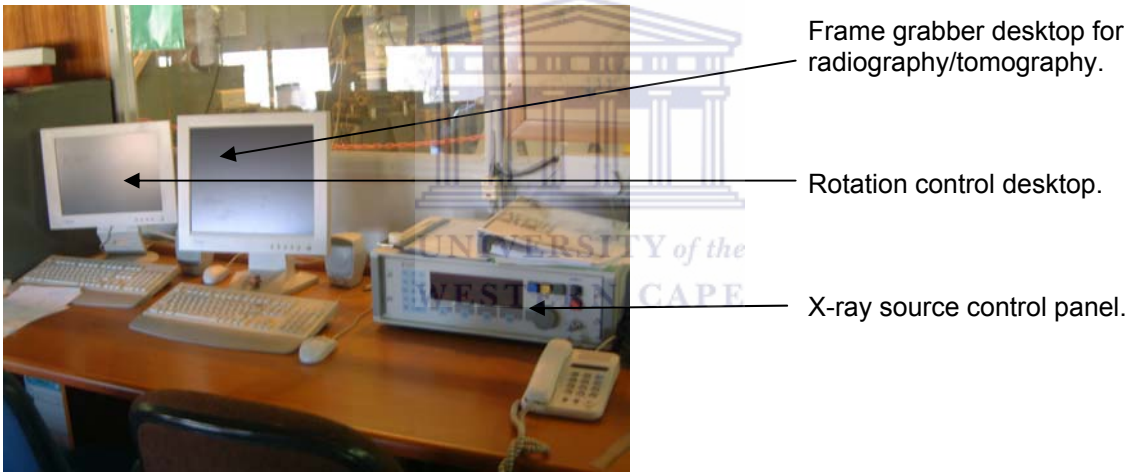

Figure 3-8: Frame grabber and rotation controlling desktops for neutron and x-rays radiography; as well as the control panel for the x-ray source.

3.4 Methods for the analysis of results

This section discusses the methodology used to acquire results for the investigation of chloride effects within laboratory concrete samples (section 3.4.1), porosity change through the leaching of concrete samples (section 3.4.2) and the preliminary detection of the effect of chlorides dissolved in distilled water (section 3.4.3). Porosity change is obtained from the difference between two calculated percentage porosity values from the same sample, validated by gravimetrical method, each after a certain length of exposure to conditions that are capable of leaching out concrete's cement paste. The chlorides within the laboratory concrete sample influence the corrosion of the steel element embedded in concrete. The preliminary investigation detects the effects of chlorides dissolved in distilled water on the attenuation of penetrating radiation by absorbed NaCl solutions of different concentrations.

3.4.1 Corrosion Analysis by 3-D imaging

The effects of oxides and hydroxides to corrode steel within the concrete samples, which is influenced by the presence of chlorides, can be visualized and quantified through neutron tomography. Neutrons were chosen as a source of radiation over x-rays notwithstanding the fact that x-rays have a bigger attenuation difference between concrete and iron, but neutrons has better penetration capability through concrete. Shown on Table 3.4 are the mass absorption coefficient values of 30 keV x-rays and thermal neutrons by concrete and iron.

Table 3.4: Mass absorption coefficients of 30 keV x-rays and thermal neutrons for concrete and iron.

	Thermal neutron mass absorption coefficient. ($cm^2.g^{-1}$)	**30 keV x-rays mass absorption coefficient ($cm^2.g^{-1}$)**
Concrete	0.06	0.96
Iron	0.15	8.20

Corrosion analysis involves image acquisition, image enhancement and calculations. The study in this regard was conducted based on the capabilities of neutron radiography and tomography. Radiograph acquisition and re-construction into 3–D tomogram images were performed with the Octopus(V8) software package [htt20]. Tomographs were enhanced and analyzed using VGStudioMax software package [htt21] whose capabilities are discussed in sections 3.4.1.1 and 3.4.1.2. Enhancement, analysis and data acquisition of radiographs made possible through IPPLUS image enhancement software package; there after data was organized and presented on Excel.

3.4.1.1 3-D Image acquisition

Radiographs were acquired (using a PC with frame grabber capabilities) after 1^0 step of the 180^0 rotation angle of the sample on a rotary stage. The software package used to control rotations also provides the user capabilities to set the angle of the sample's rotation, and the number of rotation steps to constitute the angle of rotation. In this study the sample was rotated from 0^0 to 180^0 in steps of 1^0; 225 steps of 0.8^0 was also possible.

Figures 3-9 to 3-12 show the collected radiographs of concrete sample-1_{before} containing thin Fe rods (darker lines) taken at rotation angels 0^0, 45^0, 90^0 and 180^0. A 3-D re-constructed tomogram is shown in Figure 3-13.

Figure 3-9:
Neutron radiograph of the Ferro concrete sample at 0^0 (starting position).

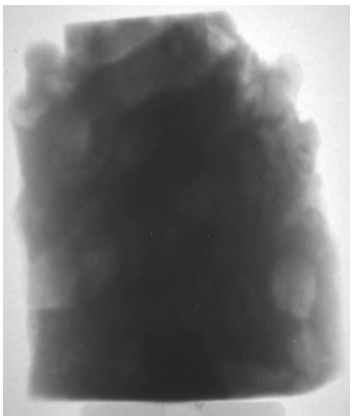

Figure 3-10:
Neutron radiograph of the Ferro concrete sample rotated 45^0.

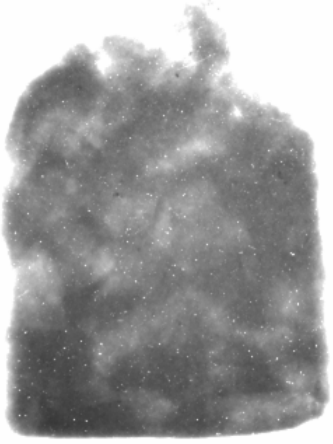

Figure 3-11:
Neutron radiograph of the Ferro concrete sample rotated 90^0.

Figure 3-12:
Neutron radiograph of the Ferro concrete sample rotated 180^0.

3.4.1.2 Image analysis and data acquisition

VGstudioMax software package is capable to visualize and analyze a reconstructed tomogram of the sample in 3-D. This software package was used for the analysis of the Ferro corrosion in this study.

VGStudioMax visualization software package

The VGStudioMax software package allows for the assignment of different colours to different components (Pseudo coloring) present as for example in the complete Ferro concrete sample shown in Figure 3-13. The package furthermore allows the user to view inside the sample through software cutting in X, Y, or Z direction through the sample mass as shown in the representation of Figure 3-14.

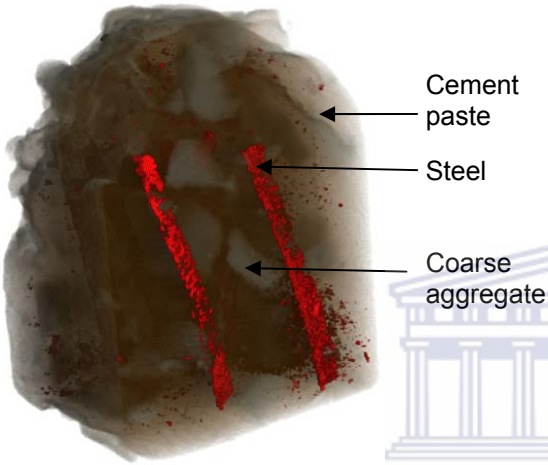

Figure 3-13: Neutron tomogram of a complete Ferro concrete sample -2 showing cement paste, aggregates and steel bars within the concrete sample.

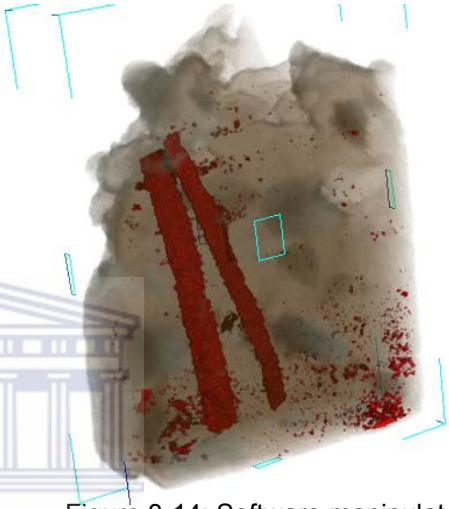

Figure 3-14: Software manipulated image of the Ferro concrete sample-2 revealing steel bars within the sample after 'cutting' using VGStudio(Max).

Figure 3-15: Software manipulated image of Ferro concrete sample-2 to only show the steel rods within the concrete.

Figure 3-16: Software manipulated image of Ferro concrete sample-2 to only show aggregates embedded in cement paste within the concrete.

This software package allows also for preferential viewing of specific sample components based on the different degrees of attenuation of the radiation beam through the different constituents of the sample. The software thus enables selective viewing between cement paste, coarse aggregates, the steel reinforcement and / or water (Figure 3-15), as well as viewing only the coarse aggregates of the concrete sample (Figure 3-16).

Procedure for quantification of steel volume within concrete samples

The mass extraction functionality in VGStudio software package was employed for the quantitative estimation of the steel volume embedded within the concrete, on the reconstructed tomogram. This functionality involves the following steps:

- Image filtering
- Dynamic range selection
- Selection of element of interest
- Extraction of element of interest

The first step is to enhance the tomogram resolution using image filters. Selection of sensitivity for volume estimation of the constituent to be extracted is achieved through dynamic range settings. Estimation of the constituent of interest, with respect to its pixel intensity value range, then follows. When the estimation is completed, the extraction of the constituent of interest is possible. The extraction functionality is not only capable of showing the extracted constituent of interest and the solid mass from which it is extracted, it is also capable to quantitatively estimate the volume of the constituent of interest as shown in Figure 3-17.

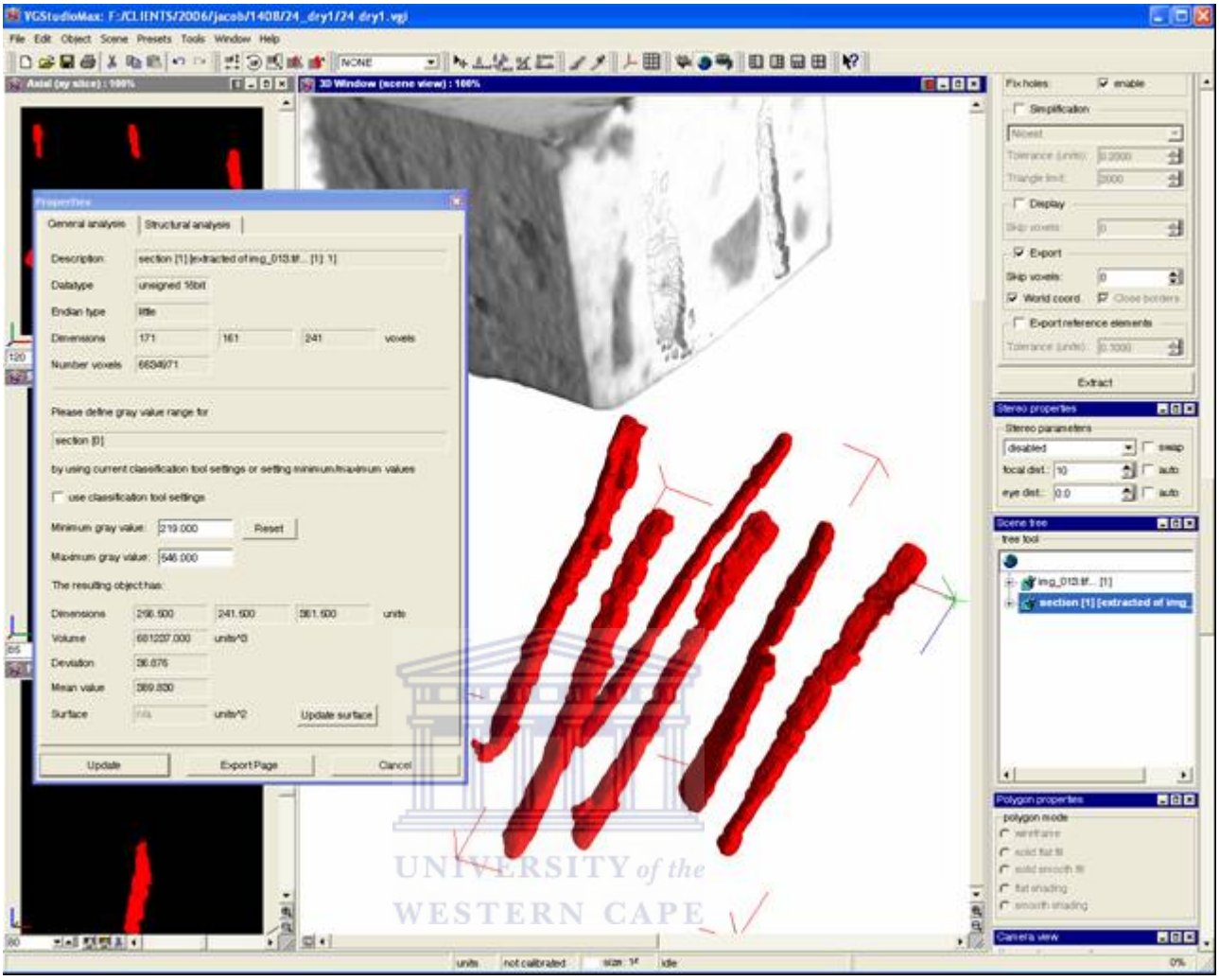

Figure 3-17: Demonstration of the volume extraction and quantification functionalities of VGStudio software package.

3.4.2 Percentage Porosity Analysis

3.4.2.1 NRad percentage porosity determination

Formula derivation

Porosity calculation from neutron transmission radiographs offers the capability of obtaining porosity percentage value as a function of pixel scale at any place within the sample or the sample bulk. This advantage provides for great sensitivity to detect the distribution of pores within the sample.

From an acquired radiograph, the pixel intensity values along a line profile are obtained utilizing IPPLUS 2-D image enhancement and analysis software by placing a line profile vertically or horizontally across the image. Shown in Figure 3-18 are pixel grey scale values obtained from a vertical line profile on a concrete sample. The grey scale value is linearly dependant on the attenuation of the beam through the sample. A black area on the radiograph, which indicates high degree of neutron /x-ray absorption, has a low pixel intensity value and vice versa.

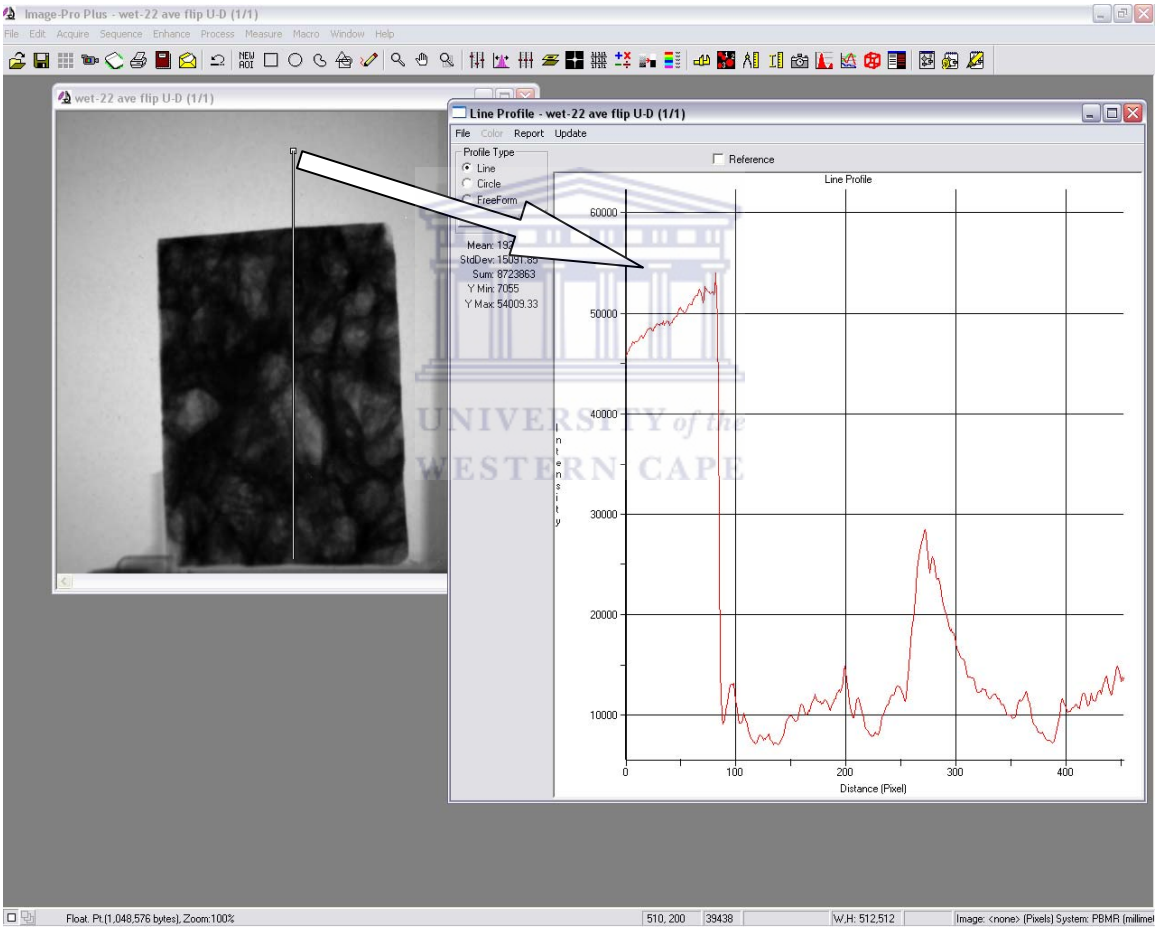

Figure 3-18: Demonstration of pixel values along a thin vertical line profile across the sample.

The bulk porosity percentage of the sample is achieved by the difference in average pixel intensity values between the sample in dry state and water saturated state. The mean pixel intensity values across the sample are obtained

from placing a “thick” line profile vertical or horizontal over the sample. This line profile must cover most of the height or width of the image. This is shown later in Figure 3-25.

The radiation attenuation relation of the area of the dry porous sample material without pores is given by the equation:

$$I_{massive.dry} = I_0 e^{-(\Sigma_m x)} \qquad \text{(Eq 3-1)}$$

where, $\Sigma_m = \mu_m \rho_m$

Σ_m - macroscopic cross section of the atoms of the porous sample’s solid matrix, in a cm^3 of the sample’s solid matrix.(cm^{-1})

μ_m - mass absorption coefficient of the sample’s atoms of the solid matrix. ($cm^2.g^{-1}$)

ρ_m - density of the material of sample. ($g.cm^{-3}$)

x - thickness of the material of sample. (cm)

I_0 - pixel intensity value of the incident neutron beam without attenuation by the sample.

$I_{massive.dry}$ - pixel intensity value of the beam transmitted through the sample.

The attenuation relation of the dry porous sample’s area with a void (pore) is given by:

$$I_{pore.dry} = I_0 e^{-(\Sigma_m (x - \Phi x) + \Sigma_a \Phi x)} \qquad \text{(Eq 3-2)}$$

where,

Σ_a - the macroscopic cross section of the atoms of the air in the pore space, in a cm^3 of air. (cm^{-1})

Φ - the ratio of the length of the pore area to the total length of the solid matrix and pore area of the porous sample.

$I_{pore.dry}$ - pixel intensity value of the transmitted beam through the area of a dry porous sample with pore(s).

The attenuation of the air is insignificant and can be neglected, so the equation may be written as:

$$I_{pore.dry} = I_0 e^{(-\sum_m (x - \Phi x))} \qquad \text{(Eq 3-3)}$$

When the void is filled with a liquid, the relation becomes:

$$I_{pore.sat.} = I_0 e^{-(\sum_m (x - \Phi x) + \sum_l \Phi x)} \qquad \text{(Eq 3-4)}$$

where,

Σ_l - the macroscopic cross section of the atoms of the liquid in the pore space, in a cm^3 of liquid. (cm^{-1})

But equation 3-4 may be expressed as:

$$I_{pore.sat.} = I_0 e^{-\sum_m (x - \Phi x)} e^{(-\Sigma_l \Phi x)} \qquad \text{(Eq 3-5)}$$

Substituting equation 3-3 in 3-5 gives:

$$I_{pore.sat.} = I_{pore.dry} e^{(-\Sigma_l \Phi x)}$$

$$\ln\left(\frac{I_{pore.dry}}{I_{pore.sat.}}\right) = \sum_l \Phi x$$

$$\therefore \Phi = \frac{\left(\ln\left(\frac{I_{pore.dry}}{I_{pore.sat.}}\right)\right)}{(\Sigma_l x)} \qquad \text{(Eq 3-6)}$$

To calculate the bulk percentage porosity entails (a) determination of $I_{pore.dry}$ and $I_{pore.sat.}$ as mean pixel intensity value for a thick line profile at the same position on the dry and wet sample. For pixel percentage porosity calculation (Porosity distribution), $I_{pore.dry}$ or $I_{pore.sat.}$ is considered to be a pixel intensity value from a thin line profile. Essential parameters are the neutron attenuation factor of the liquid filling the pores and the thickness of the porous sample.

Percentage porosity values in laboratory concrete samples of this study were calculated using the equation 3-6.

(a) Determination of I_{dry} and $I_{sat.}$

Radiographs of a sample in a dry and wet state were respectively acquired to obtain $I_{sat.}$ and $I_{dry.}$ The images were normalized and thick line profiles analysis done over the samples cross sectional areas. The mean and standard deviation for $I_{sat.}$ and I_{dry} were used in our bulk percentage porosity calculations. This is shown later in Figures 3-25 and 3-26.

Normalization of* I_{dry} and I_{sat} *sample images

Radiographs had to be normalized because the neutron fluxes from the reactor are not constant and the radiography process is a statistical process. Figures 3-19 to 3-23 demonstrate 2 steps involved in the radiograph normalizing procedure. Two regions of the radiograph respectively outside the sample region and far from the sample region, and far from the sample region, were chosen from each of the radiographs to be normalized. As the first normalization step, regions of interest defined by a thick line profile were placed outside the images from concrete samples in both the wet and dry state as demonstrated in Figures 3-19 and 3-20. The average and standard deviation of the pixel values over the line lengths were used to determine the normalization factor, by dividing the greater average by the smaller average from the two images. The acquisition of

average and standard deviation from the images of the sample in the dry and wet states is shown in Figures 3-21 to 3-22. This normalization factor was used to normalize radiographs through IPPLUS functionality as shown in Figure 3-23. This IPPLUS functionality can increase or decrease pixel intensities of all pixels of the radiograph according to this factor. This is the second step of radiograph normalization procedure. It can be seen that after normalization procedure the average from the two images of the sample in the dry and wet states, within normalizing regions, are equal. The average of the image of the sample in a dry state was 39077.10 before normalization and 41390.26 after normalization.

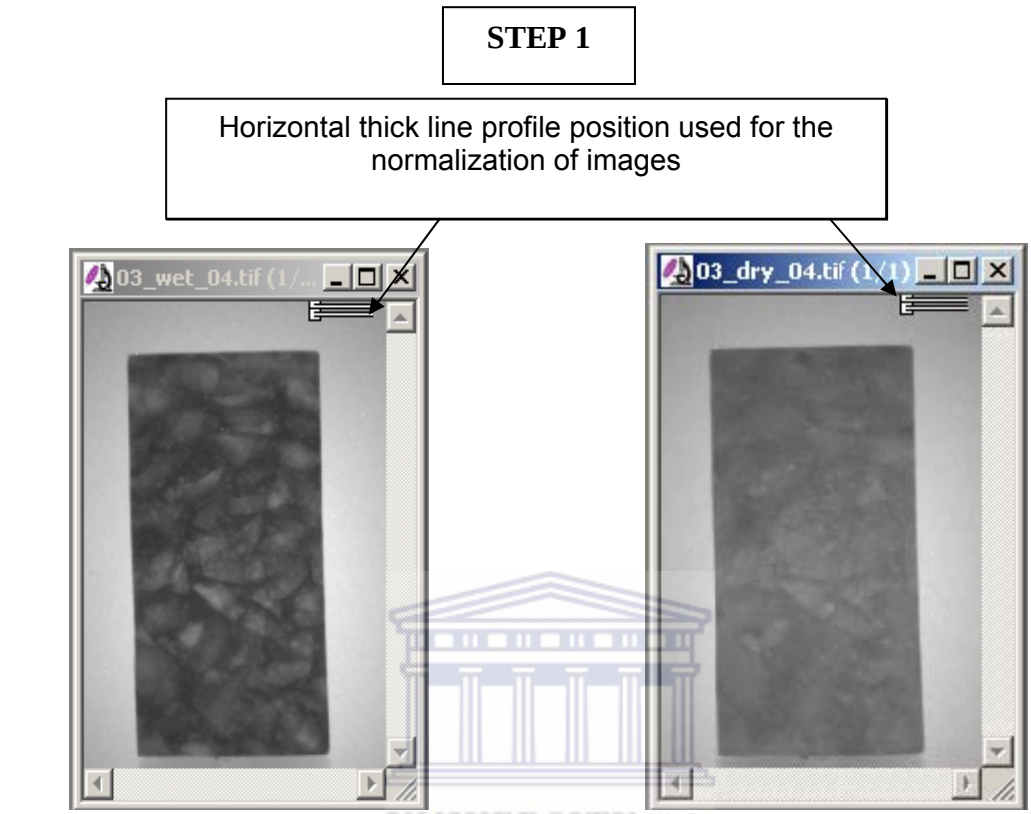

Figure 3-19: NRad image of a water saturated sample.

Figure 3-20: NRad image of a dry sample.

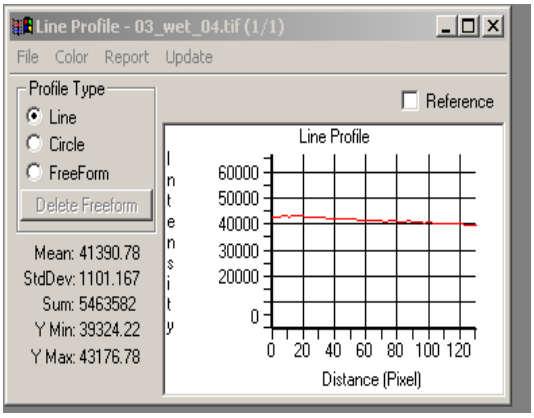

Figure 3-21: Radiograph normalization procedure: a pixel intensity vs distance plot of the line profile of a water saturated sample.

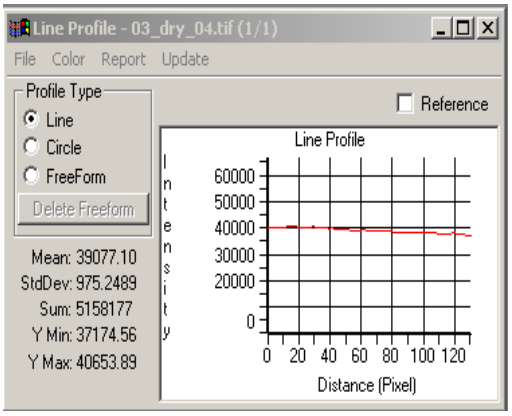

Figure 3-22: Radiograph normalization procedure: a pixel intensity vs distance plot of a line profile of a dry sample.

STEP 2

Normalization factor = 1.059208

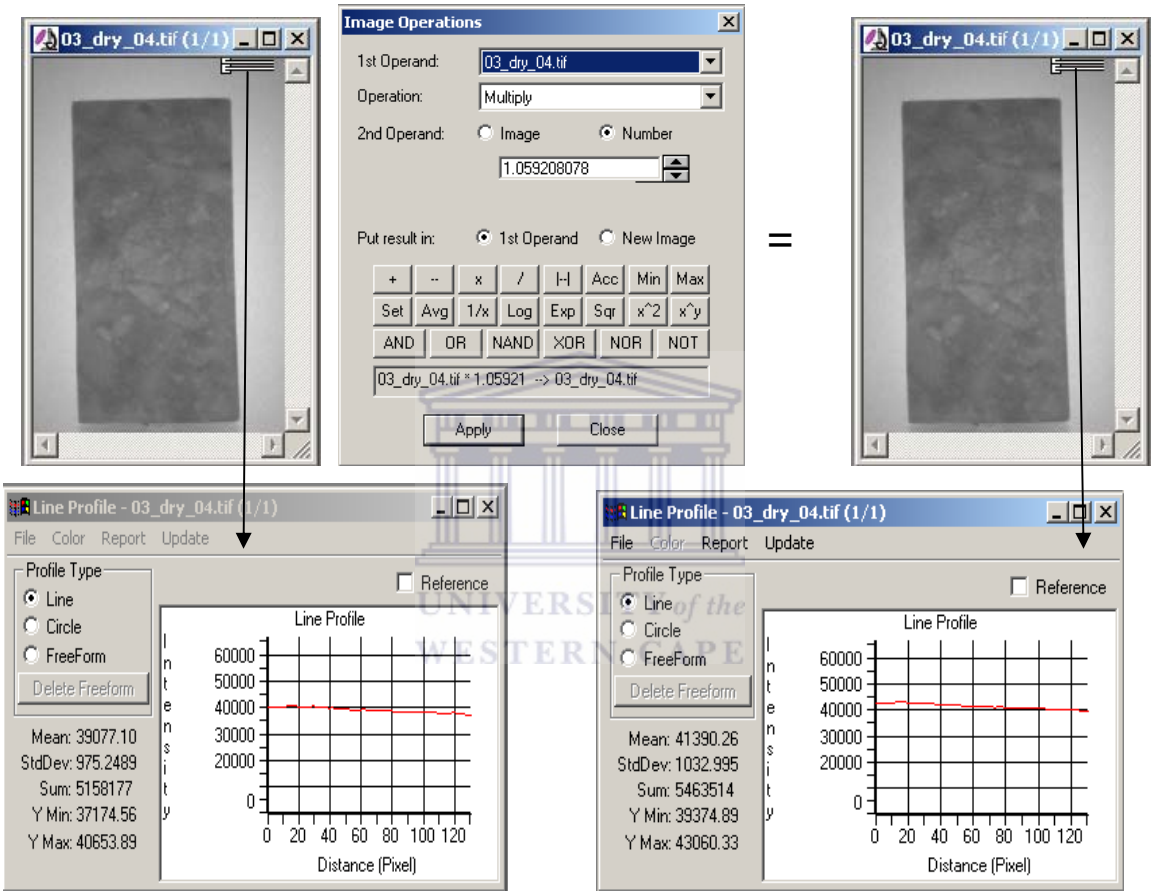

Figure 3-23: Demonstrating the increase in a radiograph's pixel intensity after normalization through IPPLUS software package.

Once the normalization of the radiographs is achieved, the pixel values are used as real quantitative data.

Acquisition of I_{dry} and I_{sat}

After the radiograph normalization procedure, thick line profiles were placed over the samples to obtain I_{dry} and I_{sat} as shown in Figure 3-24 and 3-25. Averages

from thick line profiles from the images of the sample in the dry and wet states defined I_{dry} and I_{sat}, and were 30028 and 19832.68 respectively.

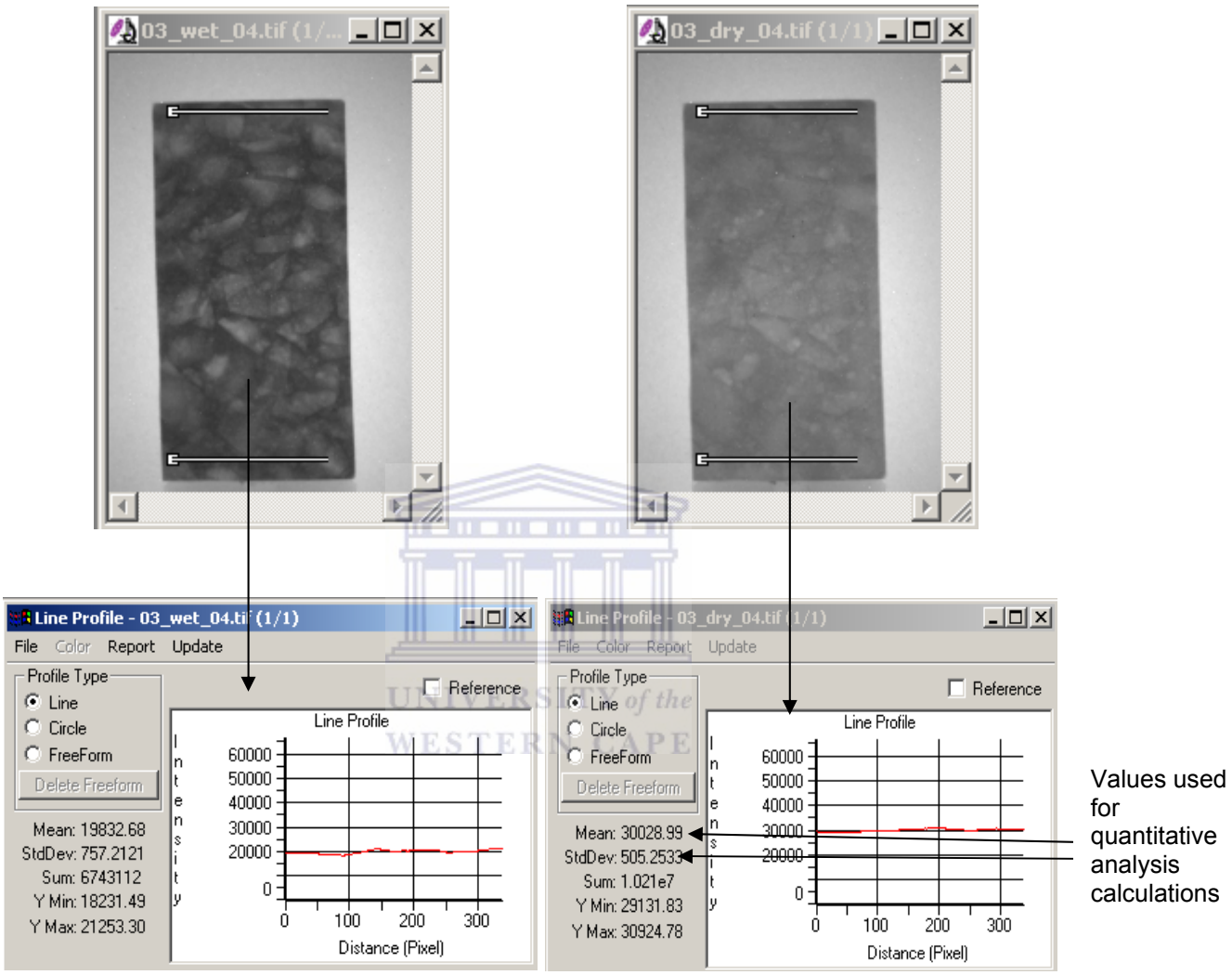

Figure 3-24: Mean and standard deviation of a thick line profile that serve as I_{sat} from a wet sample.

Figure 3-25: Mean and standard deviation of a thick line profile that serve as I_{dry} from a dry sample.

(b) Experimental determination of the linear attenuation coefficient of water

A photograph of the liquid sample holders (which can be filled with water) of equal cross-sectional area and different thicknesses is shown in Figure 3-26. In this study the 0.1, 0.3, 0.6 and 1.0 cm thick sample holders were used. Any other thicknesses can be used, these thicknesses were chosen because they were

already available. Radiographic images of water in each of these holders were individually obtained and are shown in Figures 3-32 to 3.35.

Figure 3-26: Aluminum sample holders of different thicknesses that can be filled with liquid.

From the radiation attenuation relation

$$I_{filledcontainer} = I_{emptycontainer} e^{-(\Sigma_m x)} \quad \text{(Eq 3-7)}$$

where,

$I_{filledcontainer}$ - mean pixel intensity of all pixels covering the cross-sectional area of a specific thickness sample holder filled with distilled water.

$I_{emptycontainer}$ - mean pixel intensity of all pixels covering the cross-sectional area of an empty sample holder.

this attenuation relation can be re-arranged to

$$\ln (I_{emptycontainer}/I_{filledcontainer}) = \Sigma_w \, x \quad \text{(Eq 3-8)}$$

which corresponds to a linear relationship between relevant parameters in the form:

$$y = mx + c \quad \text{(Eq 3-9)}$$

and ln ($I_{emptycontainer}/I_{filledcontainer}$) was plotted against water sample thickness, x, to obtain the attenuation factor from the slope of the graph shown in Figure 3-27. Since the plot due to multiple scattering of water has the form generally represented by an equation:

$$y = ax^2 + bx + c \qquad \text{(Eq 3-10)}$$

for which the slope is of the form

$$(dy/dx) = y' = 2ax + b \qquad \text{(Eq 3-11)}$$

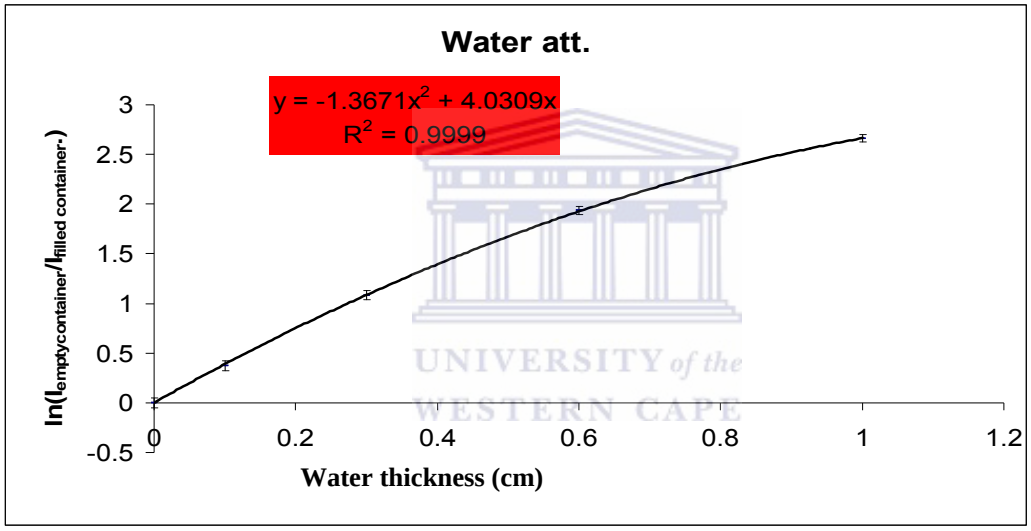

Figure-3-27: Plot of ln ($I_{emptycontainer}/I_{filledcontainer}$) = $\Sigma_w \; x$ defined using water thicknesses 0.1, 0.3, 0.6 and 1.0 cm.

Since the gradient, derivative of the function, is dependant on the thickness of water, x, corresponding x values for different ln($I_{empty\ container}/I_{filled\ container}$) values were calculated using the roots of the quadratic formula:

$$x = \frac{-b \pm \sqrt{b^2 - 4ac}}{2a} \qquad \text{(Eq 3-12)}$$

Two x-values were obtained for each y-value and one selected corresponding to the practical y-value obtained from x-values substitution into the

$\ln(I_{emptycontainer}/I_{filledcontainer})$ vs. x function, Eq 3-8. These x-values were substituted into the gradient formula to obtain the linear attenuation values for different water thicknesses.

Determination of $I_{emptycontainer}$ and $I_{filledcontainer}$

For each data point on the plot of Figure 3-27, an empty and water filled container of the same thickness, were respectively employed and imaged. These two radiographs were then normalized to one using the higher pixel intensity mean value; then $I_{emptycontainer}$ and $I_{filledcontainer}$ were obtained from horizontal thick line profiles placed on the sample holders cross-sectional areas containing water. Shown below are radiographs of the empty and distilled water filled sample holders as well as the horizontal thick line profile positions used (Figure 3-28 to 3-35).

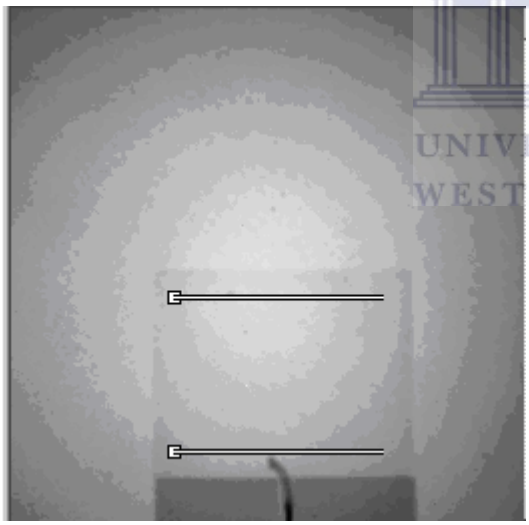

Figure 3-28: NRad image of the empty 0.1 cm thick sample holder and thick line profile position.

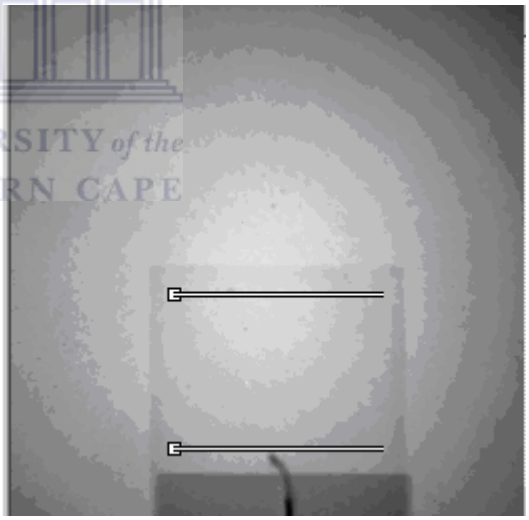

Figure 3-29: NRad image of the empty 0.3 cm thick sample holder and thick line profile position.

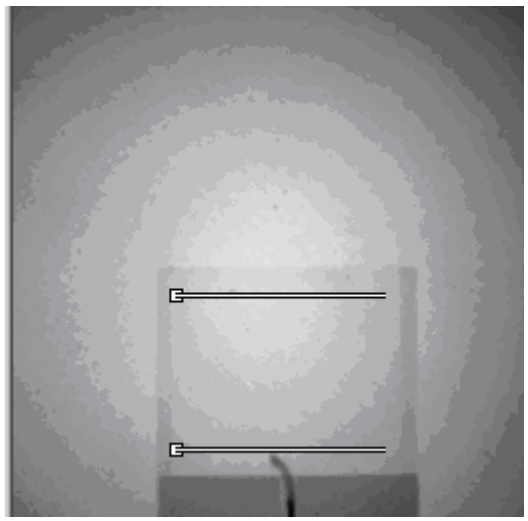

Figure 3-30: NRad image of the empty 0.6 cm thick sample holder and thick line profile position.

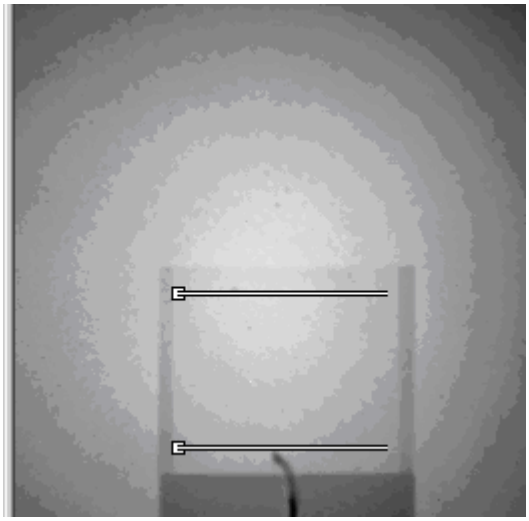

Figure 3-31: NRad image of the empty 1.0 cm thick sample holder and thick line profile position.

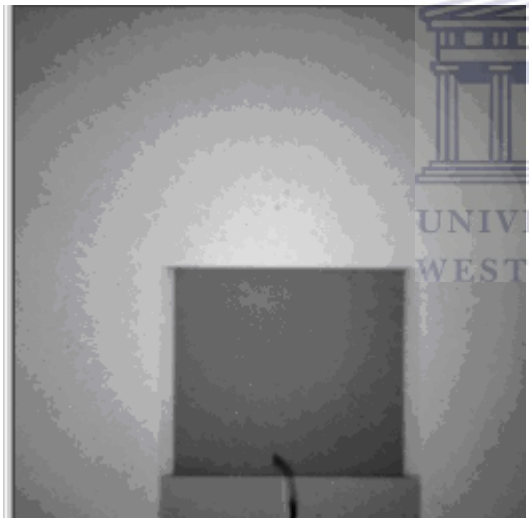

Figure 3-32: NRad image of the 0.1 cm thick sample holder position filled with distilled water.

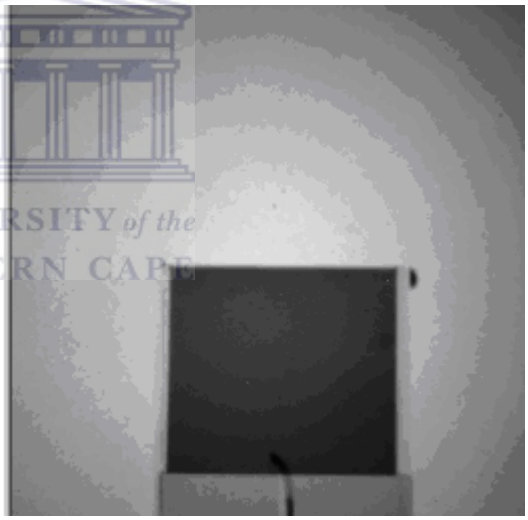

Figure 3-33: NRad image of the 0.3 cm thick sample holder position filled with distilled water.

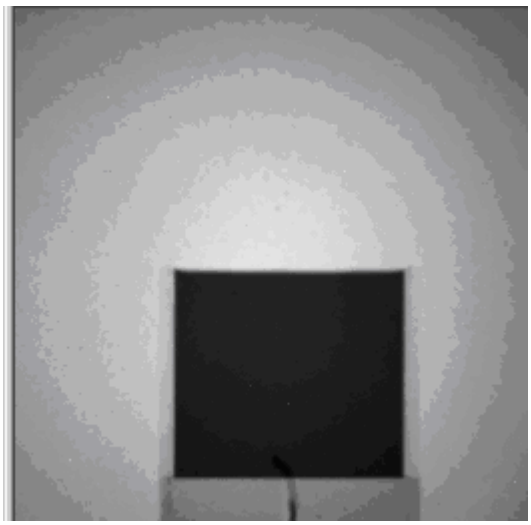

Figure 3-34: NRad image of the 0.6 cm thick sample holder position filled with distilled water.

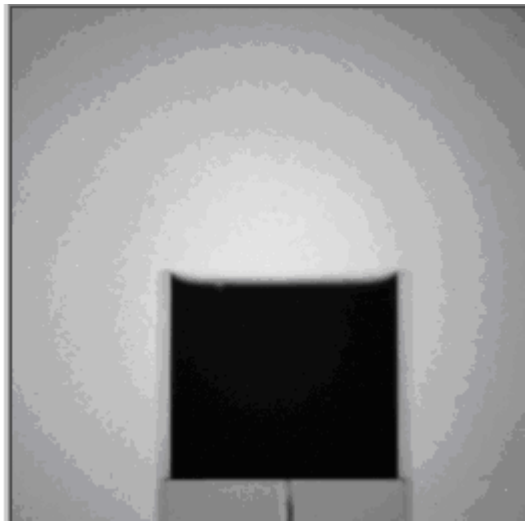

Figure 3-35: NRad image of the 1.0 cm thick sample holder position filled with distilled water.

(c) Error determination of the porosity [Gui89].

The error was also incorporated in the percentage porosity values. The percentage porosity is calculated using Eq 3-6.

If $I_{pore.dry}$, $I_{pore.sat.}$, Σ_l and x are experimentally determined values of the parameters of the formula, and assuming standard deviations/uncertainties a, b, c and d respectively in the measurement, and setting $\ln\left(\frac{I_{pore.dry}}{I_{pore.sat.}}\right)$ = z, then %porosity error value would be calculated as shown below:

Error for a natural log component = $\left(\frac{I_{pore.sat.}}{I_{pore.dry}}\right) \times \sqrt{\left(\frac{b}{I_{pore.sat}}\right)^2 + \left(\frac{a}{I_{pore.dry}}\right)^2}$ = n

Assume percentage porosity value be P, then

Error for percentage porosity = $P \times \sqrt{\left(\frac{c}{\Sigma_l}\right)^2 + \left(\frac{d}{\mathrm{x}}\right)^2 + \left(\frac{n}{z}\right)^2}$ (Eq 3-13)

3.4.2.2 Gravimetric method for porosity determination

All six concrete samples for porosity determination underwent gravimetric evaluation for comparative purposes to the neutron radiography porosity test. The procedure to obtain percentage porosity requires masses of wet and dry sample, the volume of the dry sample and the density of the liquid absorbed by the concrete sample. Porosity of the same sample before and after each submersion-drying sequence is expected to vary because of leaching effect of distilled water. If a dry sample before any wet-dry cycle is denoted by dry-0, then after wet-dry cycle is dry-1. And if a wet sample of the first wet-dry cycle is denoted as wet-1, then initial percentage porosity of a sample is worked out from dry-0 and wet-1. Percentage porosity of the same sample after the first wet-dry cycle derived from dry-1 and wet-2.

The mathematical relation used to determine gravimetric percentage porosity is: [Bee04],

$$percentage\_porosity = \frac{m_{wet} - m_{dry}}{V_{concrete} \cdot \rho_{liquid}} \times 100\% \qquad \text{(Eq 3-14)}$$

where, m_{wet} - mass of the saturated concrete sample

m_{dry} - mass of the dried concrete sample

$V_{concrete}$ - volume of the concrete sample

ρ_{liquid} - density of the liquid filling the pores

Equation 3-14 realizes that to obtain the correct percentage porosity value, the numerator and the denominator have to be the mass of the same material. So this equation assumes the concrete sample to be a transparent and flexible object containing a liquid; with pores being be small balloons floating in the same liquid and contained in the container. It is then appropriate to calculate percentage space occupied by the balloons to the total water contained in the polymer container.

3.4.3 Preliminary analysis of chloride detection

This procedure is similar to the procedure for the determination of the experimental linear attenuation coefficient of water (section 3.4.2.1). In this section neutron and x-rays were used as sources of penetrating radiation. In the case of neutrons, the 3 mm thick liquid-sample holder is used; and in case of x-ray radiation, a 3 mm thick sample holder of similar specifications to those in section 3.4.2.1 but made from polyethylene material, is used.

3.5 Samples Referencing and Conditioning

Concrete samples used in experiments had regular rectangular shapes.

Table 3.5: Sample referencing and conditioning specifications

Sample ID	Concrete type	Conditioning liquid	Submersion-drying cycle-1	Submersion-drying cycle-2
ALL SAMPLES WERE OVEN DRYING AT 50^{O}C AFTER EVERY SUBMERSION, AND THEN RADIOGRAPHED.				
Corrosion test samples DIMENSIONS: [(4.5 ± 0.03) X (4.5 ± 0.04) X (6.0 ± 0.04)] cm^3				
Sample-1	Ferro concrete	20%wt[NaCl]	6 weeks	2 weeks
Sample-2	Ferro concrete	Distilled water	6 weeks	2 weeks
Porosity test samples DIMENSIONS: [(1.5 ± 0.07) X (3.5 ± 0.2) X (7.1 ± 0.3)] cm^3				
Sample-6	Plain concrete	Lime water (3gCaOH/1L distilled water)	288 hrs	104 hrs
Sample-16	Plain concrete	Lime water (3gCaOH/1L distilled water)	288 hrs	104 hrs
Sample-17	Plain concrete	Distilled water	288 hrs	104 hrs
Sample-20	Plain concrete	Distilled water	288 hrs	104 hrs

Drying of laboratory concrete samples

The determination of the concrete sample dry status goes beyond the sample's physical appearance.

The sample was weighed wet, then dried in an oven at 50^0C for 24 hours. After every 24 hours the sample was weighed and its weight percentage change noted. This drying and weighing exercise was repeated until weight percentage change was smaller than 0.005%. This weight was then taken as the dry condition.

3.6 Sample Preparation and Measurement.

For this study two types of concrete samples, plain and Ferro concrete were used. Plain concrete comprises cement, fine aggregates, coarse aggregates and water, while Ferro concrete includes steel reinforcement embedded within the solid matrix. Tables 3.5 and 3.6 summarize the constituting components of the two sample types. Ferro concrete samples were water conditioned for seven days, air dried for one day then oven dried at 50^0C for five days. Plain concrete samples were water cured for 25 days.

Table 3.6: Constituents and proportions of the laboratory plain concrete samples.

Material	**Content (kg/m^3)**
Water	180
Cement I	450
Granite	1000
Sand	707.2

Table 3.7: Constituents and proportions of the laboratory Ferro concrete samples.

Material	**Content (kg)**
Portland cement, type 1	0.37
Silica Fume	0.05
Iron containing coarse Aggregate, 10 mm	0.50
Building lime	1.21
Water	1.14

Chapter 4: Results and discussion

In this chapter results for the corrosion test (effects of chlorides) (section 4.1), preliminary study of the detection of chloride detection in distilled water (section 4.2) and porosity measurements in concrete (section 4.3) are presented.

4.1 Corrosion test (Effects of chlorides) results

In this section reconstructed tomographs of the samples are displayed and discussed where, through the VGStudio's extraction function, the steel bars and their condition could be observed and analyzed.

The time dependence of the volume of steel in two laboratory Ferro concrete samples after 6 week submersion in 20%wtNaCl solution (Sample-1_{after}) and distilled water (Sample-2_{after}) respectively, as determined from tomographic imaging, are shown in Table 4.1. Information about the voxel[g] intensity values and the averaging of volumes is shown in Appendix B. 3-D images (tomograms) demonstrating the corrosive effect of the two liquids on the steel volumes within the laboratory concrete samples before and after submersion to the two liquids, are shown in Figures 4-1 to 4-4. Corroded steel remains trapped within cement paste of the concrete. Samples were dried before imaging.

Table 4.1: Volumes of steel determined within concrete samples that had been exposed to corrosive attack from 20%wtNaCl solution (Sample 1) and distilled water (Sample 2), before and after exposure to liquids.

Sample Identity	Dynamic Range	Average volume of steel imaged within concrete sample [voxels]	Percentage steel volume reduction due to corrosion
Sample-1_{before}	500	80733 ± 198	$54.3 \pm 0.8\%$
Sample-1_{after}	500	36925 ± 542	
Sample-2_{before}	1000	76817 ± 742	$38.7 \pm 1.2\%$
Sample-2_{after}	1000	47089 ± 1369	

g. *A volume element.*

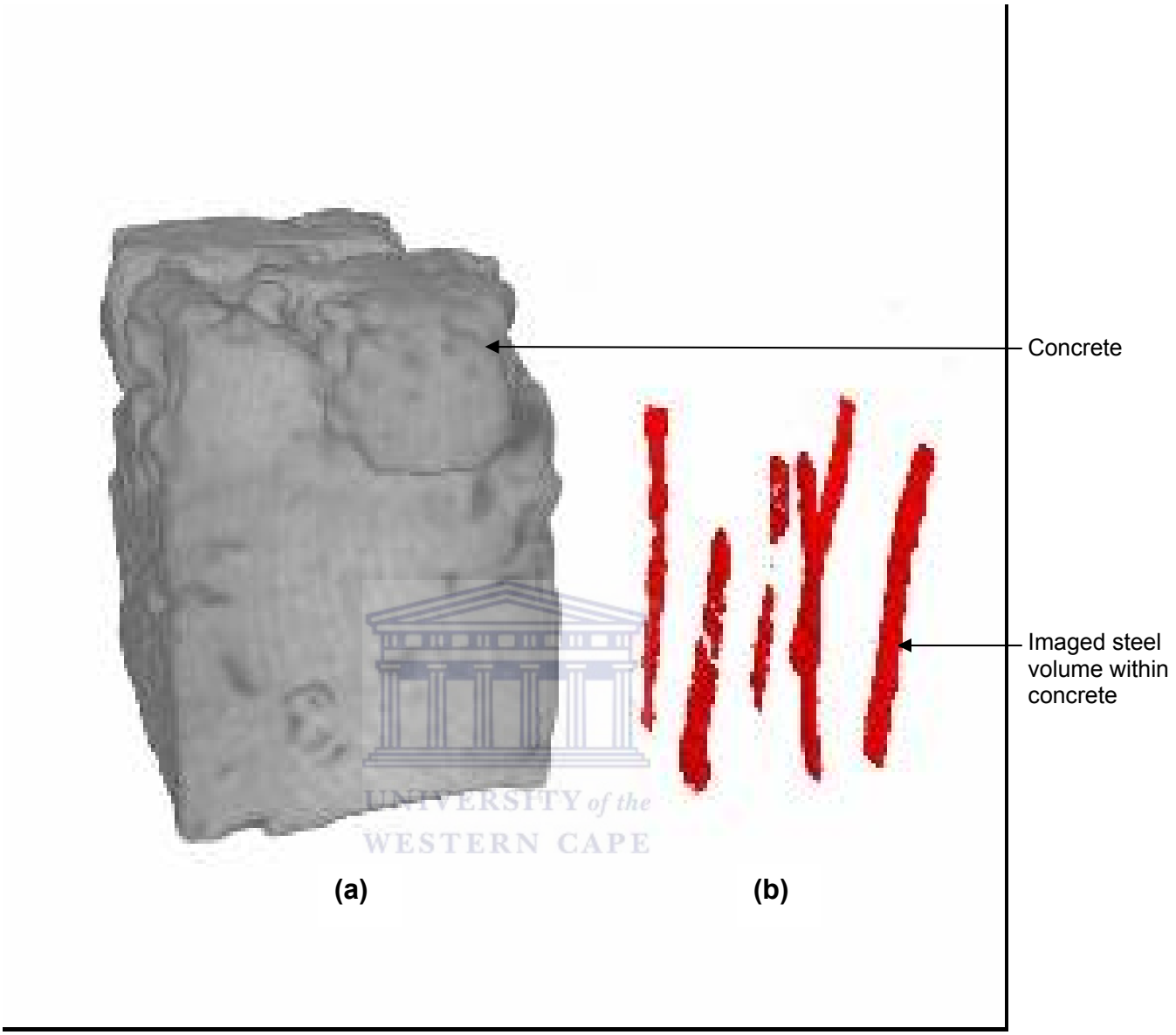

Figure 4-1: Imaging of dried sample-1 before exposure to 20%wt NaCl solution. Representation on the right shows the steel configurations from software extraction from the tomogram.

Figure 4-1 shows the neutron tomogram of sample-1_{before} before submersion into 20%wt NaCl solution. Image (a) shows the outer concrete volume of the sample. Image (b) shows the software extracted steel image originally existing inside the sample by employing classification and extraction functions in VGStudio(Max). The steel volume is determined to be 80733 ± 198 voxels.

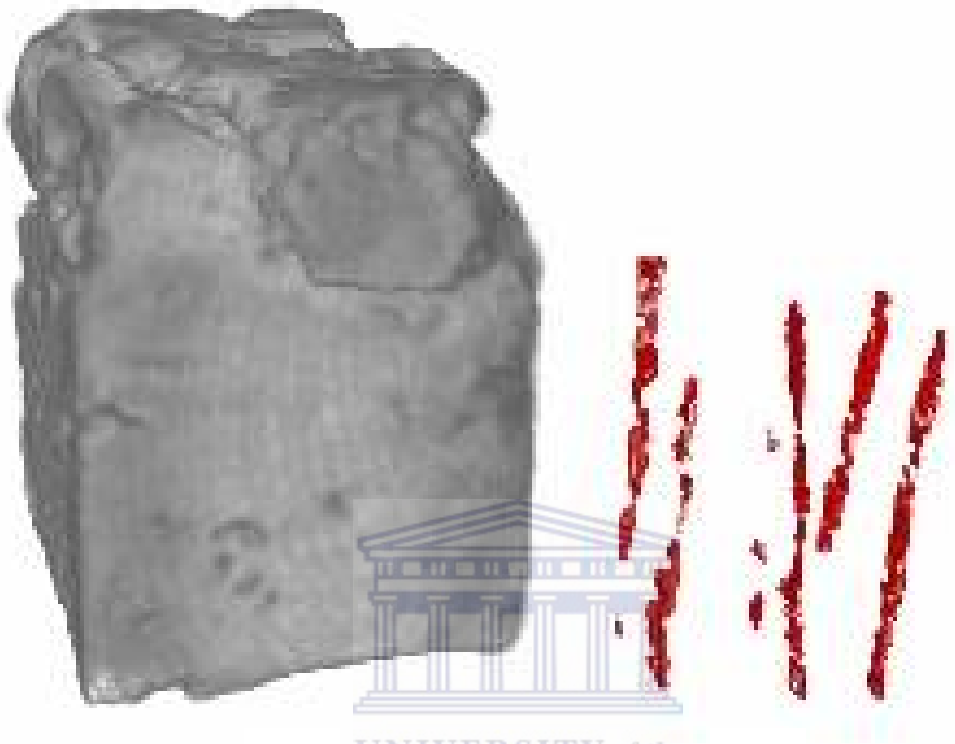

Figure 4-2: Imaging of dried sample-1 after exposure to 20%wt NaCl solution. Representation on the right shows the steel configurations from software extraction from the tomogram.

Figure 4-2 shows the neutron tomogram of sample-1_{after} after submersion into 20%wt NaCl solution and drying. Image (a) shows the outer concrete volume of the sample. Image (b) shows the software extracted steel image originally existing inside the sample by employing classification and extraction functions in VGStudio(Max). The steel volume is determined to be 36925 ± 542 voxels. There is a prominent $54.3 \pm 0.8\%$ of the original steel volume that is lost due to corrosion.

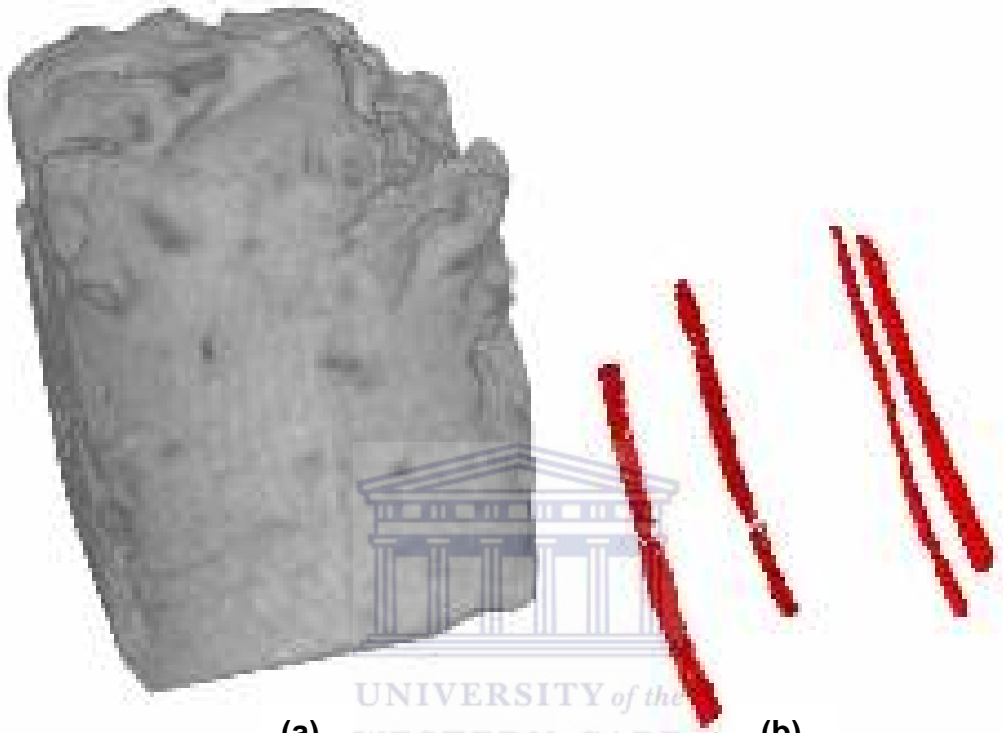

Figure 4-3: Imaging of dried sample-2 before exposure to distilled water. Representation on the right shows the steel configurations from software extraction from the tomogram.

Figure 4-3 shows the neutron tomogram of sample-2_{before} before submersion into distilled water. Image (a) shows the outer concrete volume of the sample. Image (b) shows the software extracted steel image originally existing inside the sample by employing classification and extraction functions in VGStudio(Max). The steel volume is determined to be 76817 ± 742 voxels.

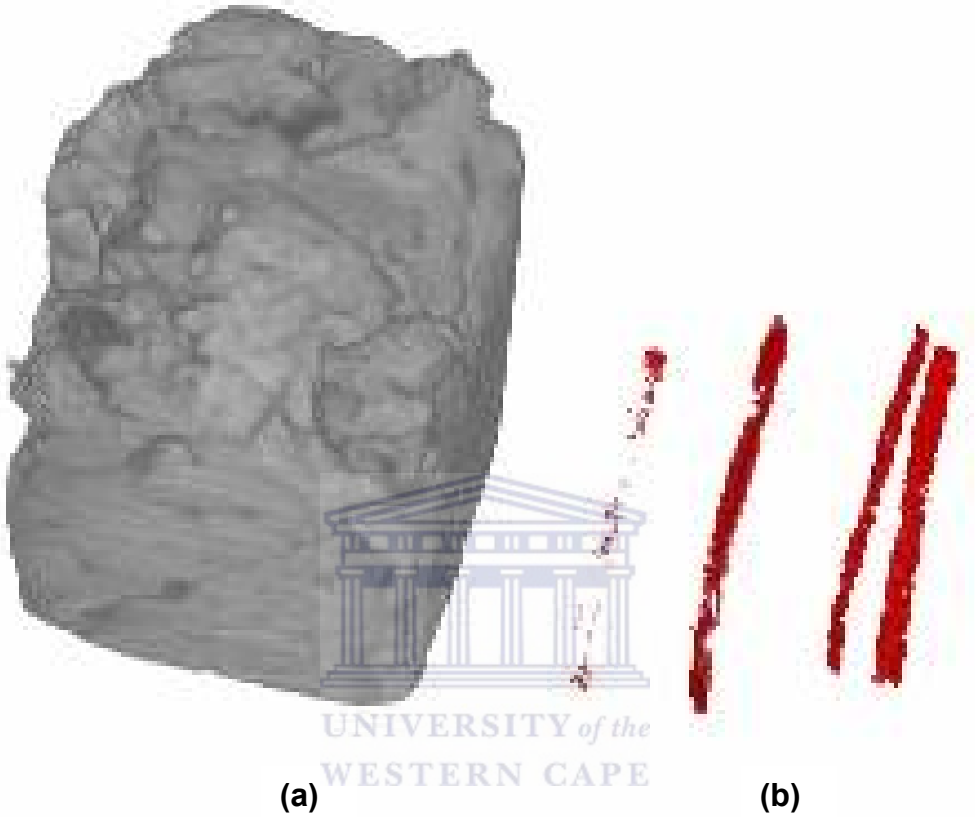

Figure 4-4: Imaging of dried sample-2 after exposure to distilled water. Representation on the right shows the steel configurations from software extraction from the tomogram.

Figure 4-4 shows the neutron tomogram of sample-2_{after} after submersion into distilled water. Image (a) shows the outer concrete volume of the sample. Image (b) shows the software extracted steel image originally existing inside the sample by employing classification and extraction functions in VGStudio(Max). The steel volume is determined to be 47089 ± 1369 voxels. There is a $38.7 \pm 1.2\%$ of the original steel volume that is lost due to corrosion.

4.2 Chloride detection in distilled water

Several solutions of [NaCl] concentrations within distilled water were radiographed using neutrons and x-rays. The attenuation of neutrons and x-rays by different concentrations of NaCl in water are presented in Figures 4-5 and 4-6 respectively. For this procedure, 3 mm liquid pathlength sample holders were used. A polyethylene sample holder was used for the x-ray imaging and an aluminum sample holder for the neutron imaging.

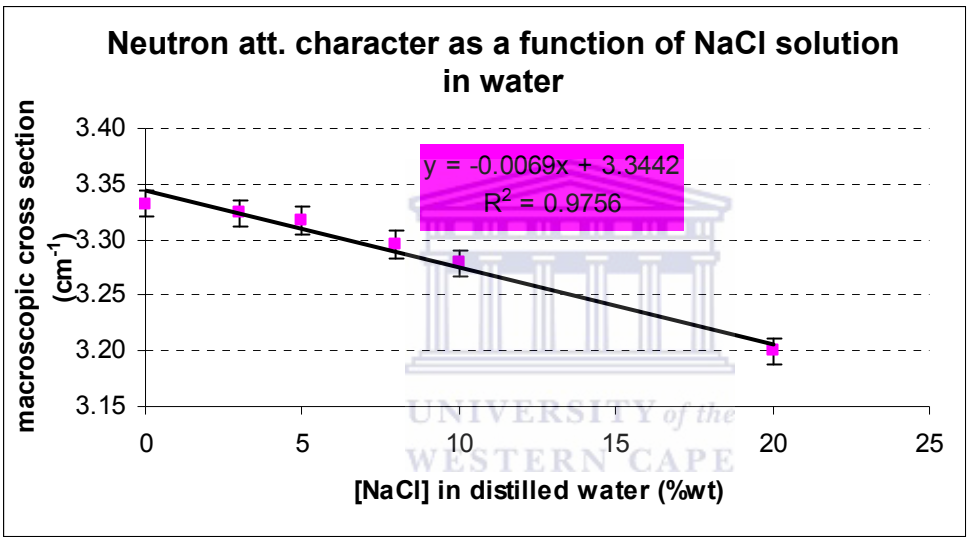

Figure 4-5: Thermal neutron attenuation character as a function of NaCl solutions. Liquid sample used was 3 mm in thickness.

The important feature of Figure 4-5 is the decrease in thermal neutron macroscopic cross section as a function of increased NaCl concentration in distilled water. The negative slope indicates that water has a greater influence on neutron attenuation than the chlorides have. With the curve slope not being very steep and as the chlorine content in concrete samples are normally less than 2% [htt07], the macroscopic cross section values can be taken as a constant value of 3.33 in all subsequent analysis.

This shows that even though distilled water attenuates neutrons more than chlorides, the effect of chlorides on the neutron attenuation is not so remarkable. However, from Appendix A, it can be seen that only at [NaCl] > 5%wt [NaCl] does

chloride have significant effect on neutron attenuation. Overall though change is 4% in neutron macroscopic cross-section between 0%wt and 20%wt [NaCl].

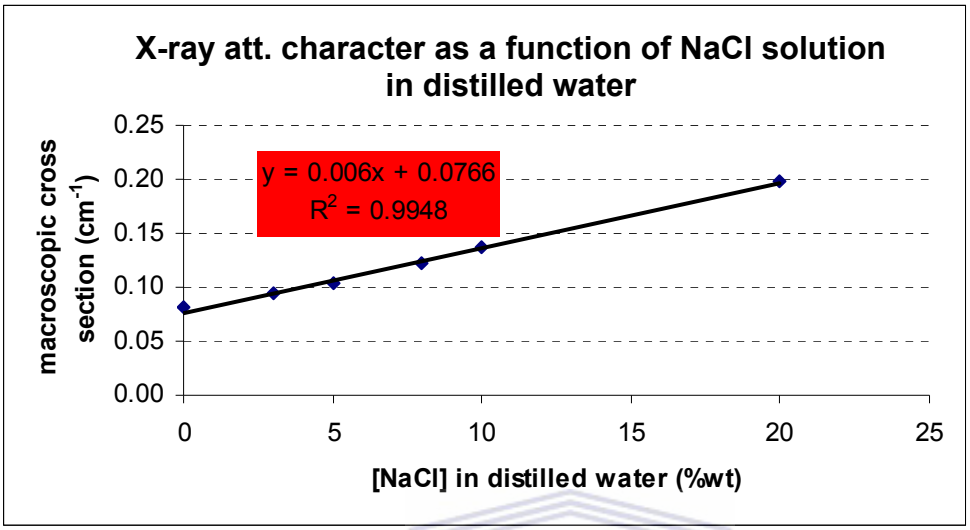

Figure 4-6: X-ray (20 kV) attenuation character of NaCl solution in distilled water. Sample used was 3 mm thickness of liquid contained in a PE container. Error bars are not visible since error = 0.01 (cm^{-1}).

For x-rays the macroscopic cross section as a function of NaCl concentration in distilled water, though having a slight increase as shown in Figure 4-6, can to a first approximation be taken to be constant over concentration range 0 - 10wt% NaCl. Figure 4-6 shows a relatively less steep though positive change in macroscopic cross section of the solutions with the increase in chloride content in distilled water, than that of neutrons. The positive slope implies that x-rays are attenuated better by NaCl than by water. Chlorides within distilled water can be detected by x-rays produced at 20 kV.

The difference between the macroscopic cross section of NaCl solution over concentration range 0 - 20wt% for x-rays is 0.12 cm^{-1}, and for thermal neutrons is 0.143 cm^{-1}. This implies better detection/imaging sensitivities of chloride presence within water by neutrons than by x-rays.

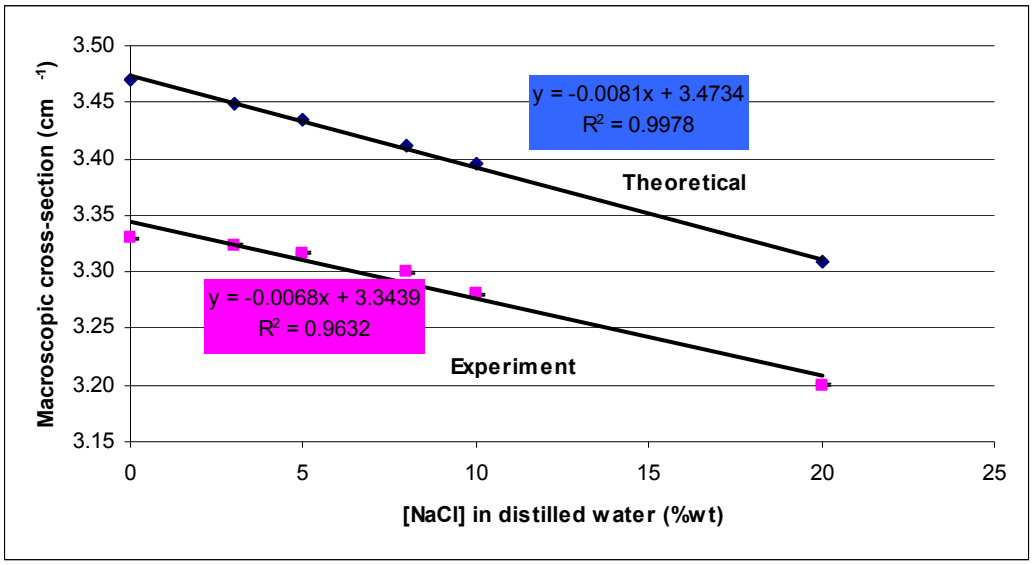

Figure 4-7: Comparison between the theoretical and experimentally obtained macroscopic cross-sections for neutrons through 3 mm thick NaCl solutions of varied concentration.

Figure 4-7 presents a comparison between experimentally and theoretically obtained neutron macroscopic cross section values as a function of NaCl concentration in distilled water. The difference between the two curves is ascribed to scattering effect of neutrons that is a known factor that has to be corrected for in quantification from neutron radiographs when the sample-detection distance is small. The scattering effect as a function of NaCl concentration generally constant and therefore does not pose a problem in comparative studies.

4.3 Percentage Porosity results

The results obtained between plain concrete samples respectively submerged in distilled water (leaching condition) and lime water (3g CaOH/Litre of distilled water), i.e. non-leaching condition as control, are presented in this section. Lime water was considered to be a control because it contains calcium ions that are leached from the concrete by distilled water. Distilled water was used to provide a medium that will demonstrate the leaching effect because it doesn't contain nutrients. Porosity was determined before exposure to the two liquids and 25 days after exposure. For 12 days, samples were submerged in liquids for

24 hours/day and again for the 13 days for 8 hours/day. After realizing that CaOH molecules sink to the bottom of the solution after some few hours, it was decided that samples will only be submerged during operation hours as continuous mixing of the lime water was possible. Percentage porosity results acquired through the gravimetric method and neutron radiography method are shown in Figures 4-8 and 4-9. Figure 4-8 presents results of samples exposed to distilled water and Figure 4-9 results of samples exposed to lime water (3g CaOH/Litre of distilled water). Percentage porosity values obtained are shown in Table 4-2.

Table 4.2: Percentage porosity results as obtained from NRad and Gravimetric methods of porosity determination.

Sample No.	Exposure of concrete	NRad	Gravimetric
6-before	Lime water	4.33 ± 0.04%	10.8 ± 0.1%
6-after	Lime water	4.39 ± 0.04%	11.1 ± 0.1%
16-before	Lime water	4.50 ± 0.04%	11.4 ± 0.1%
16-after	Lime water	4.35 ± 0.04%	11.2 ± 0.1%
17-before	Distilled water	4.70 ± 0.04%	10.5 ± 0.1%
17-after	Distilled water	5.00 ± 0.04%	12.3 ± 0.1%
20-before	Distilled water	3.50 ± 0.03%	10.8 ± 0.1%
20-after	Distilled water	4.00 ± 0.04%	11.5 ± 0.1%

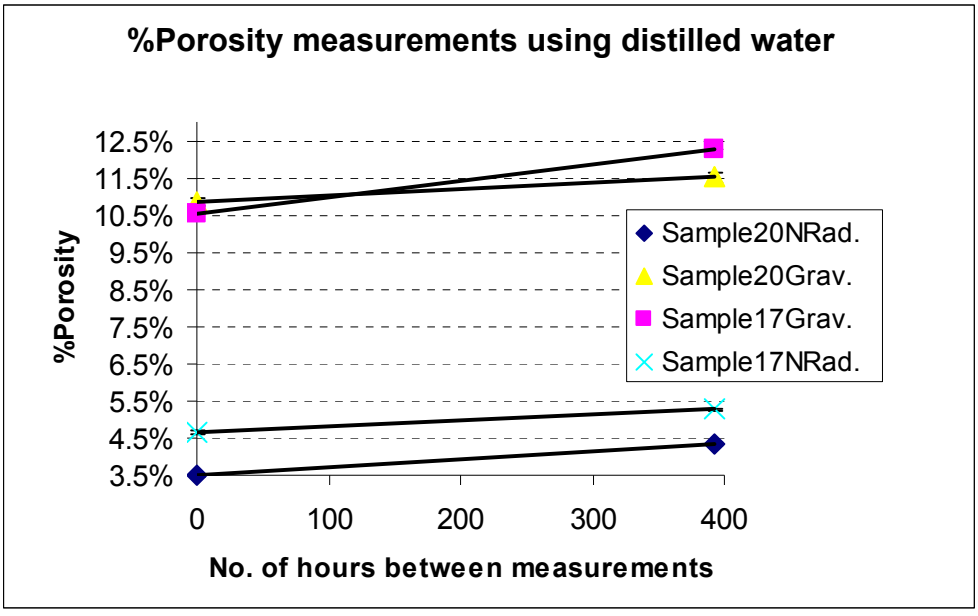

Figure 4-8: Percentage porosity of samples before and after 392 hours submersion in distilled water.

The important feature of Figure 4-8 is the increase in percentage porosity with time for the sample submerged in distilled water. The effect of the scattering of neutrons and detector-sample distance, discussed in section 4.2, are reasons for obtaining unequal NRad and gravimetric values for the same sample.

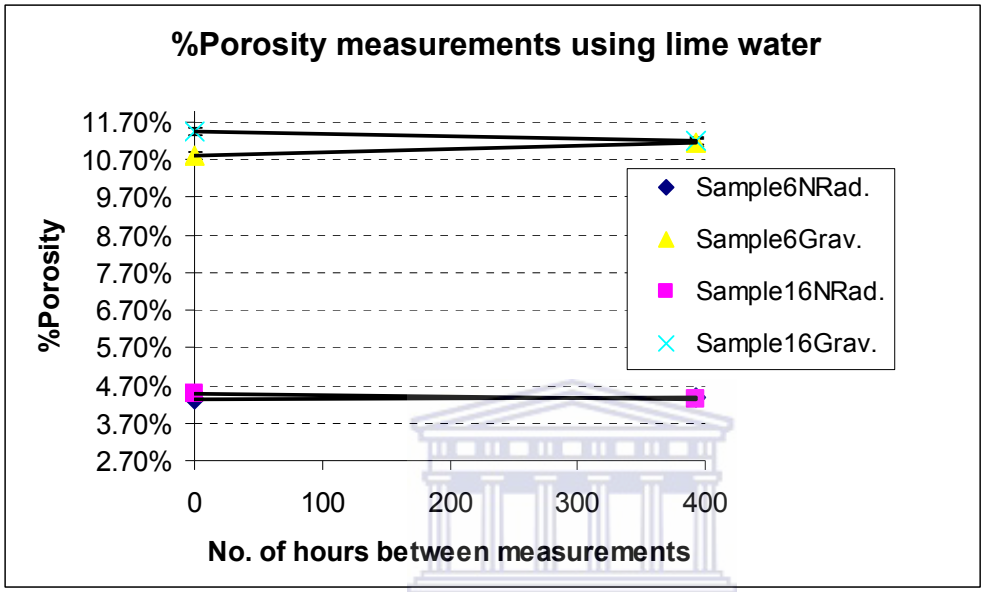

Figure 4-9: Percentage porosity of samples before and after 392 hours submersion in lime water.

The important feature of Figure 4-9 is the corresponding trends between NRad and gravimetrical results of percentage porosity of both samples-6 and-16 after 392 hours submersion in limewater (3g CaOH/Litre of distilled water). The increase in porosity for the samples submerged in distilled water shown in Figures 4.8 demonstrates that some concrete material was lost to distilled water.

Correlation between NRad and gravimetric porosity results

In order to explore the correlation between results obtained from NRad and the gravimetric method, results obtained from the two methods are evaluated on the same set of axes.

The correlation between porosity results obtained from the gravimetric method and through the NRad method is generally good, except for a few points that seem to introduce discrepancies in the data trend. This correlation feature is

explored in Figures 4-10 to 4-13. A discrepancy in results is noticed where initial porosity value for sample-17 obtained gravimetrically is less than that of sample-20, but the initial porosity value of sample-17 obtained through NRad is greater than that of sample-20. Sample 6 point (4.33, 10.8) is further evidence of discrepancy in results due to errors. It may be due to experimental errors imposed by electronic modules or possibly human error. The measurement repeatability will be investigated in future.

Figure 4-10 shows a correlation between the NRad and gravimetrical values obtained from samples submerged in limewater. The correlation was enhanced by the exclusion of the (4.33, 10.8) point from sample 6 and resulted as shown in Figure 4-11.

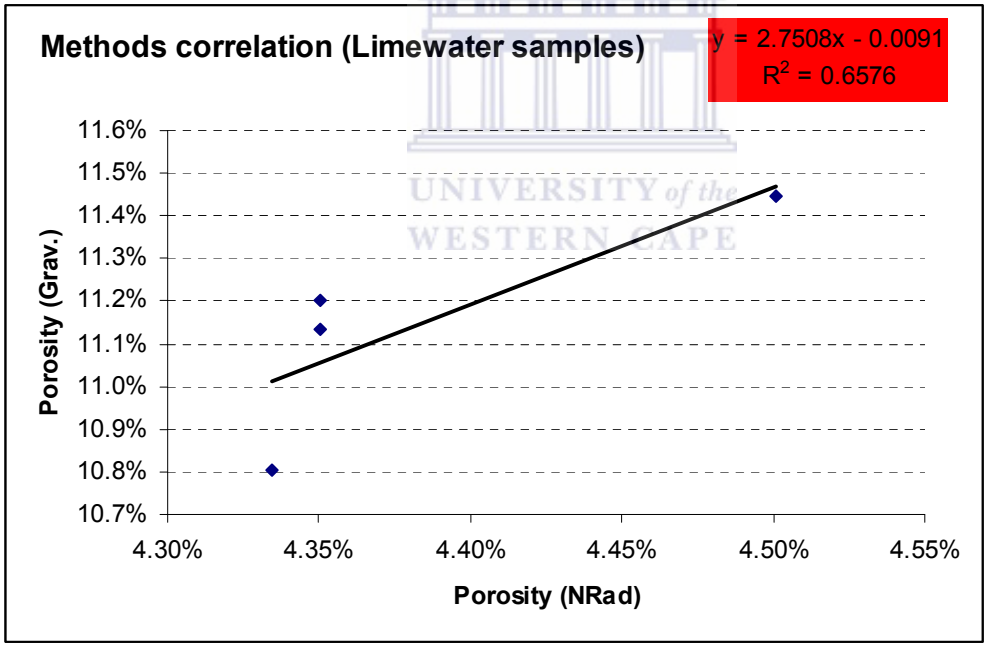

Figure 4-10: Porosity results of samples submerged in lime water, obtained from NRad and Gravimetric methods of porosity determination.

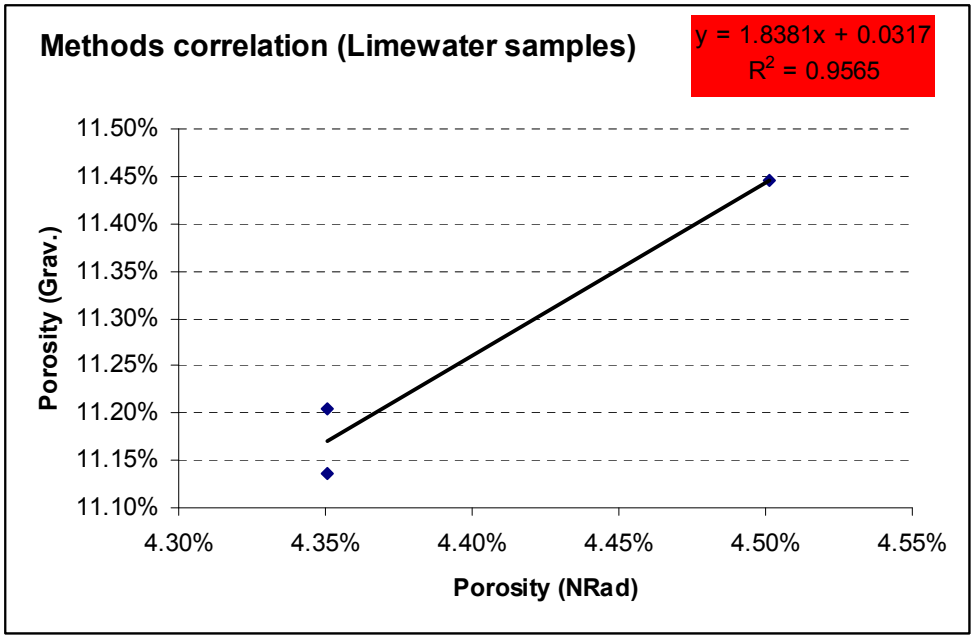

Figure 4-11: Porosity results of samples submerged in lime water, obtained from NRad and Gravimetric methods of porosity determination, after exclusion of one point.

Figure 4-12 presents the correlation plot of distilled water samples' percentage porosity values obtained from NRad and gravimetric methods. A very poor correlation is achieved, until the (4.7, 10.5) point from sample 17 is excluded from the plot, which results as shown in Figure 4-13. Figure 4-13 presents the correlation plot of percent porosity, as derived from distilled water samples, which shows better correlation than that derived from the limewater samples.

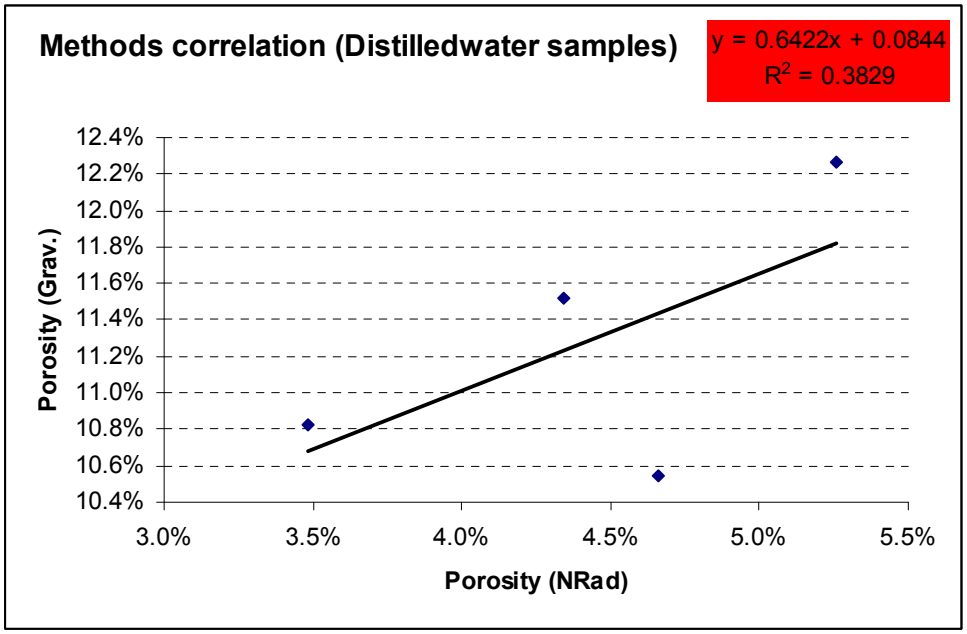

Figure 4-12: Porosity results of samples submerged in distilled water, obtained from NRad and Gravimetric methods of porosity determination.

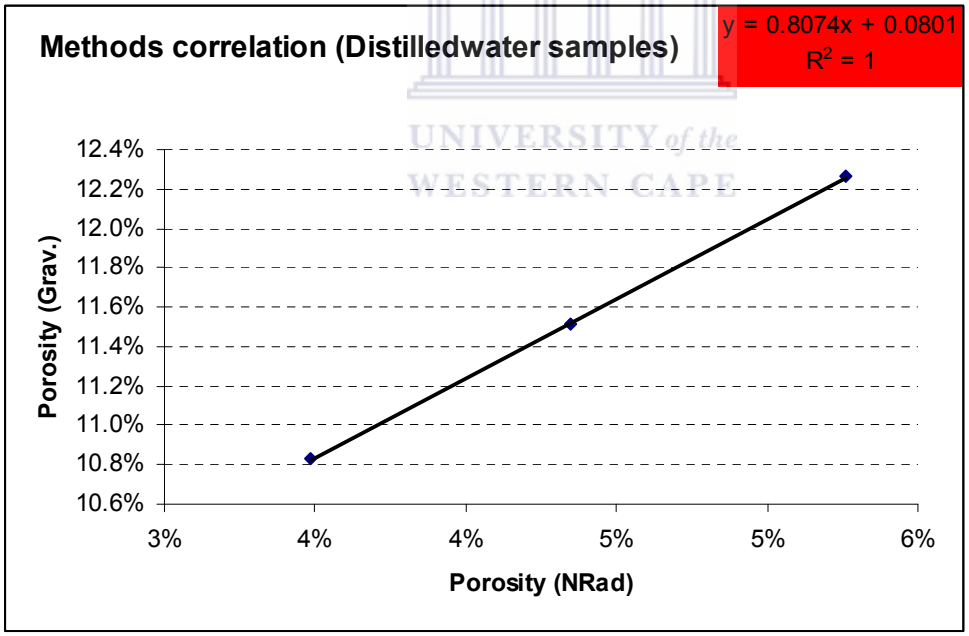

Figure 4-13: Porosity results of samples submerged in distilled water, obtained from NRad and Gravimetric methods of porosity determination. Point (4.7, 10.5) from sample 16 is excluded from the data of plot.

Nrad demonstrated potential as a complementary tool for determination of porosity of porous media.

Chapter 5: Conclusions and Recommendations

This chapter reviews results of the study conducted to explore the capabilities of radiation-based analytical techniques to identify chlorides and their effects within steel reinforced concrete.

XRad, NRad and NTomo were practically explored while Scanning Electron Microscopy (SEM), Small Angle Neutron Scattering (SANS), X-ray Diffraction (XDIFF), Neutron Diffraction (NDIFF), Particle Induced X-ray Emission (PIXE) and Prompt Gamma Neutron Activation Analysis (PGNAA) were only reviewed in the literature. NRad was applied to attain porosity measurements of laboratory plain concrete samples, while imaging of chloride effects within laboratory Ferro concrete samples was studied through NTomo. Preliminary investigation of the attenuation effects of chlorides dissolved in distilled water was conducted through XRad and NRad.

5.1 Experimentally explored radiation-based analytical techniques

5.1.1 Conclusion

5.1.1.1 Sub-study 1 (Corrosion of steel)

NTomo imaging technique was successfully applied to image and quantify corrosive effects due to 20%wt [NaCl] solution and distilled water on the embedded reinforcement thin steel plates in concrete samples.

After six weeks of submersion in a chloride solution (Figure 4-2), steel was substantially reduced whilst the distilled water (Figure 4-4) caused less volume reduction.

Steel elements that exist independent of concrete and submerged in distilled water were observed to have more of its steel volume corroded than steel elements submerged in a chloride solution. It was then suggested that distilled water is may be more corrosive than chloride solution, but the combination of

chlorides and cement paste form a more corrosive substance than distilled water. The soil corrosion mechanism of steel in chlorides contaminated liquid is still not well understood at this point. It makes it very difficult to represent the reaction using a chemical equation.

5.1.1.2 Sub-study 2 (Attenuation of neutrons and x-rays by NaCl)

XRad and NRad were used to study the attenuation effect of sodium chloride solutions of concentrations of 3, 5, 8, 10 and 20 %wt.

Chlorides attenuated neutrons less than water does, this is demonstrated by a negative slope in Figure 4-5.

XRad imaging using 23kV x-rays for the attenuation effect of chlorides dissolved was successful. The slope of a curve of x-rays cross section as a function of NaCl concentration in distilled water, shown in Figure 4-6, has a positive gradient and a little less steep gradient than that of neutron attenuation by NaCl concentration in distilled water. This implies better imaging sensitivities of chloride presence within water by neutrons than by x-rays.

X-rays of 3 keV (10 kV) energy were more desirable for this work (for reasons outlined in section 2.7.1) but no image could be obtained, which was suggested to be due to total absorption of x-rays of this energy by the sample. At this x-ray energy, chlorides have a theoretically larger interaction probability than does water, concrete and sodium; but it is experimentally impractical.

XRad is found less effective than NRad with respect to chloride attenuation effect imaging within distilled water.

5.1.1.3 Sub-study 3 (Porosity measurements)

Linear correlation was, within experimental uncertainties, attained between NRad and gravimetrically obtained porosity results of the comparative porosity study. This linear correlation was evaluated in Figures 4-10 to 4-13. This correlation proved NRad to be the complementary method for percentage porosity measurement. Results obtained from the two methods generally corresponded

but were not numerically equivalent due to the scattering effect of water upon neutrons that causes the anomaly within the neutron radiography results.

5.1.2 Recommendations

- It is recommended that NTomo be explored further to study corrosion rates of steel embedded in concrete on a long term basis, which in turn determines the corrosive character (index) of different corrosive media with which steel reinforced concrete structures are mostly associated with and situated at.
- Since only the preliminary detection of attenuation effects of chlorides dissolved in distilled water was conducted, there is a need for the study of NRad and Tomo with better spatial resolution to investigate chlorides within laboratory concrete samples.
- Further study on porosity determination using cold neutrons is recommended in order to determine if cold neutrons will not eliminate the multiple scattering character of water. This will assist to achieve numerically equivalent porosity values with both NRad and gravimetric methods. The disadvantage of using cold neutrons is that they are less penetrating than thermal neutrons that were used for this study.
- The NRad porosity determination study needs to be conducted over a lengthy period of time for the purpose of repeatability and accuracy (from increase statistical data) of the results.

5.2 Literature reviewed radiation-based analytical techniques

5.2.1 Conclusions

- PGNAA is found capable to provide very important contributions concerning the elemental analysis, concentration determination of elements within thicker concrete structures as well as good concentration sensitivity capability. PGNAA has already been applied to detect chloride ions within concrete [Naq06].

SANS, SEM, PIXE, XDIFF and NDIFF have been found to have the shortcoming not able to investigation samples of dimensions of units of centimeters. SEM, PIXE and XDIFF have been found to have the shortcoming of shallow penetration depth. The above mentioned shortcomings demonstrate that these analytical tools cannot meet the needs of the study, which deals with thick samples (several centimeters).

5.2.2 Recommendations

- For the purposes of this study PGNAA is recommended for practical examination of concrete structure, because of the deep penetration quality of neutrons, good elemental concentration sensitivity as well as its elemental analysis capability.
- Further study to determine the position of propagation front of chloride ions within concrete, as chlorides are absorbed into concrete is desired.
- Radiography and tomography cannot image chlorides dissolved in water and PGNAA can determine chlorides concentration within good concentration sensitivity, but radiography and tomography can image steel within steel reinforced concrete. It is recommended that both these tools be used as complementary instruments to suit the needs of the corrosion study.

Chapter 6: References

[Ale99] Alexander, M. G., Streicher, P. E., Mackechnie, J. R. Rapid chloride conductivity testing of concrete, Research Monograph no. 3 (1999).

[Bay92] Bayon, G., Domanus, J. C., Greim, L., Harms, A. A., Leeflang, H. P., Markgraf, J. F. W., Matfield, R., Taylor, D. J. 1992. Practical Neutron Radiography. Domanus, J. C. (editor). Kluwer Academic Publishers, Dordrecht / Boston / London, p 26-50.

[Bee04] De Beer, F. C., Strydom, W. J., Griesel, E. J. The drying process of concrete: a neutron radiography study. Appl. Rad. and Isot. 61 (2004), p 617- 23.

[Bee05] De Beer, F. C., Le Roux, J. J., Kearsley, E. P. Testing the durability of concrete with neutron radiography. Nucl. Instr. Meth. Phys. Res. A 542 (2005), p 226-231.

[Bee4A] De Beer, F. C., Middleton, M. F., Hilson, J. Neutron radiography of porous rocks and iron ore. Appl. Rad. Isot. 61 (2004), p 487- 495.

[Bee5A] De Beer, F. C. Characteristics of the neutron /X-ray tomography system at the SANRAD facility in South Africa. Nucl. Instr. Meth. Phys. Res. A 542 (2005), p 1-8.

[Burch] Burch, S. F. Measurement of density variations in Compacted Parts using X-ray computerized Tomography. AEA Technology plc, EI, Culham Science Centre, Abingdon, Oxfordshire. (steve.burch@aeat.co.uk), p 1- 2. (paper not yet published).

[Car92] Carl-otto Fischer. 1992. Neutron Radiography (4). Proceedings of the Fourth World Conference in San Francisco, California, USA. John P. Barton (editor). Gordon and Breach Publishers. p 3.

[Cas01] Castellote, M., Alonso, C., Andrade, C., Castro, P., Echeverria, M. Alkaline leaching method for the determination of the chloride content in the aqueous phase of hardened cementitious materials, Cem. Concr. Res. 31 (2001), p 233-238.

[Cas06] Caseres, L., Sagues, A. A., Kranc, S. C., Weyers, R. E. In situ leaching method for determination of chloride in concrete pore water, Cem. Concr. Res. 36 (2006), p 492-503.

[Chap86] Chapman, S. K. 1986. Working with a Scanning Electron Microscope. Lodgemark press LTD, Bank House, Summerhill, Chislehurst, Kent BR7 5RD, England. p 1- 24, 38- 46, 56- 88.

[Cod96] Cody, R. D., Cody, A. M., Spry, P. G., Guo-Liang, G. Concrete Deterioration by Deicing Salts: An Experimental Study. Semisequicentennial Transportation Conference Proceedings. May 1996, Iowa State University, Ames, Iowa.http://www.ctre.iastate.edu/pubs/semisesq/session1/cody/-taken on 15/11/2006.

[Col95] Collico Savio, D. L., Mariscotti, A. J., Guevara, S. R., Mariscotti and Sergio Ribeiro Guevara. Elemental analysis of a concrete sample by capture gamma rays with a radioisotope neutron source. Nucl. Instr. Meth. Phys. Res. B 95 (1995), p 379-388.

[Cul78] Cullity, B. D. 1978. Elements of X-RAY DIFFRACTION (second edition). Addison-Wesley publishing company, inc. p 3- 29, 32- 295.

[Gerde] Gerdes, A., Wittmann, F. H., Lehmann, E. Characterisation of transportation processes in surface near zones of concrete by means of neutron radiography. (paper not yet published).

[Gui89] Guide: 1989. Evaluasie van die betroubaarheid van analitiese data.Hoofstuk 3

[Ham95] Hammouda, B. 1995. A TUTORIAL ON SMALL –ANGLE NEUTRON SCATTERING FROM POLYMERS. National Institute of Standards and Technology, Materials Science and Engineering Laboratory. p 3- 29.

[Har86] Harms, A. A., Wyman, D. R. 1986. Mathematics and Physics of Neutron Radiography. D. Reidel Publishing Company / Dordrecht / Boston / Lancaster / Tokyo. p 1- 6.

[htt01] http://www.tfhrc.gov/structures/pubs-taken on 10/02/2006

[htt02] http://www.infoplease.com/ce6/sci/A0813170.html-taken on 11/04/2006

[htt03] http://columbia.thefreedictionary.com/concreting-taken on 11/04/2006

[htt04] http://www.hps.org/publicinformation/ate/faqs/radiationtypes.html-taken on 18/01/2006

[htt05] http://www.ndt-ed.org/-taken on 6/09/2006

[htt06] http://www.ill.fr/pages/menu_g/docs/universe2003.pdf.-taken on 5/10/2006

[htt07] http://www.nps.gov/goga/history/seaforts/chap9&10/concrete.htm-taken on 11/04/2006

[htt08] http://en.wikipedia.org-taken on 13/03/2006

[htt09] http://www.mrsec.harvard.edu/cams/PIXE.html-taken on 4/10/2006

[htt10] http://www.uksaf.org/tech/pixe.html-taken on 4/10/2006

[htt11] http://www.abo.fi/~jlill/pixe.html-taken on 4/10/2006

[htt12] http://www.aaec.gov.au/nugeo/iba/capabilities/pixe.htm-taken on 4/10/2006

[htt13] http://www.sem.com/analytic/sem.htm-taken on 4/10/2006

[htt14] http://www.danilatos.com/#esem-taken on 4/10/2006

[htt15] http://en.wikipedia.org/wiki/Scanning_electron_microscope-taken on 4/10/2006

[htt16]http://www.isis.rl.ac.uk/largescale/loq/documents/sans.htm-taken on 7/10/2006

[htt17]http://www.necsa.co.za/content.asp?catId=18&Id=146&parentId=18&childId=103&levelId=138&node=4-taken on 7/10/2006

[htt18] http://www.chem.umn.edu/services/lecturedemo/info/ corrosion.html-taken on 3/10/2006

[htt19] Rivers, M. An IDL based tomography reconstruction package. (http://cars9.uchicago.edu/software/tomography. html)-taken 10/08/2006

[htt20] http://ssf.ugent.be/linac/Octopus/-taken on 10/08/2006

[htt21] 3D volume rendering software VGStudio by Volume Graphics, Heidelberg, Germany. (http://www.volumegraphics.com.)-taken 10/08/2006

[htt22] http://www.appscintech.com/.-taken 10/08/2006

[htt23] http://inventors.about.com/library/inventors/bl**xray**.htm-taken on 24/11/2006

[htt24] http://sacoast.uwc.ac.za/publications/1B-Processes.pdf-taken on 2/05/2006 (Salt and the Sea 1B section.)

[htt25] http://www.dme.gov.za/publications/pdf/directories/D4-2002%20salt%20(distil).pdf-taken on 2/05/2006

[htt26] http://www.ornl.gov./info/ornlreview/rev28-1/text/tri.htm-taken on 11/12/2006

[htt27] http://www.isnr.de/history.php-taken on 11/12/2006

[htt28] http://www.cddc.vt.edu/host/atomic/nuketech/smyth01.html-taken on 11/12/2006

[htt29] http://www.physnet.uni-hamburg.de/hp/group_u/about_us.htm-taken on 12/12/2006

[htt30]http://www.science.mcmaster.ca/mnr/NAAPage/naa_prompt_Gamma_Activation.htm-taken on 12/12/2006

[htt31] http://www.isis.rl.ac.uk/largescale/loq/images/loq.gif-taken on 12/12/2006

[htt32] http://midas.npl.co.uk/midas/content/mn027.html-taken on 12/12/2006

[htt33] http://www.gkss.de/.../images_d/werkstoff/holo_exp.gif-taken on 12/12/2006

[htt34] http://www.qub.ac.uk/anat/EMUsite/semroom.htm-taken on 12/12/2006

[htt35] http://www.rpi.edu/dept/materials/COURSES/NANO/shaw/Page5.html-taken on 12/12/2006

[htt36] http://en.wikipedia.org/wiki/Neutron_diffraction-taken on 12/12/2006

[htt37] http://en.wikipedia.org/wiki/X-ray_crystallography-taken on 12/12/2006

[htt38] http://en.wikipedia.org/wiki/Wigner_effect-taken on 07/01/2007

[htt39] http://www.nasa.gov/centers/glenn/about/fs13grc.html--EMSPECTRUM-taken on 07/01/2007

[htt40] http://www.answers.com/topic/neutron-capture-taken on 07/01/2007

[htt41]http://homepage.mac.com/billsart/radiationsemester3/images/image001_000.jpg-taken on 07/01/2007

[htt42] http://www.springerlink.com/content/5r91432665425416/-taken on 02/04/2007

[htt43] www.corrosion-club.com/images/concreteintro4.htm-taken on 08/09/2007

[htt44]http://www.npl.co.uk/materials/residualstress/technique_information.html#Xraydiffraction

[htt45]http://www.npl.co.uk/materials/residualstress/technique_information.html#Neutron

[Jus98] Justines, H. A review of chloride binding in cementitious systems. Nordic concrete Research , Vol. 21 # 1 (1998), p 48-63.

[Kat05] Karthikeyan, T., Saroja, S., Vijayalakshmi, M. Prediction of Chloride Redistribution in Concrete Structure of PFBR. IGC Newsletter Vol. 66 (October 2005). ISSN 0972-5741. (http://www.igcar.emet.in/lis/n/66/igc66/pdf-taken on 12/02/2007).

[Khe99] Khefili, R., Idiri, Z., Omari, L., Seghir, M. Prompt gamma neutron activation analysis of bulk concrete samples with an Am-Be neutron sources. Appl. Rad. Isot. 51 (1999), p 9.

[Lil01] Lilley, J. S. 2001. NUCLEAR PHYSICS-Principles and Applications.John Wiley and Sons, Ltd, Chichester, New York, Weinheim, Brisbane, Singapore, Toronto. p 129- 147.

[Lim01] Lim, C. S., Tickner, J. R., Sowerby, B. D., Abernethy, D.A., McEwan, A. J., Rainey, S., Stevans, R., Manias, C., Retallack, D. An on-belt elemental analyzer for the cement industry. Appl. Rad. Isot. 54 (2001), p 11.

[Lunat] Lunati, I., Vontobel, P., Kinzelbach, W., Lehmann, E.Laboratory visualization of two-phase flow in a natural fracture by neutron tomography. Institute of Hydromechanics and Water Resources Management, ETH Honggerberg, Switzerland, p 1- 2. (paper not yet published).

[Mar97] Martys, N. S., Ferraris, C. F. Capillary Transport in Mortars and Concrete, Cem. Concr. Res. 27, No. 5 (1997), p 760-760.

[Mic02] Michael E. Performance Evaluation of the Westinghouse Science and Technology Center's Prompt Gamma Neutron Activation Analysis Prototype for Verification Assay of Mercury in Mixed Waste McIlwain, Idaho National Engineering and Environmental Lab., Idaho Falls,
ID. Report No: INEEL/EXT-02-00011. p 14, Jan 2002.

[Mid05] Middleton, M. F., Li, K., De Beer, F. C. Society of Petroleum Engineers, SPE Western Regional Meeting, Irvine, CA, U.S.A. 2005. p 1- 6.

[Mil04] Milczarek, J. J., Czachor, A., El-Ghany El Abd, A. Dynamic neutron radiography observations of water migration in porous media. Published by Elsevier B.V. (2004).

[Nac05] Nachiappan, V., Ha Cho, E. Corrosion of High Chromium and Conventional Steels Embedded in Concrete. Journal of Performance of Constructed Facilities, Vol. 19, No. 1 (February 2005), p. 56-61, (doi 10.1061/(ASCE)0887-3828(2005)19:1(56))

[Naq04] Naqvi, A. A., Nagadi, M. M., Kidwai, S., Khateeb-ur-Rehman, Maslehuddin, M. Search of a prompt gamma ray for chlorine analysis in a Portland cement paste. Nucl. Instr. Meth. Phys. Res. A 533/3 (2004b), p 591-597.

[Naq06] Naqvi, A. A., Nagadi, M. M., Al-Almoudi, O. S. B. Prompt gamma analysis of chlorine in concrete for corrosion study. Appl. Rad. and Isot. 64 (2006), p 283- 289.

[Nor00] Nordlund, A., Avdic, S., Dahl, B., Kaiser, N. Transmission measurement of porosity with a neutron generator in geophysics applications. Nucl. Instr. Meth. Phys. Res. A 462 (2001), p 451-456.

[Zhi06] Zhi-Biao, L., Ying-Xiang, W., Ding-Hui, L, 2004a. Studies on absorption coefficients of dual-energy gamma rays and measurements error correction for multiphase fraction determination. Nucl. Sci. and Tech., Vol. 17, No.2 (2006), p 86- 91.

Appendix A: Experimentally obtained neutron macroscopic cross-section of [NaCl] solutions

	3.00 mm								
	Non-normalised values		Normalising ratios	Normalised values		I_0/I_i		Macroscopic cross-section (cm^{-1})	
	average	st. dev.	average	average	st. dev.	average	st. dev.	average	st. dev.
open beam	47150.51	429.3							
empty	46744.03	375.07	1.01	55453.49	1442.13	1.00	0.001	0.00	0.001
0%	46980.25	387.60	1.00	20406.02	559.47	2.72	0.002	3.33	0.001
3%	48394.38	381.44	0.97	20457.37	539.89	2.71	0.002	3.32	0.001
5%	48024.39	387.00	0.98	20499.16	534.91	2.71	0.002	3.32	0.001
8%	47942.74	392.31	0.98	20633.28	539.29	2.69	0.002	3.30	0.001
10%	48151.50	391.14	0.98	20735.60	540.16	2.67	0.002	3.28	0.001
20%	47801.51	390.59	0.99	21232.94	556.63	2.61	0.002	3.20	0.001

Table A.1: Calculation of the macroscopic cross-section, using a 6.94 mm thickness liquid sample holder, for solutions of 0%, 3%, 5%, 8%, 10%, 20% [NaCl] concentrations in distilled water.

	6.94mm								
	Non-normalised values		Normalising ratios	Normalised values		I_0/I_i		Macroscopic cross-section (cm^{-1})	
	average	st. dev.	average	average	st. dev.	average	st. dev.	average	st. dev.
open beam	48598.64	441.73							
empty	48464.50	435.98	1.00	55688.28	1085.91	1.00	0.000	0	0.0004
0%	48943.97	454.39	0.99	8298.34	143.67	6.71	0.002	2.74	0.0003
3%	50053.62	456.72	0.97	8310.53	145.52	6.70	0.002	2.74	0.0003
5%	49568.64	442.53	0.98	8275.29	149.20	6.73	0.002	2.75	0.0003
8%	49717.03	460.02	0.98	8369.02	143.75	6.65	0.002	2.73	0.0003
10%	49749.64	458.33	0.98	8440.08	147.86	6.60	0.002	2.72	0.0003
20%	49905.07	455.53	0.97	8675.26	153.96	6.42	0.002	2.68	0.0003

Table A.2: Calculation of the macroscopic cross-section, using a 6.94 mm thickness liquid sample holder, for solutions of 0%, 3%, 5%, 8%, 10%, 20% [NaCl] concentrations in distilled water.

Appendix B: Neutron tomography data of the steel volume within concrete samples

Sample Identity	Volume of steel within concrete sample [voxels^3]	Mean [Pixel intensity]	Standard deviation [Pixel intensity]
Sample-1_{before}	80535	29183.3	1623.1
Sample-1_{before}	80931	29118.4	3176.6
Sample-1_{after}	37467	25934.8	1534.0
Sample-1_{after}	36383	25411.5	1653.6
Sample-2_{before}	77559	27941.2	1260.0
Sample-2_{before}	76075	28954.5	1330.8
Sample-2_{after}	45720	28507.0	1537.7
Sample-2_{after}	48458	28937.8	1891.4

Table B.1: Steel volume determined from neutron tomograms within laboratory concrete samples.

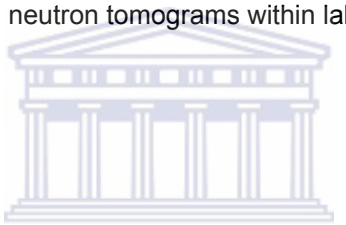

Appendix C: Theoretically calculated neutron macroscopic cross-section of [NaCl] solutions

Microscopic cross-section (cm^2/atom)		Molecule weight (g)		Density (g/cm^3)		Macroscopic cross-section (cm^{-1})	
Na	Cl	H_2O	NaCl	H_2O	NaCl	H_2O	NaCl
4.53E-24	4.98E-23	2.9912E-23	9.70327E-23	1.00	2.17	3.47	1.21

$$\text{Formular: } \text{Macroscopic cross-section}_i = \frac{\text{Density}_{\text{COMPOUND}} \text{ x Microscopic cross-section}_{\text{COMPOUND}}}{\text{Weight}_{\text{COMPOUND}}}$$

NaCl SOLUTIONS BASED ON DISTILLED WATER									
NaCl solutions	Weight per cm^3 of solution (g)		No. of molecules		Percentages based on no. of molecules		Macroscopic cross-section (cm^{-1})		
	H_2O	NaCl	H_2O	NaCl	H_2O	NaCl	H_2O	NaCl	solution
0%wtNaCl	1	0	3.343E+22	0	100.0%	0.0%	3.47	0.00	3.47
3%wtNaCl	0.986	0.030	3.296E+22	3.143E+20	99.1%	0.9%	3.44	0.01	3.45
5%wtNaCl	0.976	0.051	3.264E+22	5.295E+20	98.4%	1.6%	3.41	0.02	3.43
8%wtNaCl	0.961	0.084	3.214E+22	8.616E+20	97.4%	2.6%	3.38	0.03	3.41
10%wtNaCl	0.951	0.106	3.180E+22	1.089E+21	96.7%	3.3%	3.36	0.04	3.40
20%wtNaCl	0.897	0.224	2.997E+22	2.310E+21	92.8%	7.2%	3.22	0.09	3.31

$$\text{Formular: } \text{Macroscopic cross-section}_{\text{SOLUTION}} = \sum\left(\text{Percentage of no. of molecule}_i \text{ per cm}^3 \text{ x Macroscopic cross-section}_i\right)$$

Where:

i- solvent or solute